COVER PAGE ELEMENTS

Report Title: TAOI B- Computational Microstructural Optimization Design Tool for High Temperature Structural Materials

Type of Report: Final Scientific/Technical

Reporting Period Start Date: 9/1/2012

Reporting Period End Date: 2/28/2015

Principal Author(s): Rajiv S. Mishra, Professor, University of North Texas
Indrajit Charit, Associate Professor, University of Idaho

Date Report was Issued: June 17, 2015

DOE Award Number: DE-FE0008648

Name and Address of Submitting Organization: University of North Texas, 1155 Union Circle #305250, Denton, Texas 76203-5017

DISCLAIMER

ABSTRACT

The objectives of this research were two-fold: (a) develop a methodology for microstructural optimization of alloys - genetic algorithm approach for alloy microstructural optimization using theoretical models based on fundamental micro-mechanisms, and (b) develop a new computationally designed Ni-Cr alloy for coal-fired power plant applications. The broader outcome of these objectives is expected to be creation of an integrated approach for 'structural materials by microstructural design'. Three alloy systems were considered for computational optimization and validation, (i) Ni-20Cr (wt.%) base alloy using only solid solution strengthening, (ii) nano-Y_2O_3 containing Ni-20Cr-1.2Y_2O_3 (wt.%) alloy for dispersion strengthening and (iii) a sub-micron Al_2O_3 for composite strengthening, Ni-20Cr-1.2Y_2O_3-5.0Al_2O_3 (wt.%). The specimens were synthesized by mechanical alloying and consolidated using spark plasma sintering. Detailed microstructural characterization was done along with initial mechanical properties to validate the computational prediction. A key target property is to have creep rate of $1x10^{-9}$ s^{-1} at 100 MPa and 800^{o}C. The initial results were quite promising and require additional quantification of strengthening contributions from dislocation-particle attractive interaction and load transfer. The observed creep rate was in order of 10^{-9} s^{-1} for longer time creep test of Ni-20Cr -1.2Y_2O_3-5Al_2O_3, lending support to the overall approach pursued in this project.

TABLE OF CONTENTS

EXECUTIVE SUMMARY

The objectives of this research were two-fold: (a) develop a methodology for microstructural optimization of alloys - genetic algorithm approach for alloy microstructural optimization using theoretical models based on fundamental micro-mechanisms, and (b) develop a new computationally designed Ni-Cr alloy for coal-fired power plant applications. The broader outcome of these objectives is expected to be creation of an integrated approach for 'structural materials by microstructural design'. The overall project was divided in computational and experimental efforts. The goal of computational effort was to predict specific compositions using fundamental strengthening mechanisms. The goal of the experimental effort was to validate the computational approach and document its effectiveness.

Three alloy systems were considered for computational optimization and validation, (i) Ni-20Cr (wt.%) base alloy using only solid solution strengthening, (ii) nano-Y_2O_3 containing Ni-20Cr-1.2Y_2O_3 (wt.%) alloy for dispersion strengthening and (iii) a sub-micron Al_2O_3 for composite strengthening, Ni-20Cr-1.2Y_2O_3-5.0Al_2O_3 (wt.%). The hierarchical nature of the microstructural optimization is based on the additivity of various strengthening mechanisms. While the theoretical foundation of adding nanoparticles is based on the dispersion strengthening to impede the dislocation motion, the choice of relatively coarser particles was to enhance load transfer. For high temperature deformation, it is important to consider the change in the nature of dislocation-particle interaction. In the present work, this was incorporated by considering an attractive dislocation-particle interaction model for high temperature strength. One handicap during the present effort was the lack of independent size selection of second phase particles. For example, the size of nano-Y_2O_3 particles for experimental work was dictated by availability of powder from commercial source. So, the genetic algorithm optimization output could not be critically evaluated as it was not possible to synthesize the exact predicted microstructure.

The specimens were synthesized by mechanical alloying and consolidated using spark plasma sintering (SPS) in the temperature range of 700–1100 ^oC and pressure of 40-80 MPa. Near full density was obtained for all the three compositions. Detailed microstructural characterization was done at all stages. The mechanically alloyed powders were examined by x-ray diffraction (XRD) and scanning electron microscopy (SEM). The consolidated specimens were examined by transmission electron microscopy (TEM) in addition to XRD and SEM. The key features that were important to track were, size of second phase particles, stability of second phase particles and grain size. One of the unintended consequence on the microstructure was impact of the second phase particles on the final grain size. The grain size could not be varied independently.

The mechanical properties were evaluated to validate the computational prediction. The initial approach was to examine the hardness of all SPS specimens. This provided a quick way of down selecting process parameters. The tensile properties were obtained by a few mini-tensile tests, but the specimens did not exhibit much tensile ductility. Therefore, most of the subsequent temperature dependent work was done using compression tests and compression creep tests. The Ni-20Cr-1.2Y_2O_3-5Al_2O_3 composite had room temperature strength of 1470 MPa and a strength of 250 MPa at 800^oC. A key target property was to have creep rate of $1x10^{-9}$ s^{-1} at 100 MPa and 800^oC. The initial results were quite promising and require additional quantification of strengthening contributions from dislocation-particle attractive interaction and load transfer. The specimens showed extensive primary creep. In order to minimize the effect of primary creep, one specimen

was tested for >2500 hours. The observed creep rate was of the order of 10^{-9} s^{-1} for this longer time creep test of Ni-20Cr-1.2Y_2O_3-5Al_2O_3, lending support to the overall approach pursued in this project.

INTRODUCTION

The conventional approach for development of new materials requires a wide range of experiments and relies on discovery. The 'discovery' approach is very expensive and time consuming. Typically it takes 15-20 years to develop and implement new alloys. Therefore, the new push is on the development of materials by 'design'. This new approach requires the use of physics-based models and empirical rules together with an optimization scheme to synthesize the microstructure that will satisfy the desired macroscopic mechanical properties. Increasing the operating temperatures in coal-fired power plants, gas turbine inlets, and other high temperature structural components in order to improve their efficiency and economy will require new materials with high mechanical and creep strength, oxidation and corrosion resistance. Nickel-based alloys are promising candidates for such applications due to their excellent corrosion resistance at elevated temperatures [1-3].

While conventional nickel-based alloys may not be very stable at high temperatures due to coarsening or dissolution of the second phase particles, nickel-based ODS alloys, reinforced by homogeneously dispersed nanoparticles (usually Y_2O_3), are quite stable during high temperature applications in excess of 1000 °C [4]. Homogeneous dispersion of nanometer and stable oxide particles in the matrix of nickel-based ODS alloys can act as effective barriers against the dislocation motion [2, 5-7] and improve the high temperature mechanical properties and creep strength [8]. The pinning effects of oxide nanoparticles depend on the mean particle separation, (the mean distance between the particles) which is a direct result of the particles' number density [1]. According to theoretical calculations and experiments, a combination of a mean particle separation of 100-250 nm for 10-20 nm yttria particles and grain aspect ratio of a minimum of 10 could be promising for high- temperature applications [3, 6].

In nickel-based ODS powder containing both Al and Y_2O_3, different Y-Al-O particles such as $Y_3Al_5O_{12}$, $YAlO_3$ (perovskite), $Y_4Al_2O_9$ and $YAlO_3$ (hexagonal) can form during consolidation [1]. Recently, it has been noted that adding some minor elements such as Ti and Hf can replace the Y-Al-O particles with Y-Ti-Hf-O particles. The effects of adding minor elements such as Ti, Mg, Zr, Ca and Hf to Ni-0.5Al-1Y_2O_3 (wt.%) was studied by Tang *et al.* [1], and Hf was found to be the most effective oxide at refining the formed oxide particles, especially at a concentration of 0.8 wt.%. Formation of $Y_2Hf_2O_7$ was found to be responsible for oxide particle refinement and consequent improvement in mechanical properties through operation of the Orowan mechanism [9].

Another strengthening mechanism to consider for developing nickel-based ODS alloys would be composite strengthening mechanism or load transfer mechanism [10]. For example, studies have also shown that submicron Al_2O_3 of (0.5-1 μm diameter) could be efficient for composite strengthening due to lower density and higher modulus of elasticity [11, 12]. Hornbogen *et al.* [13] and Rosler *et al.* [14] predicted that a combination of nanoparticles and coarser particles dispersed in the microstructure would offer both dispersion strengthening and composite strengthening. In this approach, dislocations would effectively shear the nanoparticles that are smaller than a "critical size" and bypass the coarser particles that are larger than the "critical size". Through dispersion strengthening and composite strengthening as dominant mechanisms at high temperatures, enhanced mechanical properties would be achieved.

Nickel-based ODS alloys are conventionally produced by mechanical alloying (MA) or ball milling of elemental or pre-alloyed powders in combination with nano-sized Y_2O_3 (yttria) powder followed by canning, degassing and consolidation either via hot extrusion (for rods and wires) or hot isostatic pressing (HIP) and rolling (for sheets) [3].

One of the critical steps in producing nickel-based ODS alloys is the milling process in which powder blend of yttria and pure nickel or pre-alloyed nickel (for example, Ni-20Cr) are milled, and a fine homogeneous distribution of yttria particles in the metal matrix can be attained. If powder blends of yttria and two or more metal powders are milled in addition to homogeneous yttria dispersion, formation of solid solution may be also achieved [3]. During milling, the metal powder particles become trapped between the colliding balls (milling media) and cold welded together while the oxide particles become finer until trapped between layers of metal powders sandwich forming a composite. After cold welding and particle agglomeration, a fracture stage occurs and large composite powders break down until a steady state situation is reached between cold welding and fracturing. Consequently, a uniform distribution of oxide nanoparticles within metallic components would be achieved [15, 16].

In conventional consolidation methods such as extrusion or HIP, a final annealing at high temperature is usually required to develop a stable coarse grain structure alloy [16]. The numbers of thermal processing steps could be eliminated if a pulsed direct current (DC) is simultaneously used with a uniaxial pressure to primarily sinter the powders [17, 18]. This could reduce the time, cost and possibly deformation texture in the consolidated materials [19]. Field activated assisted sintering technique (FAST), also known as SPS or pulsed electric current sintering (PECS), applies a pulsed DC to enhance sintering rate of the powders to near full density at relatively lower temperatures. Pulsed DC flows through the die and powder compact producing heat via Joule heating mechanism, providing a much higher heating rate and shorter sintering time. Thus, grain growth during sintering can be essentially minimized, leading to improvement in mechanical properties [18, 20-22].

There are limited reported applications of SPS in the processing of nickel-based ODS alloys containing Y_2O_3 as dispersoids [1, 2, 4, 23, 24]. Park *et al.* [2] developed Ni-22Cr-11Fe-1TiO_2, Ni-22Cr-11Fe-1Y_2O_3 and Ni-22Cr-11Fe-0.5TiO_2-0.5Y_2O_3 (wt.%) by milling for 40 h in a planetary ball mill and SPSed the ball milled powder at 1100 °C for 5 minutes under a pressure of 40 MPa. They suggested that nano-sized TiO_2 and Y_2O_3 particles went dissolved during MA, and then precipitated out during SPS, forming Y-Ti-O particles. However, Ni-22Cr-11Fe-1Y_2O_3 exhibited the best mechanical properties among all of the developed alloys.

The present work focused on development of a new Ni based ODS alloy for high temperature application through material by design. Kulkarni *et al* [25] considered genetic algorithm (GA) based optimization approach to develop microstructure of an alloy. The chosen Ni ODS alloy system has:

(a) Cr for solid solution strengthening,
(b) nano Y_2O_3 or Cr_2O_3 particles for dispersion strengthening and grain size stabilization, and
(c) submicron Al_2O_3 for composite strengthening through increase in modulus and density reduction.

The GA optimization scheme was used to determine the volume fraction of each type of particles and the desired grain size.

Ni-20Cr-1.2Y_2O_3 (wt.%) alloy was processed by ball milling and SPS, and the effects of milling times and sintering parameters on the properties of sintered nickel-based ODS alloy were investigated. There have been very limited studies on the effects of milling parameters and microstructural evolution during milling of nickel-based ODS powder [26]. In their study, elemental powder of Ni and Cr powders were milled for 30 h to obtain a nanostructured Ni-20Cr alloy. Such solid solution reaction occurred due to interface diffusion and diffusion through dislocations and subgrain boundaries driven by chemical heterogeneity within a lamellar spacing of 500 nm.

Tasks performed

The overall work had computational and experimental aspects. All the computational work were done at the University of North Texas. The University of Idaho participated in targeted experimental activities to support and validate the computational activities. Some experimental work was also planned for UNT and the tasks below are identified with the institution.

Task 1.0- Compilation of Relevant Strengthening Mechanisms and Literature (UNT)
Task 2.0- Genetic Algorithm Optimization of Composition (UNT)
UNT already had a GA model in MATLAB for aluminum alloy. This was modified and applied to the Ni-Cr alloy work. The constants for various equations were taken from task 1.
Task 3.0- Refinement of Threshold Stress Model (UNT)
The attractive dislocation-particle of Mishra et al. and the synergistic microstructural approach of Rosler et al. was integrated to include bimodal microstructural distribution.
Task 4.0- Mechanical Alloying of Metallic Powders (UI)
Following the alloy design recommendations by the UNT, UI procured required metal powders and performed high energy ball milling to produce Ni-Cr based alloys. The SPEX 8000M Mixer/Mill was used for this purpose.
Task 5.0- Spark Plasma Sintering of Mechanically Alloyed Powders (UI)
Spark plasma sintering (SPS) was carried out at a varied temperature (700–1000 ^oC) and pressure (40-80 MPa) range. Given the right combinations of processing parameters, SPS can produce microstructure with full density. The goal was to achieve microstructure with the characteristics that could be used for model validation.
Task 6.0- Density Measurement (UI)
The physical density of all the samples was measured using Archimedes principle. This also gave us a preliminary understanding of the process capabilities and the amount of residual porosity if any.
Task 7.0- Microstructural Characterization (UI)
The University of Idaho carried out microstructural characterization using HRTEM. Microstructural parameters like grain size, particle size, volume fraction etc. was evaluated.
Task 8.0- Thermal Analysis (UI)
Detailed thermal analysis (primarily differential scanning calorimetry) measurements of the powder and spark plasma sintered samples was carried out to ascertain the thermal stability of the particles as a function of temperature (up to 1500^oC) using the STA equipment. Differential

heating rates was used to assess the kinetics of any detectable phase changes.
Task 9.0- Small Volume Mechanical Testing (UI)
Microhardness test was carried out on the samples. Shear punch test fixture set up on the Instron machine was performed. The results were benchmarked against the mini-tensile test results.
Task 10.0- Mini-tensile Testing (UNT)
UNT has a niche mini-tensile testing setup that requires only a 10 mm total specimen length. The SPS specimens and SPS and hot compressed specimens were tested using this technique.
Task 11.0- Creep Testing (UNT)
Compression creep tests was done to validate the theoretical predictions.
Task 12.0- 3D Atom Probe (UNT)
Limited 3D atom probe work was done to quantify the distribution of nano particles. This was used for refinement of theoretical calculations.

THEORETICAL BACKGROUND

Strengthening mechanisms

Compilation of relevant theoretical and phenomenological models was done for low temperature strength, ductility and high temperature strength.

Low temperature strengthening

a) Grain size strengthening

At lower temperatures grain boundaries are effective obstacle to dislocation motion. The yield strength can be expressed in terms of grain diameter as

$$\sigma_y = \sigma_0 + Kd^{-0.5} \quad (1)$$

where σ_y is yield strength, σ_o yield strength of a single grain, K a constant and d the grain size. Equation (1) is known as the Hall-Petch [27, 28] equation.

b) Solid solution strengthening

The solid solution strengthening due to multicomponent Ni-alloys has been investigated by Gypen and Deruyttere [29] and the strengthening can be expressed as

$$\Delta\sigma_s = \left(\sum k_i^{\frac{1}{n}} c_i\right)^n \quad (2)$$

where (2) is the solid solution contribution. k_i is the strengthening constant for solute i, c_i is the concentration of solute i and the value of n is taken as ½. For Ni-Cr alloy the value of k is 337 MPa at fraction$^{-1/2}$ [30].

c) Dispersion strengthening

For non shearable particles or dispersoids, a modified Orowan equation [31] was employed to estimate the strengthening. It can be expressed as

$$\Delta\sigma_p = \frac{Gb\sqrt{f_d}}{d_p} \quad (3)$$

where G is the shear modulus, b is the burger vector, f_d is the volume fraction of dispersoids and d_p is the particle diameter.

d) Composite strengthening

Composite strengthening differs from the dispersion strengthening in the particle size, and the interparticle spacing of particles, which are much larger. In particle reinforced composite the reinforcement phase is significant stronger than the matrix and during loading a significant fraction of load is transferred to the reinforced phase. Rule of mixture holds good for the uniformly distributed mixture. It is expressed as

$$\sigma_c = V_p\sigma_p + V_m\sigma_m \tag{4}$$

where σ_c is the estimated strength of the composite, V_p and V_m are the volume fraction of the particle and matrix respectively, σ_p and σ_m are the yield strength of the particle and matrix. Rule of mixture gives the upper bound values of the properties.

The strengthening coefficient, $\wedge$ due to load transfer is defined as

$$\wedge \approx 1 + 2\left(2 + \frac{l}{R}\right) f_r^{\frac{3}{2}} \tag{5}$$

for fibers of length 2l and diameter 2R and reinforcement volume fraction f_r [14].

Ductility

The main reason for the fracture of material under plastic deformation is formation and growth of microvoids. Presence of inclusions and second phase particles lead the fracture of material as they act as sites for the nucleation of microvoids. The strain at which the specimen fails is referred as a measure of ductility of the material.

Majumdar and Pandey [32] developed the expression for the failure strain for the alloy. It can expressed as,

$$\varepsilon_c^f = \left({}^{1}/_{\Omega\sqrt{2}}\right)\left(1 - \left({}^{6f}/_{\pi}\right)^{\frac{1}{3}}\right)(1.285 - 4.403\, f \quad + 4.122\, f^2) \tag{6}$$

where f is the volume fraction of the particles. The value of Ω can calculated as

$$\Omega = \frac{9.3 + 35\varepsilon_B}{0.3 + 100\varepsilon_B} \tag{7}$$

$$\varepsilon_B = \left(\frac{\varepsilon_m^f}{2.2 + 7N(N+1)}\right)\left(\frac{\varepsilon_m^f}{0.002}\right)^N \tag{8}$$

by putting ε_m^f equal to the work-hardening coefficient.

High temperature strength

At elevated temperature most of the strengthening mechanism which involved for lower temperature has no longer significant effect. The grain boundaries no longer act as obstacles for dislocation motion. Dispersion strengthening is the most effective way to increase high temperature strength. Before 1980s, all attempts to model threshold stress for dislocation-particle interaction were based on the assumption that dislocation is repelled by hard particles. TEM results

showed that interaction between particle and dislocation is attractive and dislocations to be pinned at departure side.

a) Dislocation creep of dispersion strengthened alloys

Considering 'departure side pinning' concept, Arzt and Roser [6] developed a thermally activated detachment model for dislocation creep. According to this mechanism steady state creep rate can be expressed as

$$\dot{\varepsilon} = \frac{6\lambda\rho D}{b} \exp\left(-\frac{Gb^2 r[(1-k)(1-\sigma/\sigma_d)]^{\frac{3}{2}}}{k_B T}\right) \tag{9}$$

where $\dot{\varepsilon}$ is the creep rate, λ is the interparticle spacing, ρ is the dislocation density, r is the particle radius, k is the relaxation parameter, σ is the applied stress and σ_d is the athermal detachment stress. The main disadvantages of this model are that the value of k and σ_d have to be determined from the experimental data and hence these terms cannot be calculated from the first principles.

Mishra *et al.* [33] proposed an empirical relationship based on the concept of dislocation particle interaction and suggests that the dislocation particle interaction leads to both the threshold stress and change in deformation kinetics. The expression is given by

$$\dot{\varepsilon} = 8.3 * 10^8 \frac{DGb}{k_B T}\left[exp\left(-104\sqrt{\frac{b}{\lambda}}\right)\right]\left(\frac{\sigma-\sigma_0}{E}\right)^5 \tag{10}$$

where E is the Young's modulus and σ_0 is the threshold stress.

b) Threshold stress model

Initial efforts to model threshold stress were based on the concept of 'repulsive 'dislocation –particle interaction. This concept was based on the assumption that the dislocations are repelled by the elastically hard particles and the applied stress has to overcome this repulsive force. The fact that dislocations entered the matrix–particle interface at elevated temperatures and were pinned on the departure side clearly contradicts the model based on the 'repulsive' concept.

Following models have been developed with the concept of departure side pinning:

1. Diffusional relaxation model (Srolovitz et al 1983 [34])
2. Energy reduction model (Nardone et al 1984 and Arzt and Wilkinson et al 1986 [35,36])
3. Dislocation and positive climb model (Mishra et al 1994,1995 [33,37])

A comparison of theoretical predictions of threshold stress models with experimental trends are shown in Table 1.

Table 1. Comparisons of theoretical predictions of threshold stress models with experimental.

S. No	Experimental characteristics	Diffusional relaxation model (Srolovitz et al 1983) [34]	Energy reduction model (Nardone et al 1984, Arzt and Wilkinson 1986) [35,36]	Dissociation and positive climb model (Mishra et al) [33,37]
1	Magnitude lower than Orowan stress	No	Yes	Yes
2	Temperature dependent	No	No	Yes (qualitative at this stage)
3	Interparticle spacing dependent	Yes	Yes	Yes
4	Particle size dependent	Weak dependence	No	Yes
5	Grain size dependent	No	No	No
6	Local climb Configuration	Yes	Yes	For energy reduction of > 36%
7	TEM contrast at matrix-particle interface	No	Yes	Yes
8	Departure side pinning	Yes	Yes	Yes

Mishra *et al.* [33] proposed that dislocation energy is reduced by dissociation of lattice dislocations in the matrix –particle interface and their transformation to interfacial dislocations. The threshold stress is given by

$$\sigma_0 = 0.002\, G \left(\frac{b}{r}\right) exp\left(20\frac{r}{\lambda}\right) \tag{11}$$

Grain size and interparticle spacing can be expressed in terms of particle size, volume fraction as [38],

$$d = \frac{4}{3}\frac{r}{f} \tag{12}$$

$$\lambda = 1.23\, r \sqrt{\frac{2\pi}{3f}} \tag{13}$$

Refinement of threshold stress model

It is possible to obtain a synergistic effect through interaction of small dispersoids and large reinforcement as discussed earlier. Composite strengthening differs from the dispersion strengthening in the particle size and the interparticle spacing of particles is too large to exert a significant back stress on dislocation motion. In particle reinforced composite the reinforcement phase is significantly stronger than the matrix and during loading a significant fraction of load is

transferred, which increases the load carrying capability of the composite. The strengthening coefficient, ∧, due to load transfer is defined earlier as equation (5) [14].

The strengthening coefficient, ∧, is dependent on reinforcement volume fraction, aspect ratio and stress exponent. As stress exponent n ~ 5 for creep strength, there is noted effect in high temperature strength even with little load transfer coefficient. Deshmukh *et al.* [39] performed creep experiments on Al-Y_2O_3 -10SiC composite at three different temperatures. They compared the physically measured values of threshold stress using measured detachment angle from creep experiments with one calculated from in-situ TEM experiments as shown in Fig. 1. The difference between mean detachment stress and experimental threshold stress values can be attributed to the contribution of load transfer.

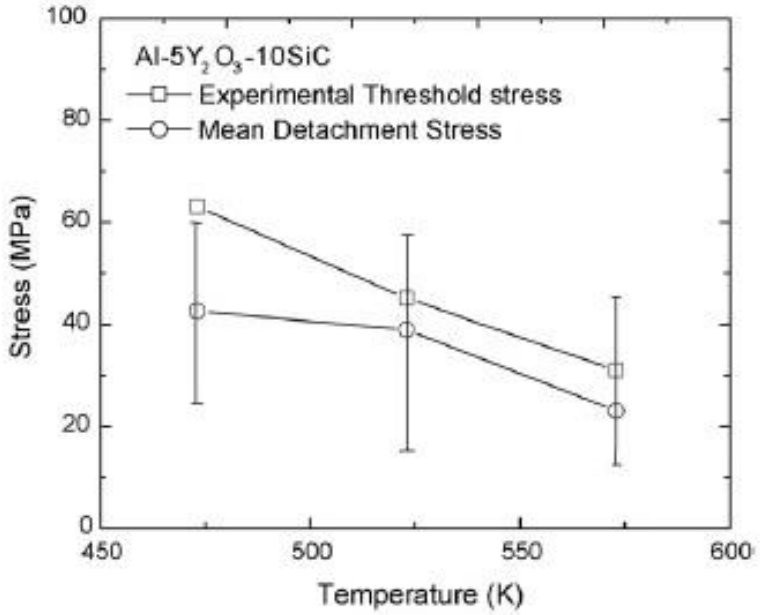

Figure 1. Comparison of experimental threshold stress values with mean detachment stress values showing possible contribution from load transfer.

As discussed earlier Mishra *et al.* [33] proposed an empirical relationship based on the concept of dislocation particle interaction and suggests that the dislocation particle interaction leads to both the threshold stress and change in deformation kinetics. The expression is given by equation (9). Rosler *et al*. [14] have proposed a theoretical concept for the design of high temperature materials by dual- scale particle strengthening. Their theoretical analysis showed that it is possible to obtain a synergistic effect through interaction of small dispersoids and large reinforcement, provided high aspect ratio reinforcements are added. The creep strength parameter∑, is defined as

$$\sum = \sqrt{f_d}\left(1 + 2\left(2 + \frac{l}{R}\right) f_r^{\frac{3}{2}}\right) \tag{14}$$

At given applied stress σ, the effective stress causing dislocation motion is now termed as $\sigma' = \sigma/\wedge$ and equation (9) can be re-written as

$$\dot{\varepsilon} = 8.3 * 10^8 \frac{DGb}{k_B T}\left[exp\left(-104\sqrt{\frac{b}{\lambda}}\right)\right]\left(\frac{\sigma' - \sigma_0}{E}\right)^5 \quad (15)$$

Dislocation motion visualization

The plastic deformation of crystals involves the movement of dislocations in an array of obstacles. The focus of the present work is on movement of a dislocation against the resistance by various types of obstacles. Two major concern in dislocation motion visualization are nature and distribution of particles/points and interaction between points and dislocation.

Nature and distribution of points:

The distributed particles are of many kinds. The simplest case is distribution of like particles (strong or weak). The situation will become complicated for unlike particle distribution. However, most realistic systems contain more than one type of obstacles. Second important concern is the distribution of particles in a glide plane. Most of previous researchers used random distribution of points. Different random distributions are: binomial distribution, Poisson distribution, normal distribution and uniform distribution. Mean particle approach has also used in case of precipitation hardened alloy. Kulkarni et al [38] used the Wagner and Lifshitz and Slyozov (WLS) particle size distribution theory to better represent real alloys.

Interaction between particle and dislocation:

In the presence of point obstacles, a dislocation is fixed to form a cusp at an obstacle. The pinning angle ϕ is defined as the angle between two tangent vectors at a cusp as shown in Fig. 2. For a periodic array of obstacles whose spacing is L, the critical resolved shear stress (CRSS) τ_c is represented by

$$\tau_c = \frac{2\gamma}{bL}\cos\frac{\phi_c}{2} \quad (16)$$

where γ denotes the line tension and b denotes the Burgers vector.

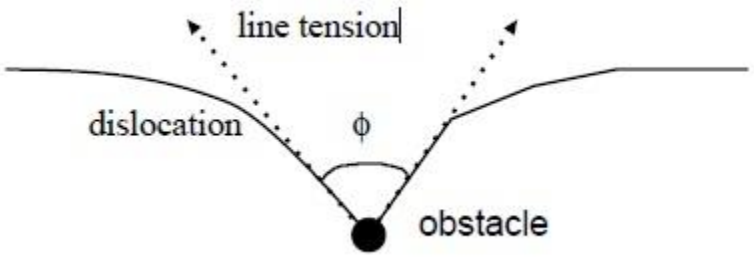

Figure 2. A cusp formed at an obstacle. The angle ϕ between two tangential vectors is called the pinning angle.

Foreman and Makin [40] performed computer simulation of the dislocation motion on a glide plane with randomly distributed obstacles which have the same critical angle. For obstacles

of a small critical angle (i.e. strong obstacles), the dislocation propagation resembles dendritic growth [41], while for a large critical angle (i.e. weak obstacles) the global form does not significantly deviate from the straight line. Also τ_c are well described by

$$\tau_c = \begin{cases} \frac{2\gamma}{bL}\left(\cos\frac{\phi_c}{2}\right)^{\frac{3}{2}}, & (\phi_c \geq \frac{5}{9}\pi) \\ \frac{1.6\gamma}{bL}\cos\frac{\phi_c}{2}, & (\phi_c \leq \frac{5}{9}\pi) \end{cases} \tag{17}$$

The dislocation line can form symmetrical or asymmetrical configurations [38] depending on the positional variation of the particles. Fig. 3 shows the calculation of the included angle for symmetric and asymmetric dislocation configurations.

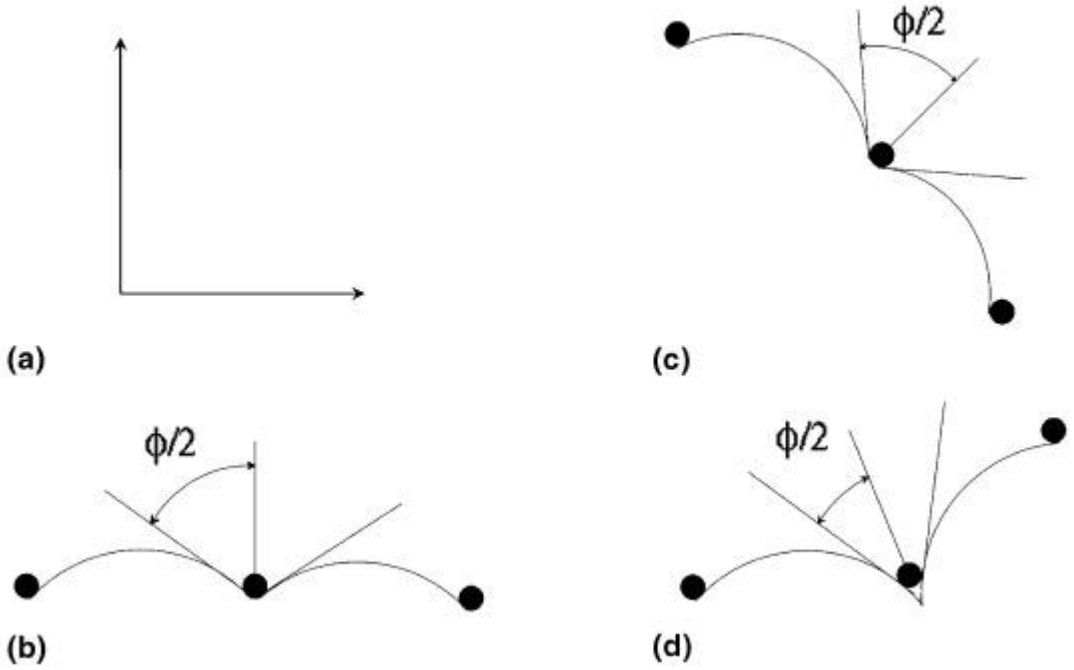

Figure 3. Calculation of included angle for different dislocation configurations, (a) coordinate frame, (b) symmetric dislocation configuration, (c) asymmetric dislocation configuration, and (d) asymmetric dislocation configuration.

Nanoindentation

Nanoindentation technique measures mechanical properties such as hardness, elastic modulus, etc., with the help of contact of known geometry. The main components in nanoindentation are the testing material, the sensors and actuators and the indenter tip. The most important tip geometry for nanoindentation testing is three-sided Berkovich pyramid made of diamond as shown in Fig. 4. It gives the same projected area to depth ratio as the four sided Vickers indenters. The contact radius a is given by expression [42]

$$a^3 = \frac{3}{4}\frac{PR}{E^*} \tag{18}$$

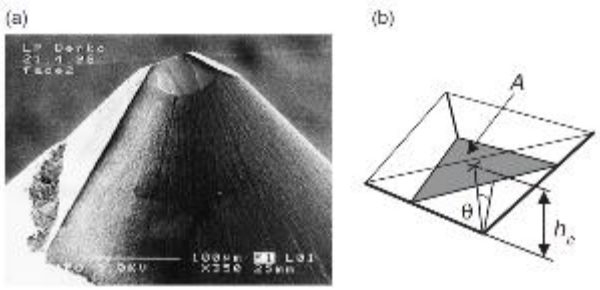

Figure 4. (a) High magnification SEM of Berkovich indenter tip (b) Schematic of indenter geometry.

where P is the applied load, R is the combined radius and E^* is the combined elastic modulus of the contacting bodies. The E^* is given by

$$\frac{1}{E^*} = \frac{(1-\nu^2)}{E} + \frac{\left(1-\nu'^2\right)}{E'} \tag{19}$$

where E' and ν', and E and ν, describe the elastic modulus and Poisson's ratio of the indenter and the specimen, respectively. The area of contact for a Berkovich indenter is given by

$$A = 24.5\, h_c^2 \tag{20}$$

where h_c is the distance as measured vertically from the indenter tip. The cross-section of profile of specimen surface at full load, and full unload for an elastic –plastic indentation as shown in Fig. 5.

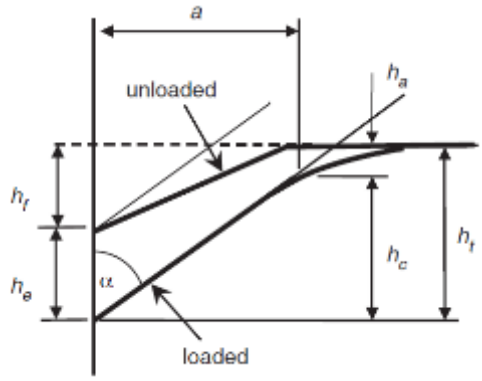

Figure 5. Cross-section of profile of specimen surface at full load, and full unload for an elastic-plastic indentation.

MODELING APPROACH

Genetic algorithm optimization approach

The cost function, J is defined as

$$J = \frac{\left[\sum_{i=S,D,HTS} w_i \left|\left(\frac{P_i}{(P_i)_{desired}}\right) - 1\right|\right]}{n} \tag{21}$$

where P_S is the strength, P_D ductility, P_{HTS} high temperature strength; w_S, w_D and w_{HTS} weight factors for strength, ductility, and HTS properties, respectively, and n is the number of properties involve in cost function.

Various considerations were taken in order to minimize the cost function:

- 100 Individuals were considered in each generation.
- Rank scales were used for the fitness scaling. The rank of the fittest individual was 1, the next fittest was 2 and so on.
- Population at each new generation consists of:
  1. 10 best individuals survived to the next generation.
  2. Probability of crossover was chosen 0.85 and rest were produce via mutation.
  3. For mutation, adaptive feasible technique was considered as it randomly generates directions that are adaptive with respect to the last successful or unsuccessful generation.
- The optimization was run until 100 generations were completed or the cost function did not vary significant for 25 successive generations.
- Different GA operator was considered for different conditions.

Notation used for variables:

- $[w_S\ w_D\ w_{HTS}]$= Weight factors for low temperature strength, ductility and high temperature strength properties.
- r (nm) is the radius of dispersoids particles.
- r_f (nm) is the radius of reinforced particles.
- f_r (%) is volume fraction of reinforcement.
- f_d (%) is volume fraction of dispersoids.
- r1 (nm) and r2 (nm) are the radius of dispersoids particles 1 and 2, respectively.
- f_d1 (%) and f_d2 (%) are the volume fractions of dispersoids particles 1 and 2, respectively.

The numerical values used for various constants and parameters were:
G=76 GPa, σ_o=17.4 GPa, K= 0.236 $MNm^{-3/2}$, b= 0.249 nm.
The optimization was carried out for condition:
I: 15 nm ≤ r ≤ 20 nm , 300 nm ≤ r_f ≤ 400 nm , f_r ≤ 15 %, T=1073 K, $\dot{\varepsilon} = 10^{-9}\ s^{-1}$
II: 2 nm ≤ r ≤ 4 nm , 500 nm ≤ r_f ≤ 1000 nm , f_r ≤ 15 %, T=1073 K, $\dot{\varepsilon} = 10^{-9}\ s^{-1}$
III:2 nm ≤ r ≤ 4 nm , 500 nm ≤ r_f ≤ 1000 nm , f_r ≤ 15 %, T=1123 K, $\dot{\varepsilon} = 10^{-6}\ s^{-1}$
IV: 1nm ≤ r ≤ 30nm , 400 nm ≤ r_f ≤ 1000 nm , f_r ≤ 15 %, T=1073 K, $\dot{\varepsilon} = 10^{-9}\ s^{-1}$
V: 1nm ≤ r ≤ 30 nm , 100 nm ≤ r_f ≤ 1000 nm , f_r ≤ 50 %, T=1073 K, $\dot{\varepsilon} = 10^{-9}\ s^{-1}$
VI: Two types of dispersoids were considered.
10 nm ≤ r1 ≤ 100 nm,1 nm ≤ r2 ≤ 3 nm, 400 nm ≤ r_f ≤ 1000 nm , f_r ≤ 15 %, T=1073 K, $\dot{\varepsilon} = 10^{-9}\ s^{-1}$
VII: Different GA operator conditions were considered as summarized in Table 2. Rest conditions were same as in condition VI. The chosen weightage factor was [1 1 10].

Table 2. Different combinations of GA operators.

GA operator	**1**	**2**	**3**	**4**	**5**
Selection	Tournament	Uniform	Uniform	Tournament	Roulette
Crossover	Heuristic	Arithmetic	Heuristic	Arithmetic	Heuristic
Mutation	Adaptive feasible	Adaptive feasible	Adaptive feasible	Adaptive feasible	Adaptive feasible

The further optimization was carried out for following conditions as summarized in Table 3.

Table 3. Conditions for different GA optimization.

Condition	[r f_d r_f f_r] / [r1 r2 f_d1 f_d2 r_f f_r]		Temperature (K)	Strain rate (s^{-1})
	LB	UB		
VIII	[1 1 100 1]	[30 5 1000 50]	1073	10^{-9}
IX	[1 1 100 2]	[30 5 1000 30]	1073	10^{-9}
X	[10 1 1 1 400 5]	[100 3 5 3 1000 15]	1073	10^{-9}

Different GA operator conditions were considered for conditions VIII, IX and X as given in Table 4.

Table 4. Different GA operator combination.

Conditions	GA operator		
	Selection	Crossover	Mutation
VIII (1)	Uniform	Heuristic	Adaptive feasible
VIII (2)	Uniform	Arithmetic	Adaptive feasible
VIII (3)	Roulette	Heuristic	Adaptive feasible
VIII (4)	Roulette	Arithmetic	Adaptive feasible
VIII (5)	Tournament	Heuristic	Adaptive feasible
VIII (6)	Tournament	Arithmetic	Adaptive feasible
IX (1)	Tournament	Arithmetic	Adaptive feasible
IX (2)	Roulette	Heuristic	Adaptive feasible
X (1)	Tournament	Arithmetic	Adaptive feasible
X (2)	Roulette	Heuristic	Adaptive feasible

Four cases were considered on the basis of different weight factors for three properties except condition VII. The desired low temperature strength was taken 900 MPa, ductility 10 % and high temperature strength of 100 MPa and 150 MPa were considered. Case I involved only low temperature strength design criteria. In other cases ductility and high temperature design criteria were introduced along with low temperature strength. The desired low temperature strength was taken 900 MPa, ductility 10 % and high temperature strength 150 MPa for condition VIII. In case of conditions IX and X, low temperature strength was considered 1500 MPa although ductility and high temperature strength same as in condition VIII.

EXPERIMENTAL

Mechanical milling

Gas atomized Ni-20Cr powder with nominal composition of Ni-19.6Cr-0.2Fe-0.8Mn-0.9Si (wt.%) and mean particle size of 23.6±1.1 µm, yttrium oxide (yttria/Y_2O_3) powder with high purity (99.99%) and mean particle size of 30-40 nm and aluminum oxide (alumina/ Al_2O_3) powder with

99.99% purity and mean particle size of 300-400 nm were procured from the American Elements Inc.

Powder batches were prepared in a glove box under high purity argon atmosphere and poured into hardened steel grinding vial (Spex 8001). In order to minimize powder agglomeration and cold welding during milling, 1 wt.% stearic acid was added to the powder mix prior to the ball milling process as a process control agent (PCA). The ball milling was carried out in a Spex 8000M shaker mixer/mill using steel balls 5 mm in diameter and a ball to powder ratio (BPR) of 10:1 (the powder mass and the ball mass of each batch was 10 g and 100 g, respectively). A variety of Ni-based alloys with different milling durations (0 h, 2 h and 4 h) and nominal compositions (Ni-20Cr, Ni-20Cr-1.2Y_2O_3, Ni-20Cr-1.2Y_2O_3-5Al_2O_3, wt.%) were milled.

For preparing the Ni-20Cr-1.2Y_2O_3-5Al_2O_3 powder, Ni-20Cr-1.2Y_2O_3 was first milled for 2 h, and then 5 wt.% Al_2O_3 powder was added to the milled Ni-20Cr-1.2Y_2O_3 alloy and subsequently ball milled to distribute all the Al_2O_3 particles homogeneously. In our former experiments, Al_2O_3 powder was only blended (i.e. milled without the steel balls) with the milled Ni-20Cr-1.2Y_2O_3 powder, and the results were unsatisfactory because all the Al_2O_3 powder particles were found to be mostly located on the prior particle boundaries after consolidation.

X-ray diffraction (XRD) experiments of the as-milled powders were performed using a Siemens 5000D diffractometer with Cu-Kα radiation. Modifications such as $k\alpha_2$ Rachinger and background correction by Sonnerveld were applied to XRD patterns using the Powder-X software [43]. Lattice parameters, crystallite size and lattice strain were calculated based on the Nelson-Riley extrapolation [44] and Williamson-Hall (W-H) formula, respectively [45]. In this study, for the standard sample, a fully annealed unmilled Ni-20Cr powder was used.

The morphology and size distribution of the as-received powder batches and as-milled powder were analyzed using a Zeiss Supra 35 field-emission gun scanning electron microscope (FEG-SEM). The milled powders were hot mounted in phenolic powder and polished to 0.05 μm. The cross section of the hot mounted and polished milled powders were observed in backscattered electron (BSE) mode in the FEG-SEM. The SEM and high angle annular dark field (HAADF) micrographs were obtained by scanning transmission electron microscopy (STEM).

The ball milling runs were the first stage of materials processing. First, a run was made to blend the powder in the vial without the balls. The SPEX 8000M mixer/mill was used for both blending and high energy ball milling. Figure 6a and b show the Labconco glove box (for mixing the powder under the argon atmosphere) and SPEX mixer/mill (for blending and ball milling experiments), respectively, used in these experiments.

(a) (b)

Figure 6. a) The Labconco glove box, b) A SPEX 8000M Mixer/Mill available at the Advanced Materials Laboratory, University of Idaho.

Spark plasma sintering

The ball milled powder was consolidated via SPS using a Dr. Sinter Lab SPS-515S machine (SPS Syntex Inc., Kanagawa, Japan) with maximum capacity of 30 kN and 1500 A. Tri-Gemini cylindrical graphite dies with an inner diameter of 12.7 mm and an outer diameter of 38 mm were used. The inner surface of the die and radial surfaces of punches were covered with a graphite foil (0.25 mm in thickness) to facilitate the removal of the sintered specimens. In order to inhibit the diffusion of carbon from the punches and graphite foil to the powder mixture, a thin niobium foil (0.06 mm in thickness) was placed between the powder and the graphite foils. The die was wrapped in graphite felt (4 mm in thickness) to minimize heat loss by thermal radiation.

All the SPS experiments were performed under vacuum (7×10^{-3} Torr or 0.9 Pa), using a heating rate of 100 ^{o}C/min and force of 10 kN (equals to about 80 MPa considering punch configuration used in this study). An intermediate 15 min dwell time at 450 ^{o} C (with 4.5 kN applied force) was given for all the SPS runs to allow the stearic acid to volatilize. Following that, the temperature was ramped up to different levels (600 ^{o}C, 900 ^{o}C, 1000 ^{o}C and 1100 ^{o}C), kept at those temperatures for different times (5 and 30 min), and cooled down at the rate of about 50 ^{o}C/min. The temperature was monitored by a K-type thermocouple that was inserted into a hole in the die such that the tip was located 6 mm away from the sintering powder. The final product was in the form of a disk with dimensions of 12.5 mm in diameter and 8 mm in thickness. All the Ni-based alloys processed in this study varying in milling times, compositions, sintering temperatures and times are listed in Table 5.

Table 5. Different milling times, SPS temperatures, SPS dwell times and alloy compositions in processing Ni-based ODS alloys considered for current study

Purpose	Alloy (wt.%)	Milling Time (h)	SPS Parameters	Alloy Code
Effect of Milling Time	Ni-20Cr-1.2Y_2O_3	0	1100 ^oC/ 30 min	A
	Ni-20Cr-1.2Y_2O_3	2	1100 ^oC/ 30 min	B
	Ni-20Cr-1.2Y_2O_3	4	1100 ^oC/ 30 min	C
Effect of SPS Parameters	Ni-20Cr-1.2Y_2O_3	2	600 ^oC/ 5 min	D
	Ni-20Cr-1.2Y_2O_3	2	900 ^oC/ 5 min	E
	Ni-20Cr-1.2Y_2O_3	2	1000 ^oC/ 5 min	F
	Ni-20Cr-1.2Y_2O_3	2	1100 ^oC/ 5 min	G
	Ni-20Cr-1.2Y_2O_3	2	1100 ^oC/ 30 min	B
Effect of Alloy Composition	Ni-20Cr	2	1100 ^oC/ 30 min	H
	Ni-20Cr-1.2Y_2O_3	2	1100 ^oC/ 30 min	B
	Ni-20Cr-1.2Y_2O_3-5Al_2O_3	2.5	1100 ^oC/ 30 min	I

Density and Mechanical characterization

Upon SPS, physical density of the bulk specimens was measured using Archimedes' principle with at least six measurements for each specimen. The final relative density was calculated as the ratio between the measured density and the theoretical density of each composition. The sample surface for microhardness testing was mechanically polished using standard metallographic procedures involving grinding and polishing down to 0.5 μm finish. The Vickers microhardness tests were performed with a Leco LM100 microhardness tester at 0.5 kgf (~5 N) load applied for 15 s on the sintered samples. The microhardness tests were repeated on random spots in the center of each specimen up to 10 times.

Compression testing was performed on an Instron 5982 machine at both 25 °C and 800 ^oC applying a nominal strain rate of 10^{-3} s^{-1}. The disk shaped SPSed specimens were electro-discharge machined to a square-based rectangular prism shape with dimensions of 4×4×6 mm.

Microstructural characterization

Electron backscattered diffraction (EBSD) study was performed using a JEOL JSM-6610LV scanning electron microscope (SEM) equipped with an EDAX/TSL Hikari EBSD system. The transmission electron microscopy (TEM) specimens were mechanically thinned and electropolished at a temperature of about -35 ^oC using a solution of nitric acid and methanol (10:90, vol.%) and a Fischione twin-jet polisher operating at 30 V. Microstructural studies were conducted using a JEOL-2010 TEM operating at 200 kV. A focused ion beam (FIB) was used to prepare a

TEM foil from the specimen with a composition of Ni-20Cr-1.2Y_2O_3-5Al_2O_3 due to the unsatisfactory results after electropolishing (likely caused by low conductivity of this alloy). FIB experiment was done by using an FEI Quanta 3D FEG instrument with a Ga-ion source.

Creep testing

High temperature compression creep experiments were performed on three different specimens namely Ni-20Cr, Ni-20Cr-1.2Y_2O_3 and Ni-20Cr-1.2Y_2O_3-5Al_2O_3 (2320 Model ATS instruments, USA). The equipment can carry out tests in compression and tension mode at high temperature with precision of ±3 K. Strain was measured by highly precise extensometer. The creep frame has 5:1 lever arm ratio. The specimen was kept in the center of 3210 series split furnace to maintain a constant temperature along the gage of samples. Split furnace has capability to reach temperature till 1100 ^{0}C. Samples were prepared through SPS. All the SPS experiments were performed using a heating rate of 100 ^{0}C /min and 10 kN force (equals to about 80 MPa) under vacuum. An intermediate 15 min dwell at 450 ^{0}C (with 4.5 kN applied force) was provided for all the SPS runs in order to remove the stearic acid. Following that, the temperature was ramped up to 1100^{0}C and kept at that temperature for 30 min, and then cooled down in the vacuum chamber.

Nanoindentation experiment

Nano-indentation experiments were carried out using Hysitron Triboindenter (Hysitron, Inc., Minneapolis, MN) at room temperature using a Berkovich diamond tip. The room temperature hardness and modulus maps were evaluated on Ni-20Cr-1.2Y_2O_3-5Al_2O_3 sample. The indentation was performed at a load of 10000 µN with loading rate of 2000 µN /sec, hold time of 2 seconds and unloading rate of 2000 µN /sec.

3D atom probe

Atom probe tomography (APT) studies were performed on Ni-20Cr-1.2Y_2O_3-5Al_2O_3 sample. Samples for APT studies were prepared by dual-beam focused ion-beam (FIB) technique through Nova Nanolab 200 system using GA ion beam. The APT experiments were conducted using LEAP 3000XTM local electrode atom probe system from Cameca Instruments Inc. Data analysis was carried out using IVAS 3.6.2TM software. Three dimensional atom probe (3DAP) reconstruction of size 40*40*180 nm^3 was considered.

RESULTS AND DISCUSSION

Genetic algorithm optimization

Condition I

Table 6 shows the results obtained for four different design criteria. Dispersoid radius tends to lie near the lower limit of 15 nm for all cases. Low temperature strength is around 670 MPa, which is lesser than the required strength of 900 MPa. GA plots for case 1([1 0 0]) and 2 ([10 1 1]) are shown in Figs. 7 and 8, respectively. GA plots here describe the fitness value for the cost function at each generation and value of best individual for all variables. The best fitness value for

case 1 is 0.42166. The mean fitness value is 0.42166 and for the case 2, best and mean fitness value is 0.41405 and 0.41406, respectively. For all other cases similar results were obtained. The high temperature strength varies from 33-43 MPa with creep rate 10^{-9} at 800ºC. The ductility for all cases is close to desired 10 %.

Table 6. Optimized microstructure for different design criteria for condition I.

Case	**[1 0 0]**	**[10 1 1]**	**[1 1 1]**	**[1 1 10]**
r (nm)	15	15.01	15	15.08
f_d (%)	5	5	3.84	4.88
r_f (nm)	318	304	300	305
f_r (%)	13.70	7.06	8.21	7.56
LTS (MPa)	678.6	678.4	661.1	676.2
Ductility	-	0.090	0.105	0.1005
HTS (MPa)	-	33. 5	41.8	43.0

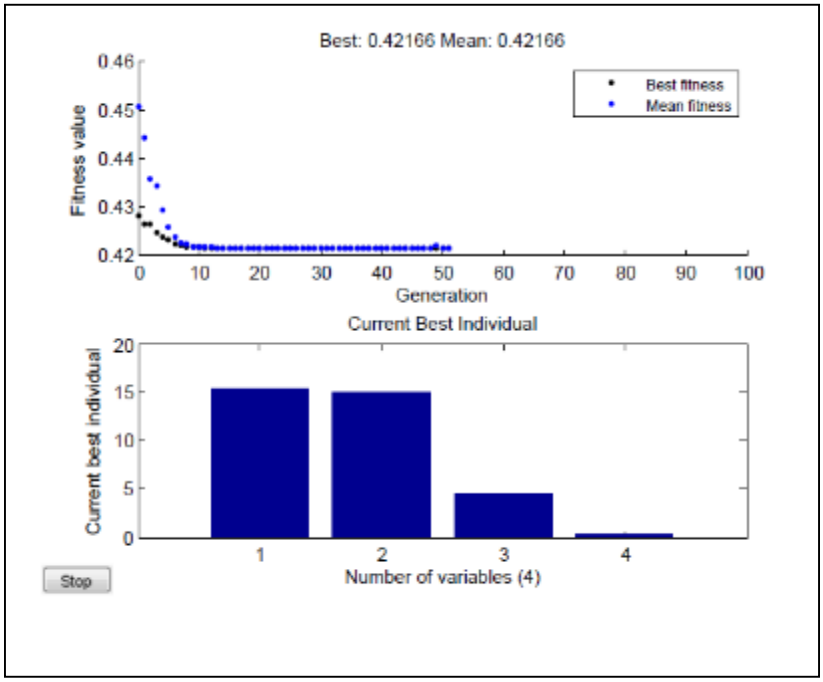

Figure 7. GA plot of case [1 0 0] for condition I.

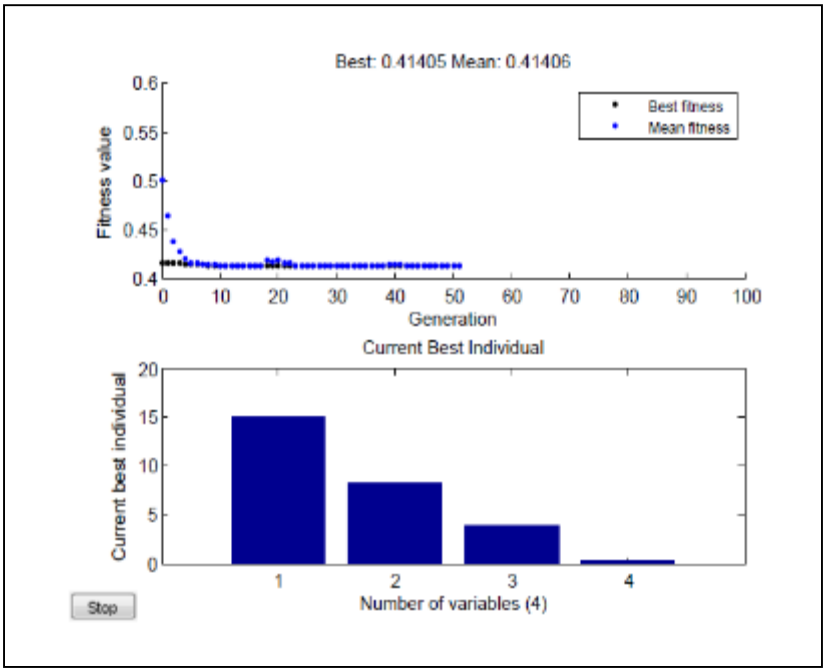

Figure 8. GA plot of case [10 1 1] for condition I.

Condition II

Table 7 shows the results obtained for four different design weightage of condition II. In this condition, the dispersoids radii come close to 3 nm for all cases. The low temperature strength is significant and at or above 900 MPa. The GA plots are shown in Figs. 9 and 10 for the case 1 ([1 0 0]) and case 2 ([10 1 1]). Here, best and mean fitness values for case 1 are 0.035841 and 0.035842, respectively, and for case 2, 0.013055 and 0.013072. The ductility is close to 10 %. This condition shows very good high temperature strength 130-150 MPa.

Table 7. Optimized microstructure for different design weightage for condition II.

Case	**[1 0 0]**	**[10 1 1]**	**[1 1 1]**	**[1 1 10]**
r (nm)	3.00	2.96	3.44	2.58
f_d (%)	3	3	4.09	2.58
r_f (nm)	797	642	971	697
f_r (%)	13.01	10.20	8	8.92
LTS (MPa)	932.1	900.0	902.5	989.3
Ductility	-	0.0906	0.0996	0.0967

HTS (MPa)	-	132.0	145.1	150.2

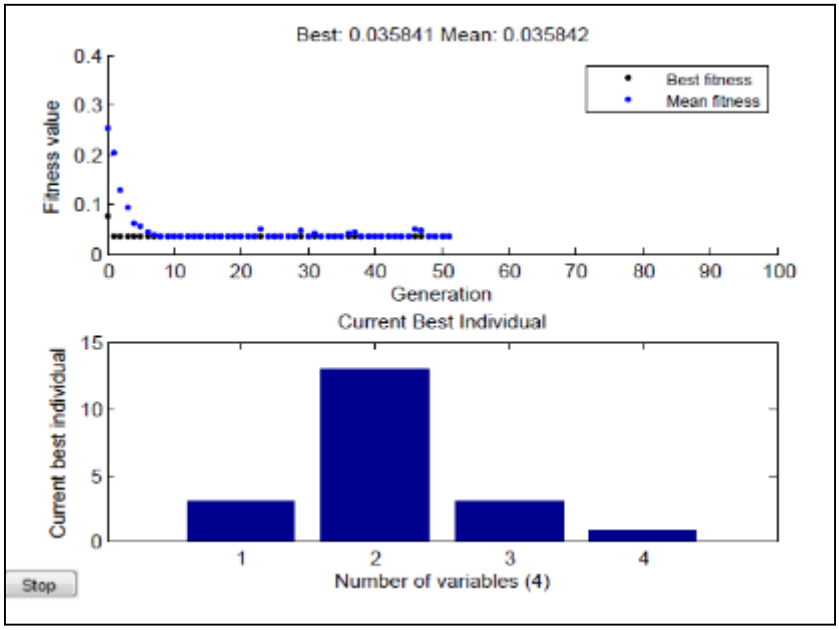

Figure 9. GA plot of case [1 0 0] for condition II.

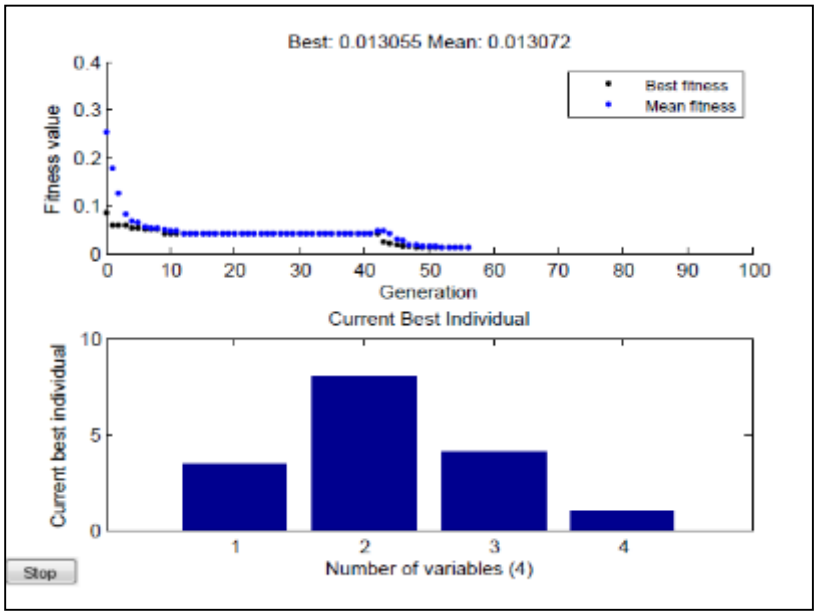

Figure 10. GA plot of case [10 1 1] for condition II.

Condition III

Table 8 shows the results obtained for four different design weightage of condition III. In this condition, the predicted dispersoid radii are close to 2.5 nm for all the cases. The low temperature strength is at or above 900 MPa. The GA plots are shown in Figs. 11 and 12 for the case 1 ([1 0 0]) and case 2 ([10 1 1]). Here, best and mean fitness value for case 1 are 0 and 0.131,

respectively, and for case 3 are 0.21 and 0.319. The ductility is close to 10 %. This condition shows very good high temperature strength 210-250 MPa.

Table 8. Optimized microstructure for different design weightage for condition III.

Case	**[1 0 0]**	**[10 1 1]**	**[1 1 1]**	**[1 1 10]**
r (nm)	2.27	2.16	2.85	3.34
f_d (%)	3.317	3.002	2.134	2.759
r_f (nm)	887	531	681	596
f_r (%)	10.265	9.03	9.873	9.222
LTS (MPa)	1002.3	984.5	889.2	802.8
Ductility	-	0.1003	0.0997	0.1006
HTS (MPa)	-	212.8	225.6	242.8

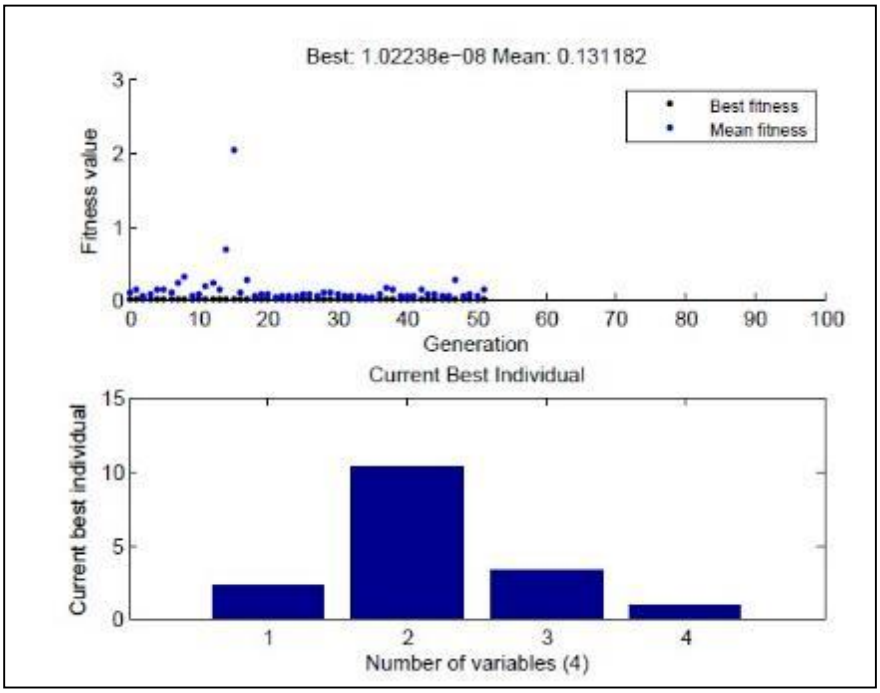

Figure 11. GA plot of case [1 0 0] for condition III.

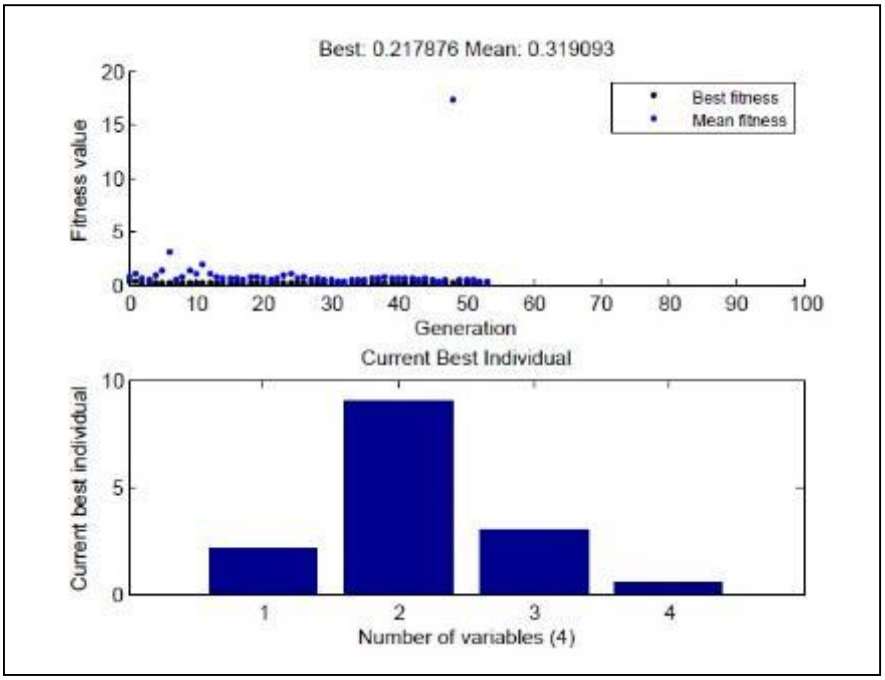

Figure 12. GA plot of case [10 1 1] for condition III.

Condition IV

Table 9 shows the results obtained for four different design weightage of condition IV. In this condition, the reinforcement fraction is approx. 10% for all cases. The GA plots are shown in Figs. 13 and 14 for the case 2 ([10 1 1]) and case 4 ([1 1 10]). Here, best and mean fitness values for case 2 are 0.050689 and 0.07771, respectively, and for case 4, 0.078014 and 0.10299.

Table 9. Optimized microstructure for different design weightage for condition IV.

Case	**[1 0 0]**	**[10 1 1]**	**[1 1 1]**	**[1 1 10]**
r (nm)	4.60	4.53	3.18	6.10
f_d (%)	3.10	3.01	2.06	4.71
r_f (nm)	756	786	929	690
f_r (%)	11.06	10	10.00	10.01
LTS (MPa)	900.0	900.0	964.8	874.1
Ductility	-	0.0920	0.0990	0.0795
HTS (MPa)	-	87.2	90.8	100.9

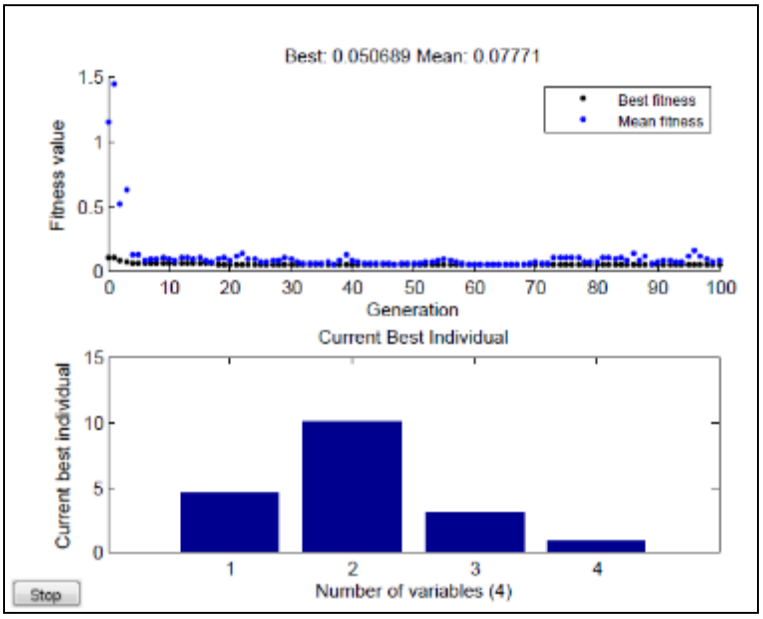

Figure 13. GA plot of case [10 1 1] for condition IV.

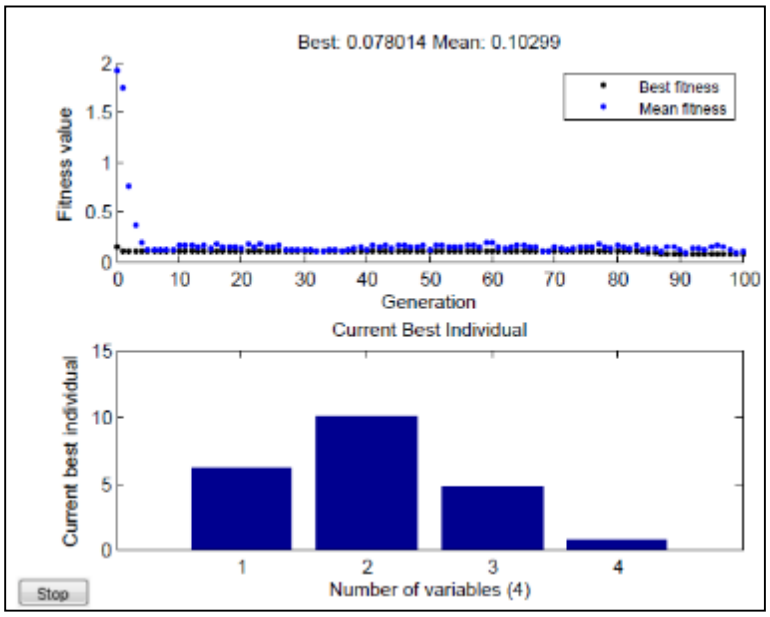

Figure 14. GA plot of case [1 1 10] for condition IV.

Condition V

Table 10 shows the results obtained for four different design weightage of condition V. Here, less restriction on parameters was selected. The GA plots are shown in Figs. 15 and 16 for the case 2 ([10 1 1]) and case 4 ([1 1 10]). Here, best and mean fitness values for case 2 are 0.031984 and 0.043681, respectively, and for case 4 are 0015974 and 0.20865. The ductility is close to 10 %. This condition shows high temperature strength 84-100 MPa.

Table 10. Optimized microstructure for different design weightage for condition V.

Case	[1 0 0]	[10 1 1]	[1 1 1]	[1 1 10]
r (nm)	4.13	4.49	4.84	6.68
f_d (%)	2.49	2.96	3.83	4.65
r_f (nm)	477	991	571	205
f_r (%)	16.30	9.09	8.22	13.62
LTS (MPa)	900.6	900.0	920.3	846.8
Ductility	-	0.10	0.10	0.088
HTS (MPa)	-	84.8	97.9	99.9

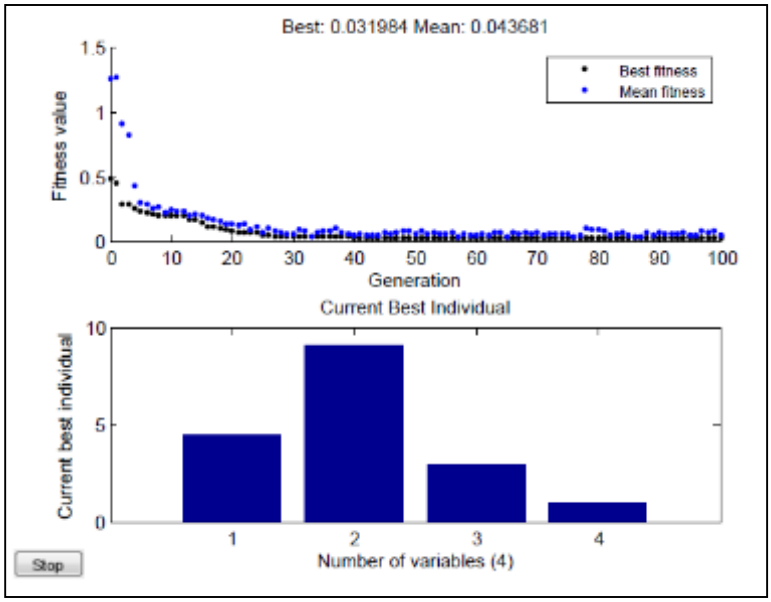

Figure 15. GA plot of case [10 1 1] for condition V.

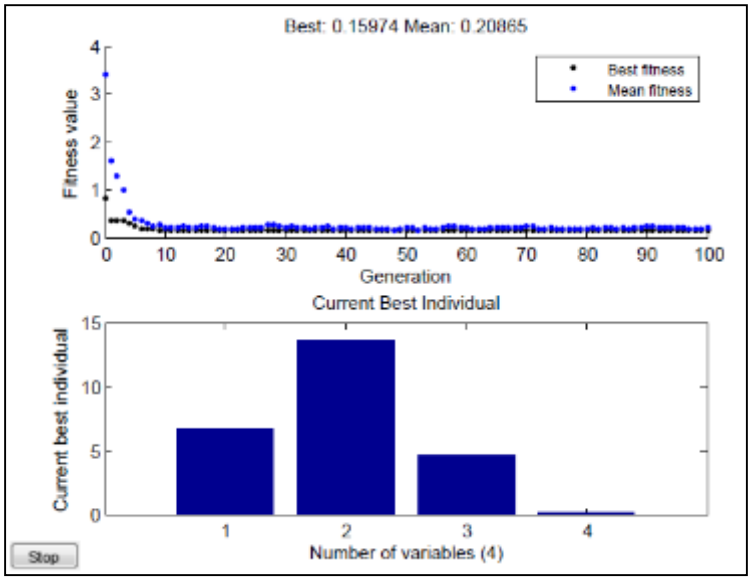

Figure 16. GA plot of case [1 1 10] for condition V.

Condition VI

Table 11 shows the results obtained for four different design weightage of condition VI. With the addition of two different dispersoids, high temperature strength comes close to 150 for two cases. The GA plots are shown in Figs. 17 and 18 for the case 2 ([10 1 1]) and case 4 ([1 1 10]). Here, best and mean fitness values for case 2 are 0.17229 and 0.23986, respectively, and for case 4, 0.12959 and 0.26146.

Table 11. Optimized microstructure for different design weightage for condition VI.

Case	**[1 0 0]**	**[10 1 1]**	**[1 1 1]**	**[1 1 10]**
r1 (nm)	39.87	41.25	30.68	22.71
r2 (nm)	2.79	2.81	2.29	2.28
f_d 1(%)	3.11	4.98	4.69	3.13
f_d 2(%)	1.12	1.13	3.00	2.91
r_f (nm)	335	594	819	906
f_r (%)	8.26	5.93	4.35	6.01
LTS (MPa)	899.9	926.9	1085.6	1108.9
Ductility	-	0.098	0.099	0.10
HTS (MPa)	-	77.5	149.8	150.2

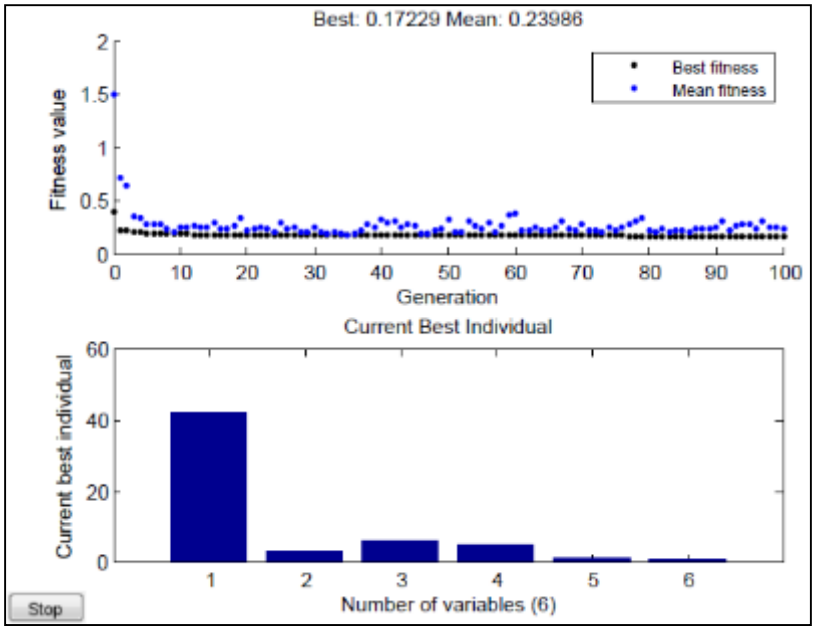

Figure 17. GA plot of case [10 1 1] for condition VI.

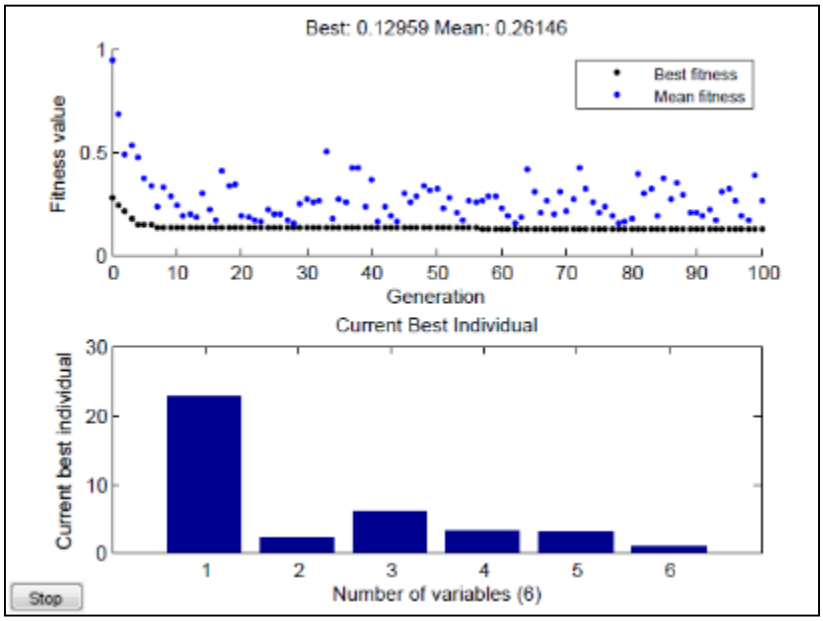

Figure 18. GA plot of case [1 1 10] for condition VI.

Condition VII

Table 12 shows the results obtained for different GA operator conditions with weightage [1 1 10] of condition VII. The GA plots are shown in Figs. 19(a)-(e) for all the cases. High temperature strength is close to 150 MPa for all cases. There is significant variation in dispersoid radius.

Table 12. Optimized microstructure for different design weightage for condition VII.

Case	1	2	3	4	5
r1 (nm)	16.20	20.33	22.54	15.78	22.71
r2 (nm)	1.98	1.68	2.83	2.20	2.28
f_{d1} (%)	3.90	4.94	2.81	1.56	3.13
f_{d2} (%)	2.05	1.41	4.64	2.47	2.91
r_f (nm)	631	535	899	545	906
f_r (%)	7.87	11.36	11.86	10.90	6.01
LTS (MPa)	1233.4	1110.9	1105.2	1219.0	1108.9
Ductility	0.1	0.1	0.1	0.10	0.10
HTS (MPa)	150.0	147.8	148.0	150.0	150.2

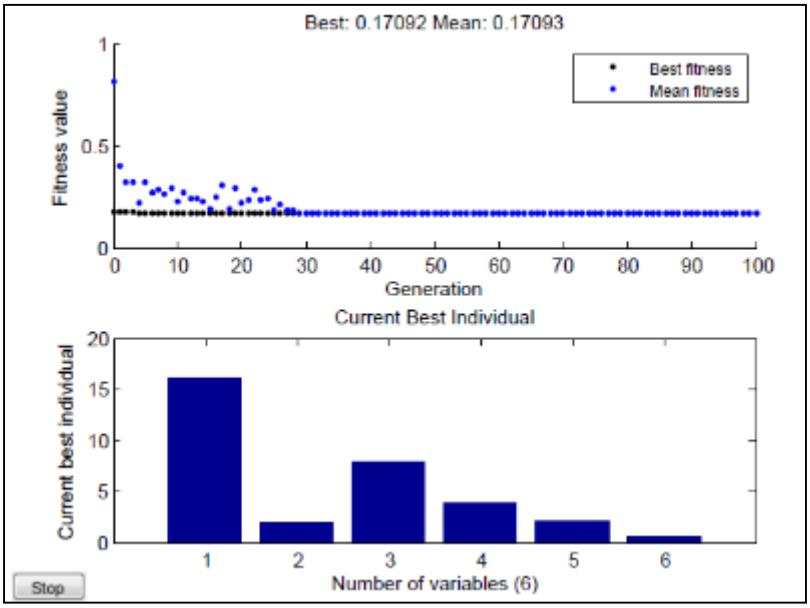

Figure 19(a). GA plot of case 1 for condition VII.

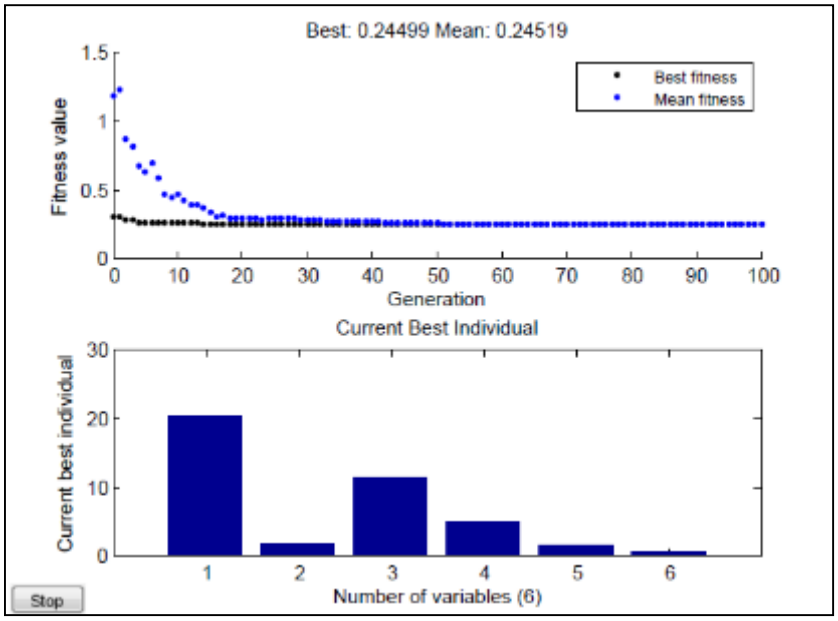

Figure 19(b). GA plot of case 2 for condition VII.

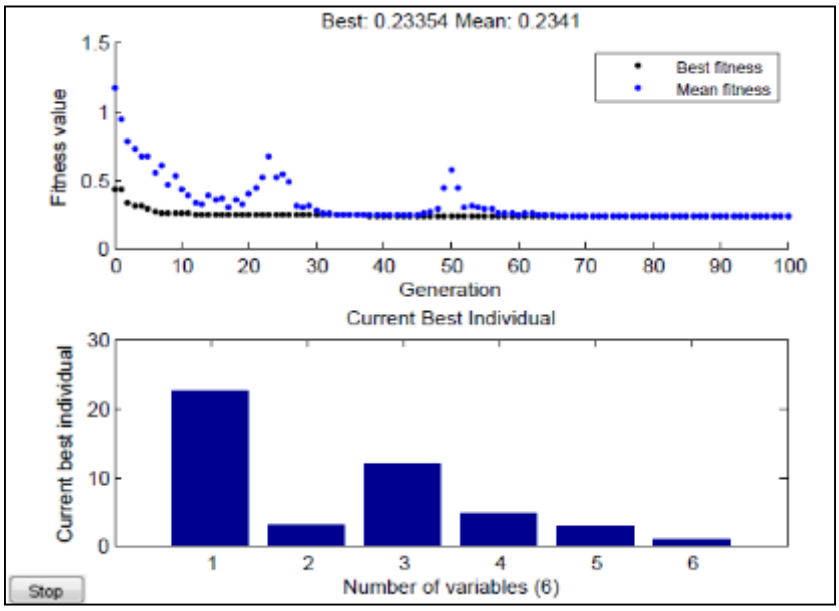

Figure 19(c). GA plot of case 3 for condition VII.

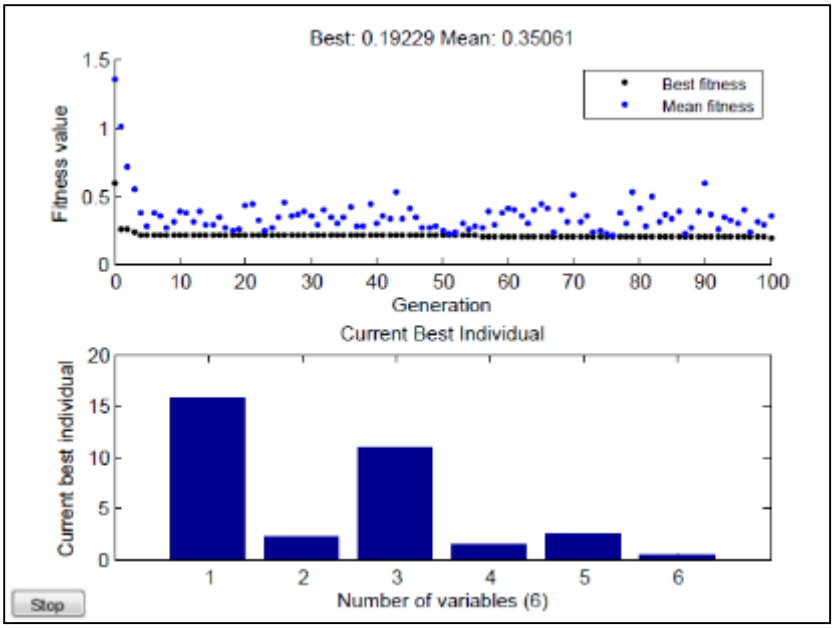

Figure 19(d). GA plot of case 4 for condition VII.

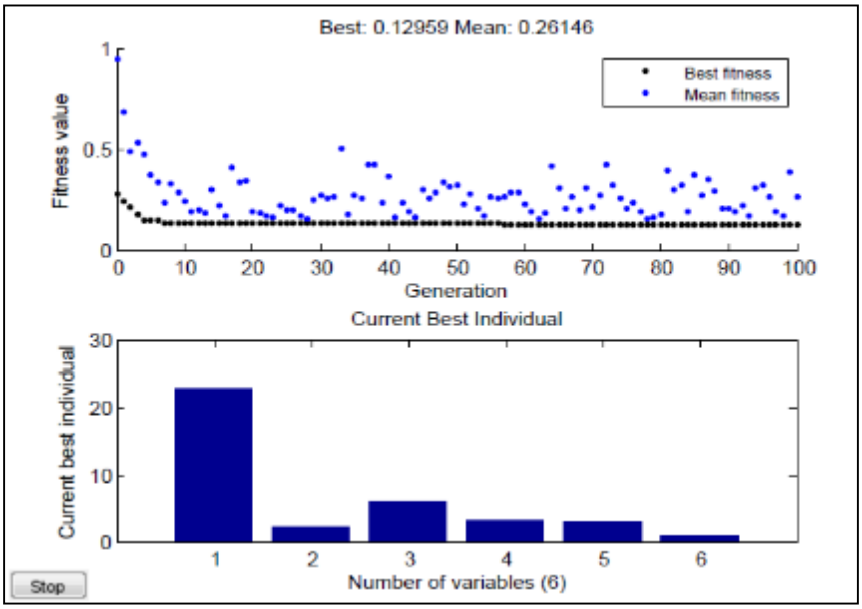

Figure 19(e). GA plot of case 5 for condition VII.

Condition VIII (1)

Table 13 shows the results obtained for four different design weightage of condition VIII (1). In this condition, the reinforcement fraction is approximate 7% for all cases except [1 0 0] case. The GA plots are shown in Figs. 20 and 21 for the case 2 ([10 1 1]) and case 4 ([1 1 10]). Here, best and mean fitness values for case 2 are 0.05897 and 0.059039, respectively, and for case 4, 0.073939 and 0.076446.

Table 13. Optimized microstructure for different design weightage for condition VIII (1).

Case	[1 0 0]	[10 1 1]	[1 1 1]	[1 1 10]
r (nm)	4.73	4.06	5.75	3.52
f_d (%)	3.28	5	4.84	4.34
r_f (nm)	759	409	349	579
f_r (%)	16.44	7.05	7.21	7.72
LTS (MPa)	900	1059	900	1098
Ductility	-	0.1	0.1	0.1
HTS (MPa)	-	148	103	149

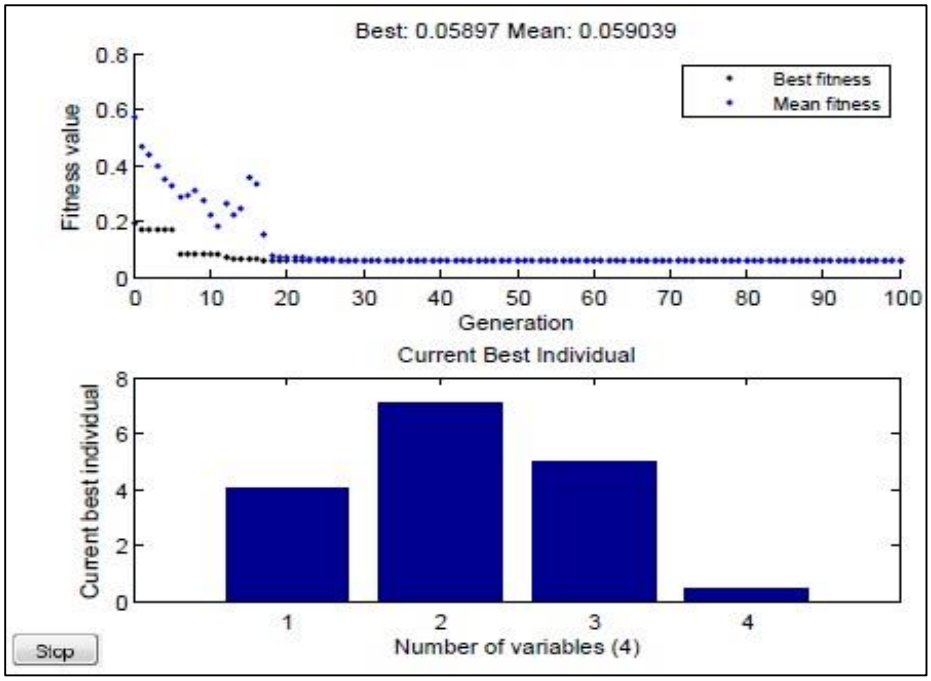

Figure 20. GA plot of case [10 1 1] for condition VIII (1).

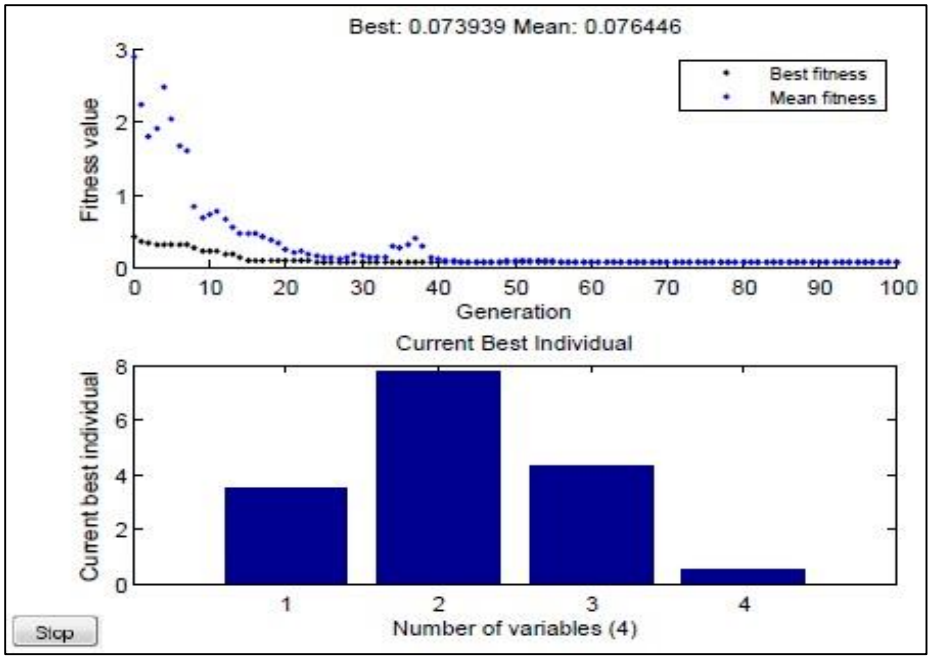

Figure 21. GA plot of case [1 1 10] for condition VIII (1).

Condition VIII (2)

Table 14 shows the results obtained for four different design weightage of condition VIII (2). The GA plots are shown in Figs. 22 and 23 for the case 2 ([10 1 1]) and case 4 ([1 1 10]). Here, best and mean fitness values for case 2 are 0.28234 and 0.28261, respectively, and for case 4, 0.14449 and 0.14483. High temperature strength is considerably low for the case [10 1 1] and [1 1 1].

Table 14. Optimized microstructure for different design weightage for condition VIII (2).

Case	**[1 0 0]**	**[10 1 1]**	**[1 1 1]**	**[1 1 10]**
r (nm)	4.19	2.89	3.68	3.70
f_d (%)	2.57	1.11	1.90	4.26
r_f (nm)	525	521	762	421
f_r (%)	13.46	15.92	12.01	10.57
LTS (MPa)	901	883	892	1065
Ductility	-	0.065	0.085	0.1
HTS (MPa)	-	79	78	150

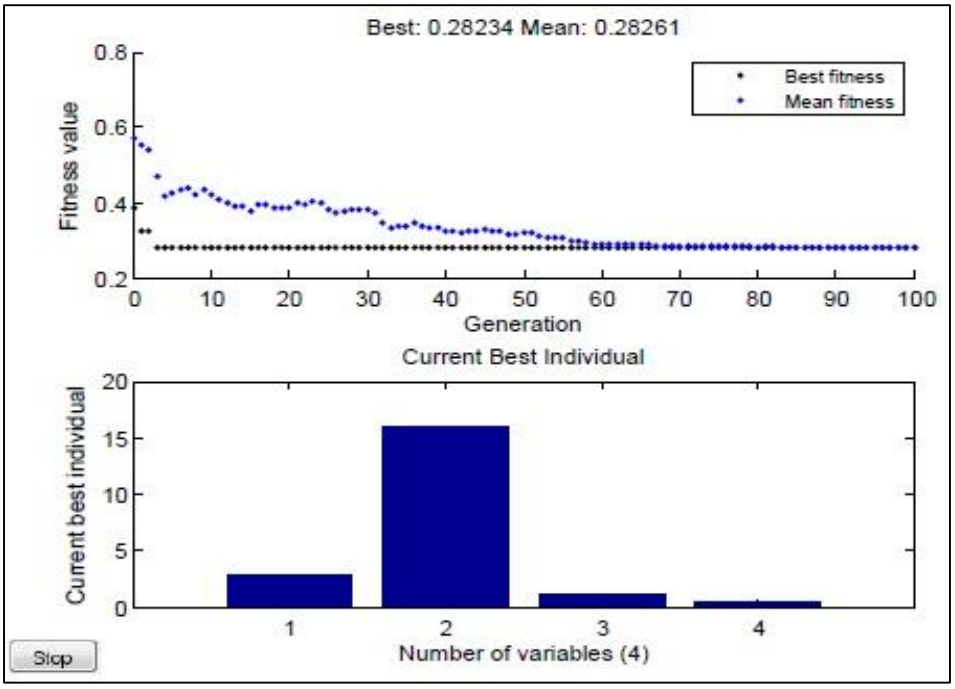

Figure 22. GA plot of case [10 1 1] for condition VIII (2).

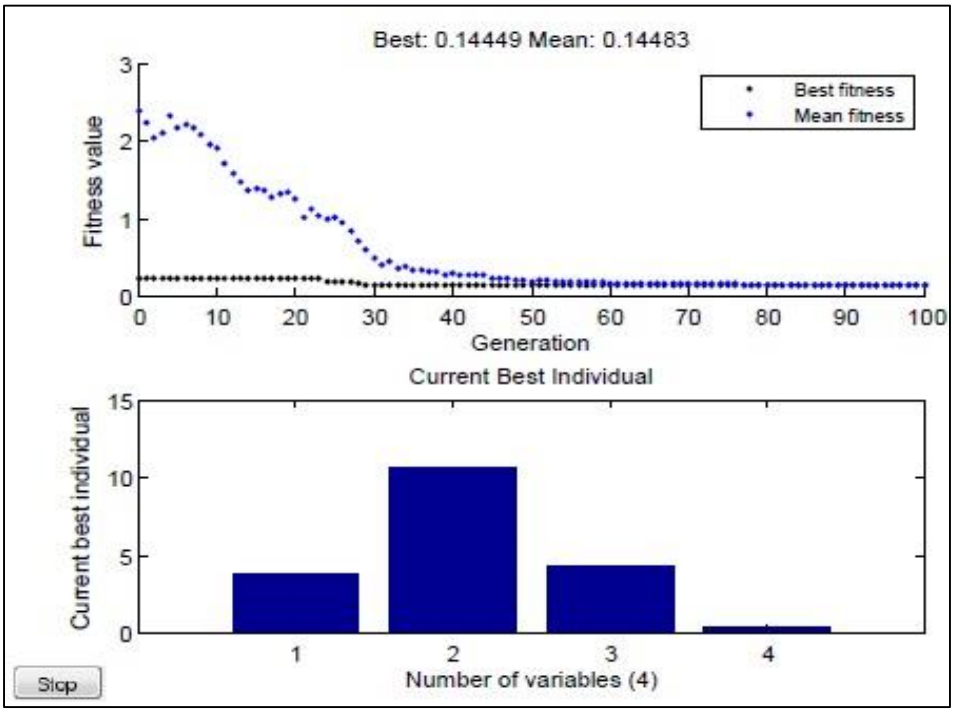

Figure 23. GA plot of case [1 1 10] for condition VIII (2).

Condition VIII (3)

Table 15 shows the results obtained for four different design weightage of condition VIII (3). Low temperature strength is above 900 MPa for all the cases. The GA plots are shown in Figs.

24 and 25 for the case 2 ([10 1 1]) and case 4 ([1 1 10]). Here, best and mean fitness values for case 2 are 0.059145 and 0.07009, respectively, and for case 4, 0.10667 and 0.28696.

Table 15. Optimized microstructure for different design weightage for condition VIII (3).

Case	[1 0 0]	[10 1 1]	[1 1 1]	[1 1 10]
r (nm)	4.36	4.07	5.35	3.47
f_d (%)	2.78	5	4.2	4.15
r_f (nm)	699	993	793	334
f_r (%)	20.48	7.05	7.85	9.19
LTS (MPa)	900	1058	900	1094
Ductility	-	0.1	0.1	0.1
HTS (MPa)	-	150	97	150

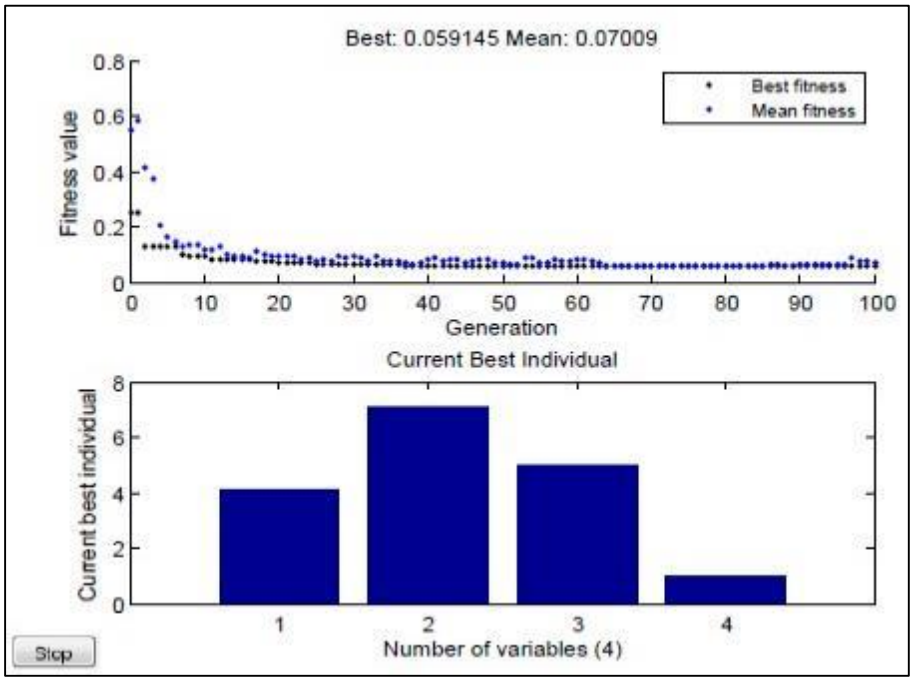

Figure 24. GA plot of case [10 1 1] for condition VIII (3).

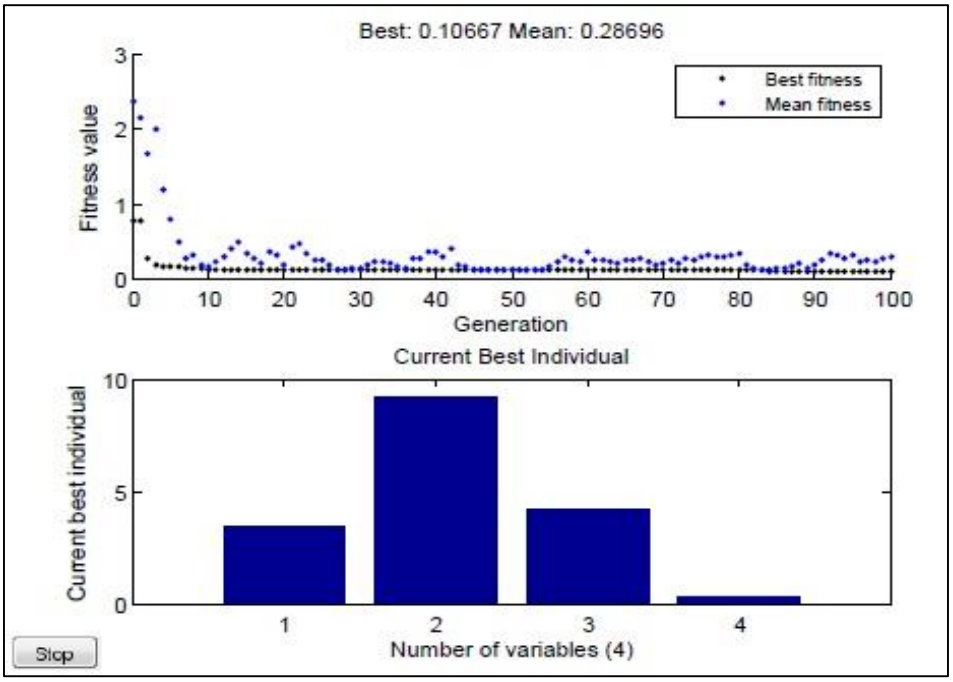

Figure 25. GA plot of case [1 1 10] for condition VIII (3).

Condition VIII (4)

Table 16 shows the results obtained for four different design weightage of condition VIII (4). The GA plots are shown in Figs. 26 and 27 for the case 2 ([10 1 1]) and case 4 ([1 1 10]). Here, best and mean fitness values for case 2 are 0.091904 and 0.092034, respectively, and for case 4, 0.13526 and 0.13556. In this condition volume fraction of dispersoids are close to 4-5 % in all cases. For case [1 1 1], observed ductility and high temperature strength is low as compared to desired ones.

Table 16. Optimized microstructure for different design weightage for condition VIII (4)

Case	**[1 0 0]**	**[10 1 1]**	**[1 1 1]**	**[1 1 10]**
r (nm)	5.51	3.67	5.78	4.33
f_d (%)	4.39	4.44	4.91	4.90
r_f (nm)	232	782	837	632
f_r (%)	14.06	8.51	13.01	10.79
LTS (MPa)	900	1081	900	1022
Ductility	-	0.1	0.059	0.1
HTS (MPa)	-	145	120	150

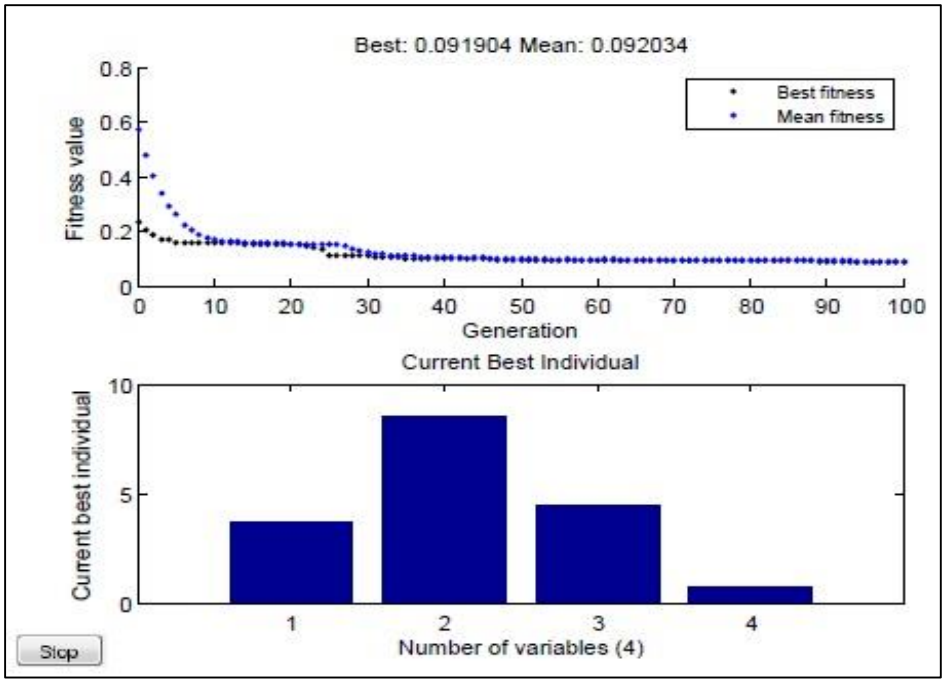

Figure 26. GA plot of case [10 1 1] for condition VIII (4).

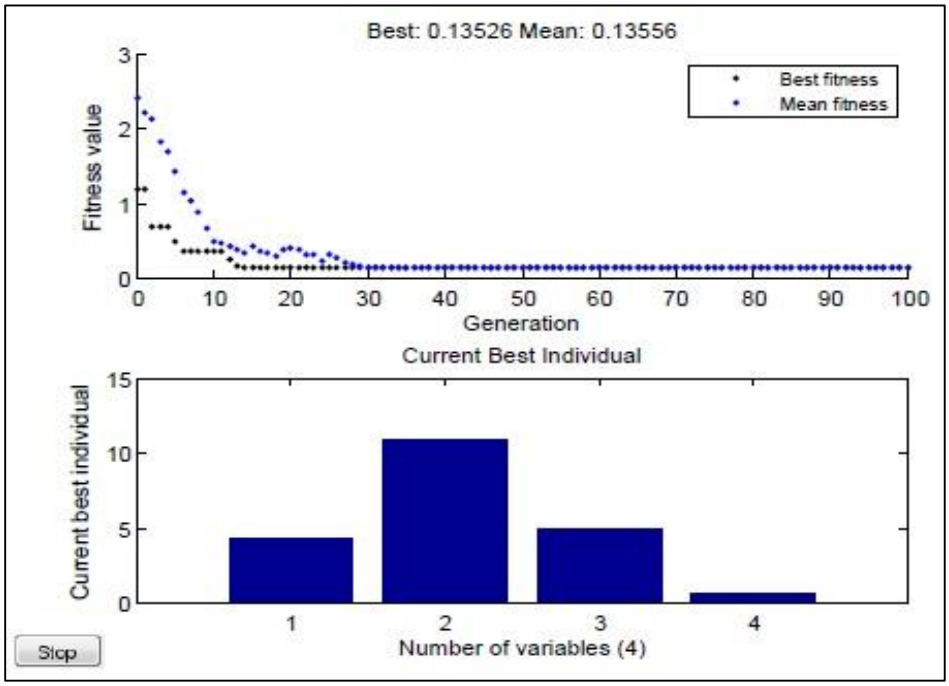

Figure 27. GA plot of case [1 1 10] for condition VIII (4).

Condition VIII (5)

Table 17 shows the results obtained for four different design weightage of condition VIII (5). Here, high temperature strength is low in case of [1 1 1] case like condition VIII (4). The GA plots are shown in Figs. 28 and 29 for the case 2 ([10 1 1]) and case 4 ([1 1 10]). Here, best and

mean fitness values for case 2 are 0.061085 and 0.084838, respectively, and for case 4, 0.15238 and 0.20857.

Table 17. Optimized microstructure for different design weightage for condition VIII (5).

Case	[1 0 0]	[10 1 1]	[1 1 1]	[1 1 10]
r (nm)	4.52	4.05	4.48	4.05
f_d (%)	2.99	5.00	2.94	4.98
r_f (nm)	561	847	764	605
f_r (%)	15.21	6.88	9.40	7.14
LTS (MPa)	900	1059	900	1018
Ductility	-	0.1	0.098	0.1
HTS (MPa)	-	138	85	150

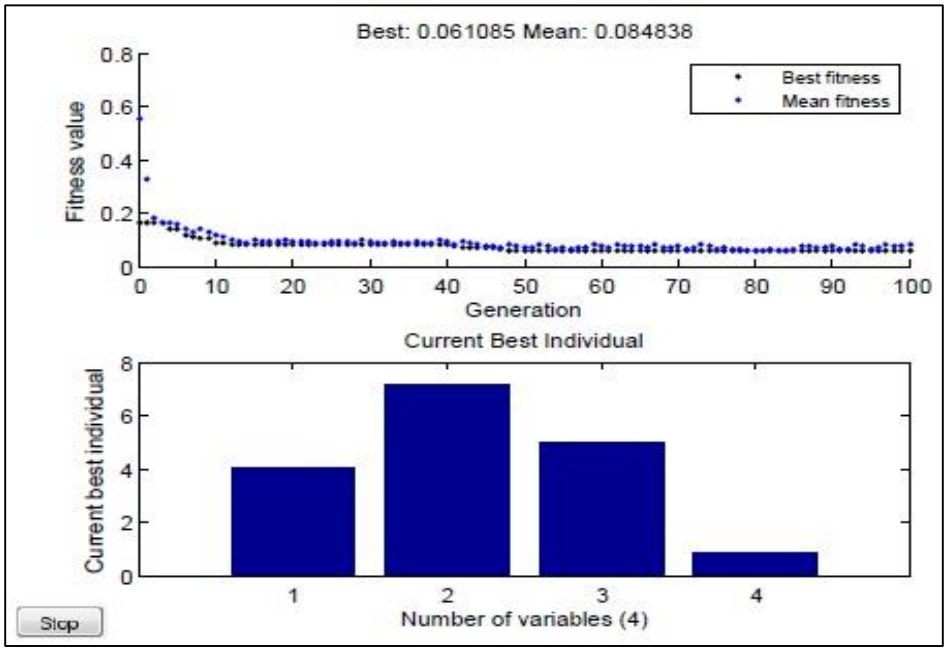

Figure 28. GA plot of case [10 1 1] for condition VIII (5).

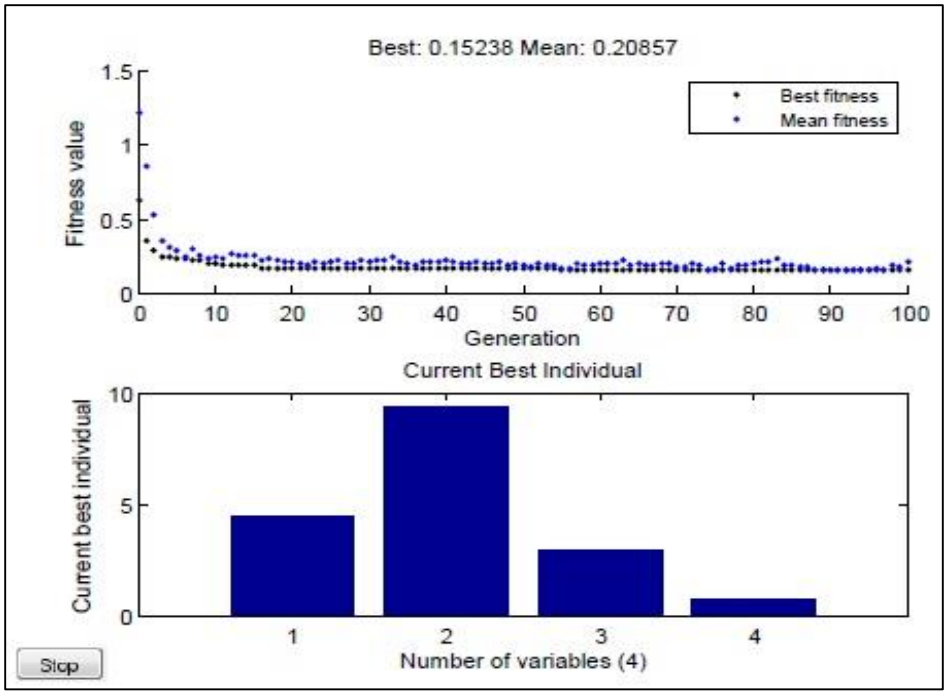

Figure 29. GA plot of case [1 1 10] for condition VIII (5).

Condition VIII (6)

Table 18 shows the results obtained for four different design weightage of condition VIII (6). The GA plots are shown in Figs. 30 and 31 for the case 2 ([10 1 1]) and case 4 ([1 1 10]). Here, best and mean fitness values for case 2 are 0.059051 and 0.059062, respectively, and for case 4, 0.16258 and 0.16264. Observed ductility is 10 % for all the cases, although high temperature strength is low for case [1 1 1] similar to previous conditions.

Table 18. Optimized microstructure for different design weightage for condition VIII (6).

Case	**[1 0 0]**	**[10 1 1]**	**[1 1 1]**	**[1 1 10]**
r (nm)	5.42	4.05	4.90	3.88
f_d (%)	4.30	4.99	3.52	4.28
r_f (nm)	747	948	817	736
f_r (%)	16.27	7.06	8.53	12.37
LTS (MPa)	900	1059	900	1042
Ductility	-	0.1	0.1	0.1
HTS (MPa)	-	150	90	150

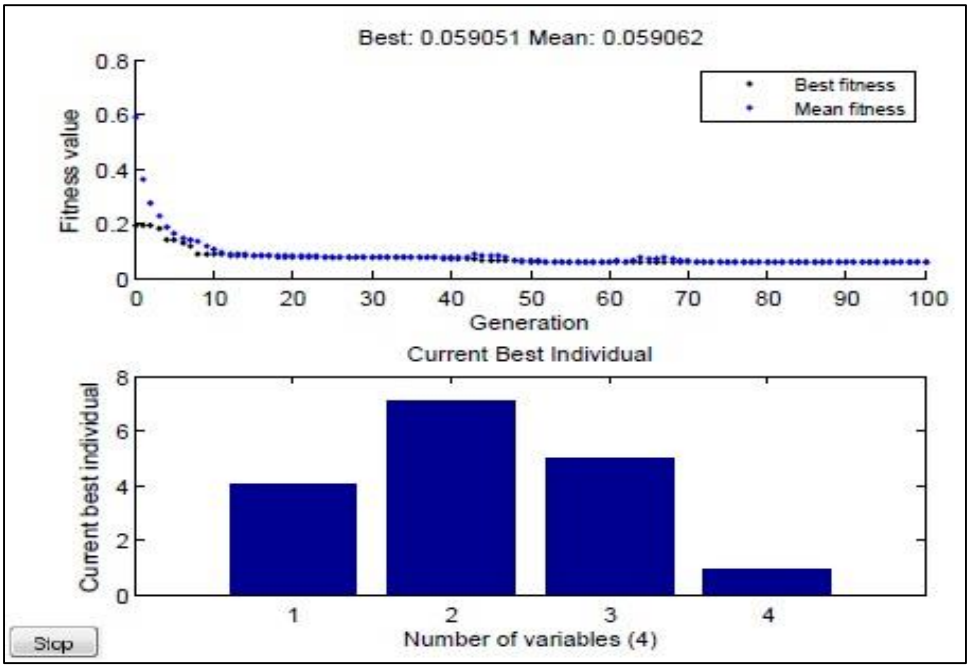

Figure 30. GA plot of case [10 1 1] for condition VIII (6).

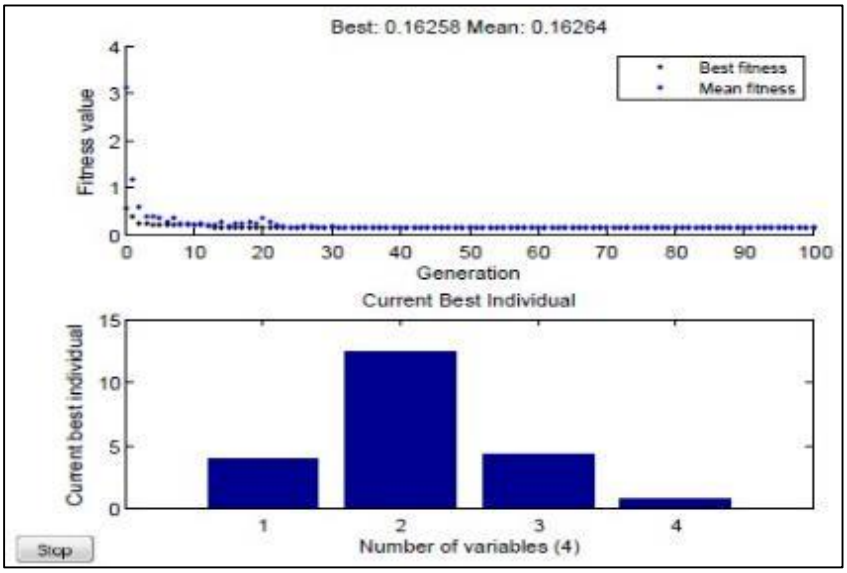

Figure 31. GA plot of case [1 1 10] for condition VIII (6).

Different GA operating conditions were taken to see the optimization results variation with the GA operators. Two conditions were chosen among them for further optimization on the basis of observed property and cost function. For all the above conditions the desired low temperature strength was considered 900 MPa. It was observed that while increasing the weightage on high temperature strength, low temperature strength also increases, which results in more cost function. Considering above situation next optimizations were carried out with 1500 MPa desired low temperature strength.

Condition IX (1)

Table 19 shows the results obtained for four different design weightage of condition IX (1). The GA plots are shown in Figs. 32 and 33 for the case 2 ([10 1 1]) and case 4 ([1 1 10]). Here, best and mean fitness values for case 2 are 0.0237768 and 0.0237827, respectively, and for case 4, 0.029209 and 0.0.0292301. High temperature strength is close to 150 MPa for all cases. The low temperature strength is decreased when weightage factor on high temperature strength is high.

Table 19. Optimized microstructure for different design weightage for condition IX (1).

Case	**[1 0 0]**	**[10 1 1]**	**[1 1 1]**	**[1 1 10]**
r (nm)	2.059	2.306	1.733	2.479
f_d (%)	2.627	2.663	2.025	2.912
r_f (nm)	265	147	556	246
f_r (%)	15.947	9.384	9.973	9.221
LTS (MPa)	1499.99	1393.2	1499.9	1373
Ductility	-	0.1	0.1	0.1
HTS (MPa)	-	150	163.5	150

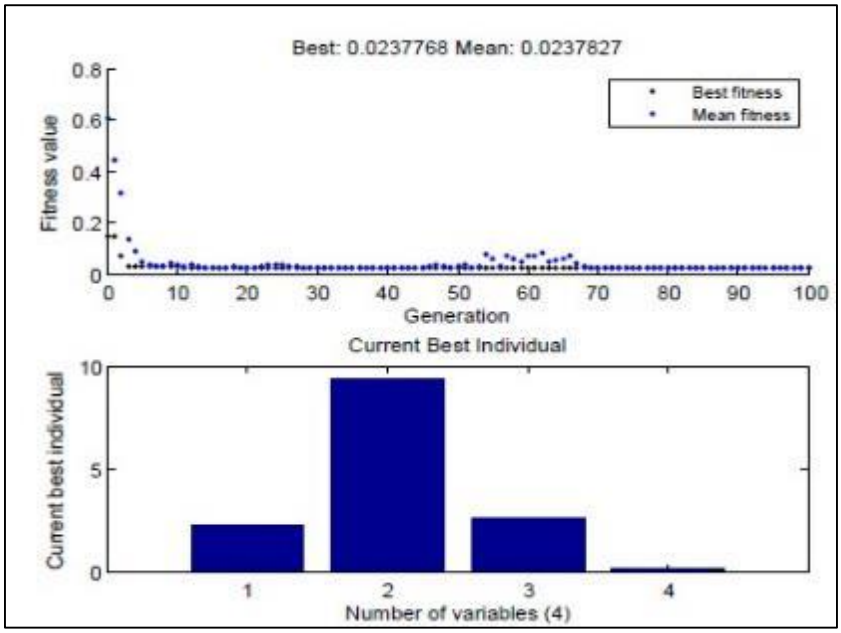

Figure 32. GA plot of case [10 1 1] for condition IX (1).

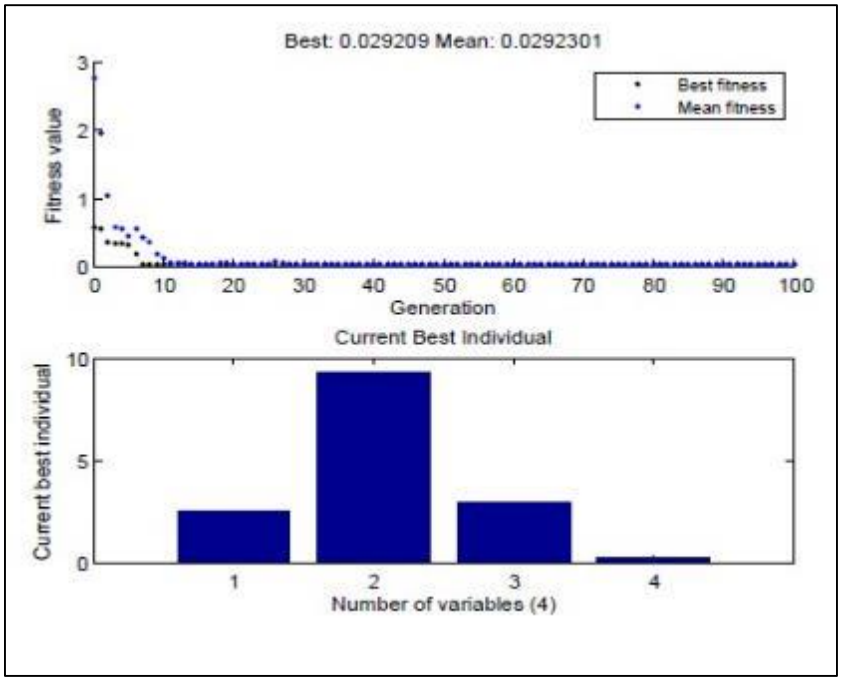

Figure 33. GA plot of case [1 1 10] for condition IX (1).

Condition IX (2)

Table 20 shows the results obtained for four different design weightage of condition IX (2). The GA plots are shown in Figs. 34 and 35 for the case 2 ([10 1 1]) and case 4 ([1 1 10]). Here, best and mean fitness values for case 2 are 0.0221221and 0.032618, respectively, and for case 4, 0.0249994 and 0.0.210684. The results are very similar to above condition.

Table 20. Optimized microstructure for different design weightage for condition IX (2).

Case	**[1 0 0]**	**[10 1 1]**	**[1 1 1]**	**[1 1 10]**
r (nm)	3.012	2.115	1.904	2.133
f_d (%)	4.614	2.372	2.334	2.374
r_f (nm)	657	316	261	122
f_r (%)	12.404	9.674	9.71	9.597
LTS (MPa)	1500	1400.3	1497.9	1395.3
Ductility	-	0.1	0.1	0.1
HTS (MPa)	-	150	164.9	150

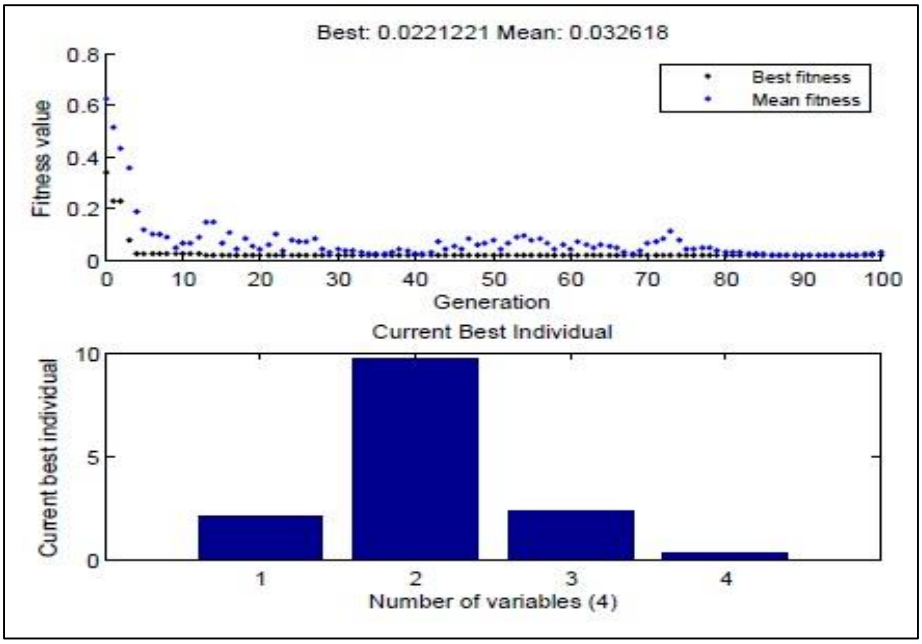

Figure 34. GA plot of case [10 1 1] for condition IX (2).

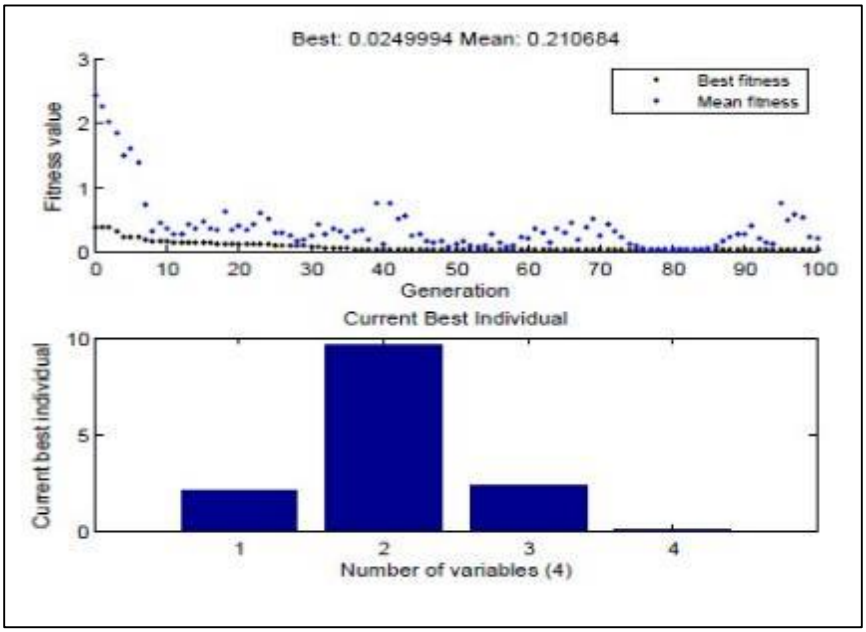

Figure 35. GA plot of case [1 1 10] for condition IX (2).

Condition X (1)

In this condition, two different dispersoids were considered .Table 21 shows the results obtained for four different design weightage of condition X (1). The GA plots are shown in Figs. 36 and 37 for the case 2 ([10 1 1]) and case 4 ([1 1 10]). Here, best and mean fitness values for case 2 are 0.057057and 0.2049, respectively, and for case 4, 0.081032 and 0.0.21854. Here, observed low temperature strength is close to desired one for all cases.

Table 21. Optimized microstructure for different design weightage for condition X (1).

Case	**[1 0 0]**	**[10 1 1]**	**[1 1 1]**	**[1 1 10]**
r1 (nm)	20.36	40.58	16.65	17.83
r2 (nm)	1.67	1.11	1.28	1.99
f_d 1(%)	1.39	3.41	1.40	3.12
f_d 2(%)	2.80	1.29	1.31	2.27
r_f (nm)	857	568	515	416
f_r (%)	14.09	7.33	9.30	7.82
LTS (MPa)	1500	1519	1403	1456
Ductility		0.1	0.1	0.1
HTS (MPa)		137	150	150

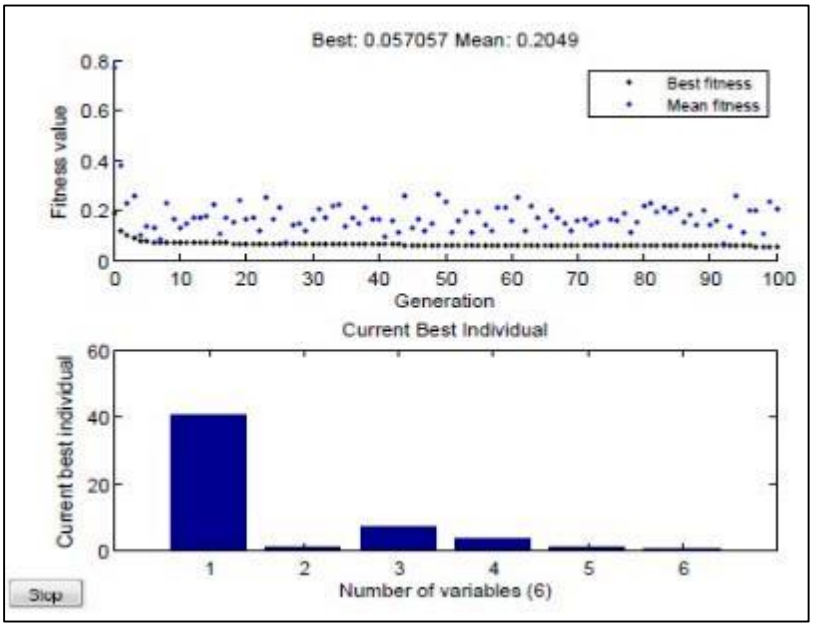

Figure 36. GA plot of case [10 1 1] for condition X (1).

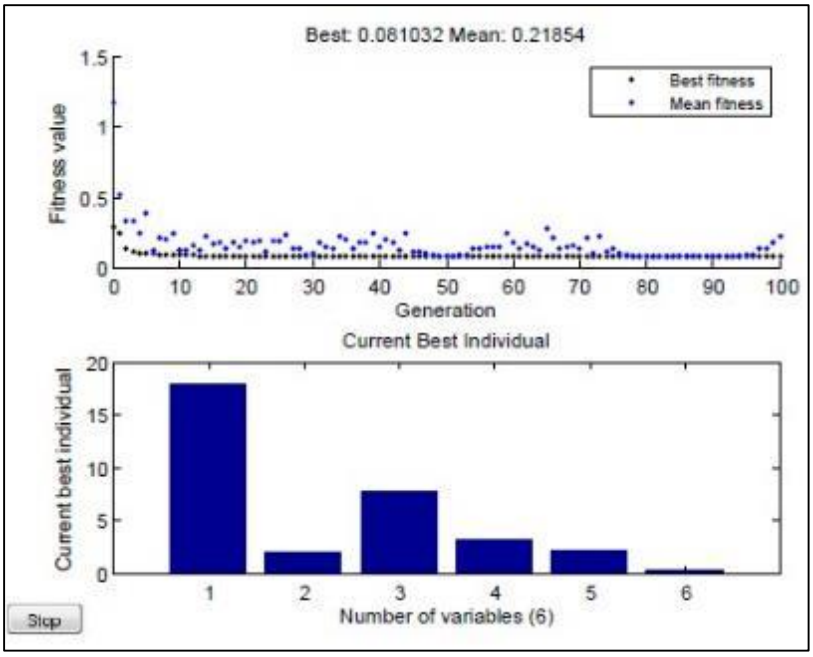

Figure 37. GA plot of case [1 1 10] for condition X (1).

Condition X (2)

Table 22 shows the results obtained for four different design weightage of condition X (2). The GA plots are shown in Figs. 38 and 39 for the case 2 ([10 1 1]) and case 4 ([1 1 10]). Here, best and mean fitness values for case 2 are 0.00543and 0.15197, respectively, and for case 4, 0.031663 and 0.0.13989. The observed high temperature strength is close to desired one, although observed low temperature strength is lower than the desired for [1 1 10] case.

Table 22. Optimized microstructure for different design weightage for condition X (2).

Case	**[1 0 0]**	**[10 1 1]**	**[1 1 1]**	**[1 1 10]**
r1 (nm)	11.90	52.00	29.70	17.91
r2 (nm)	1.62	1.19	1.51	1.54
f_d 1(%)	4.95	4.99	1.64	2.76
f_d 2(%)	2.56	1.41	1.82	1.69
r_f (nm)	716	413	815	510
f_r (%)	5.43	5.64	8.58	7.59
LTS (MPa)	1500	1500	1400	1358
Ductility		0.1	0.1	0.1
HTS (MPa)		142	150	150

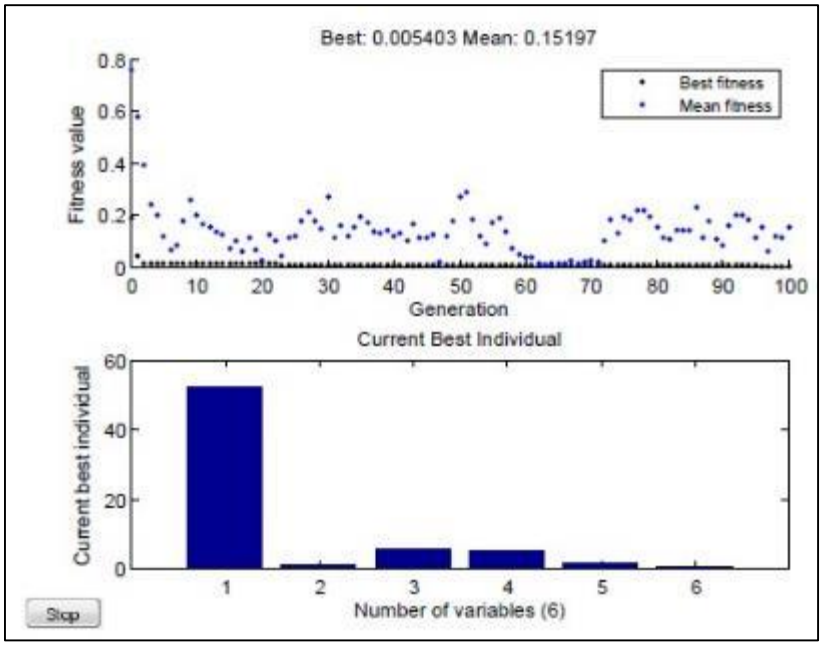

Figure 38. GA plot of case [10 1 1] for condition X (2).

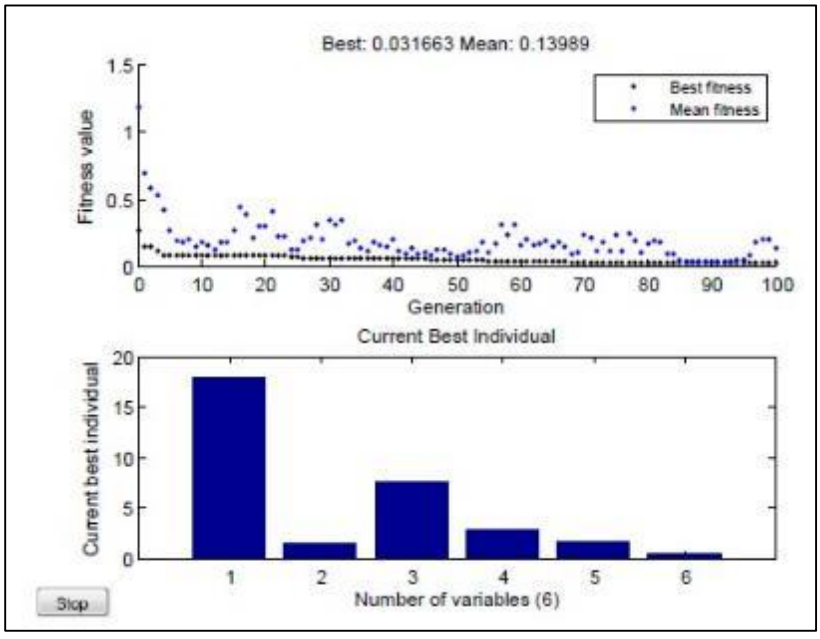

Figure 39. GA plot of case [1 1 10] for condition X (2).

Dislocation motion simulation

The dislocation motion visualization was simulated for Al-alloys to verify the simulation approach [38]. After verification of simulation approach, it was applied for Ni-ODS system for uniform particle distribution and random particle distribution. Population of obstacles was distributed uniformly in the glide plane. CRSS was calculated from the dislocation-particle interaction. Constant line tension approach was used for interactions. Dislocation was initially at bottom of the glide plane and it started approaching particles and an initial stable configuration

obtained depending on initial applied stress. Periodic boundary conditions were applied at the left and right boundary of the glide plane. For each set of particles, critical angle was defined using modified Orwan equation [31] and Friedel model [40]. The bow-out radius was estimated using [46- 48]

$$R = \frac{F}{\sigma b} \quad (22)$$

where σ is the applied shear stress, b is Burger vector and F is the line tension which can be expressed as [47, 48]

$$F = \frac{Gb^2}{4\pi} ln \frac{\lambda}{b} \quad (23)$$

where λ is the inter-particle spacing.

When applied stress was increased the dislocation line started bow-out and terminate on the following conditions:

a) The dislocations encountered a new obstacle of the array and retained new configuration.
b) When angle is less than critical angle at any point, then dislocation left that point and approached new points using circle rolling technique.
c) The procedure (a) and (b) was repeated until it touched the upper edge of the glide plane.

Conditions considered for the particle –dislocation simulation:
Particle size, r (nm) = 4; volume fraction, f = 4 %; G= 75 GPa; b= 0.249 nm and φ_{cr}= 118^0.
The obtained CRSS value is 373 MPa for uniform particle distribution and 415 MPa for random particle distribution. Observed CRSS in random distribution of particles is higher than the CRSS observed in uniformly distributed particles.

Mechanical milling

The X-ray diffraction pattern (XRD) of the as-received Ni-20Cr powder is shown in Figure 40. It revealed that the Ni-20Cr powder has the FCC-specific peaks. There was no separate Ni or Cr peaks present, implying that the powder was in the form of a solid solution alloy. Also, SEM experiments on the Ni-20Cr powder revealed (as shown in Figure 41) that the powder particle shape was more or less spherical and the mean powder size was measured to be ~20 μm. However, a few powder particles were also found to be in agglomerated state and with spheroidal shape. The EDS experiments done in conjunction with SEM showed that it was Ni-20Cr powder with 1.5-1.8 wt.% Si and other minor impurities.

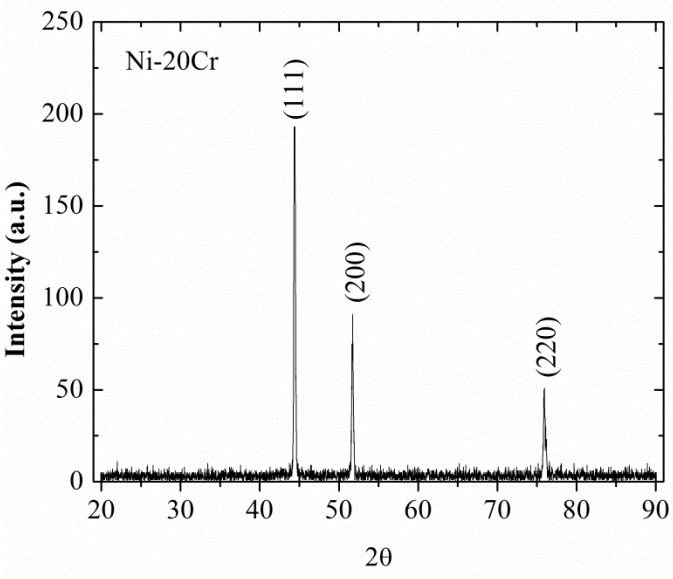

Figure 40. The XRD pattern from the as-received Ni-20Cr powder (note that diffraction angle, 2θ, is in degree).

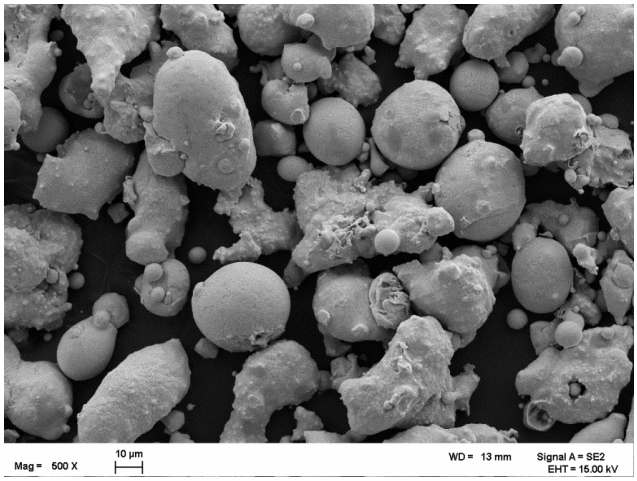

Figure 41. A SEM micrograph of the as-received Ni-20Cr powder.

Figure 42 shows the XRD pattern of the yttria powder. It revealed that it was a high purity powder with no other significant phase present. A SEM image of the yttria powder as shown in Fig. 43a revealed a mean powder particle size less than 100 nm. However, yttria powder particles were better resolved using a STEM as shown in Figure 43b. The powder particle size was measured to be 30-40 nm.

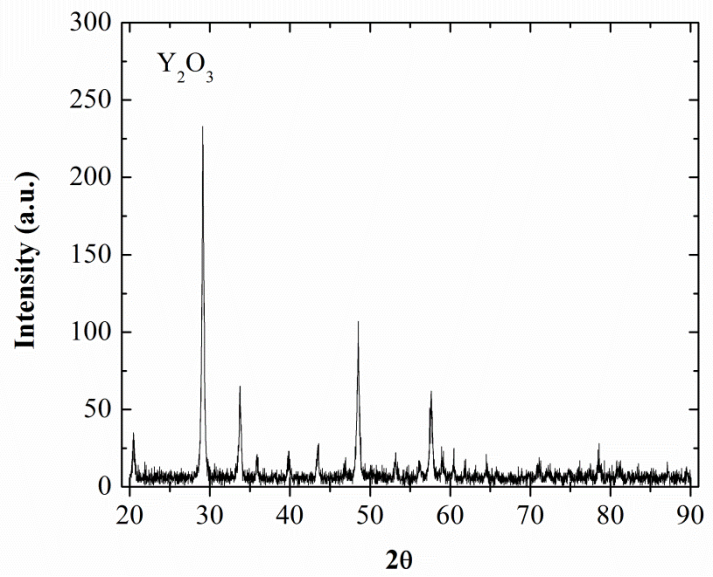

Figure 42. The XRD pattern from the as-received nano-yttria powder (note that the diffraction angle 2θ is in degree).

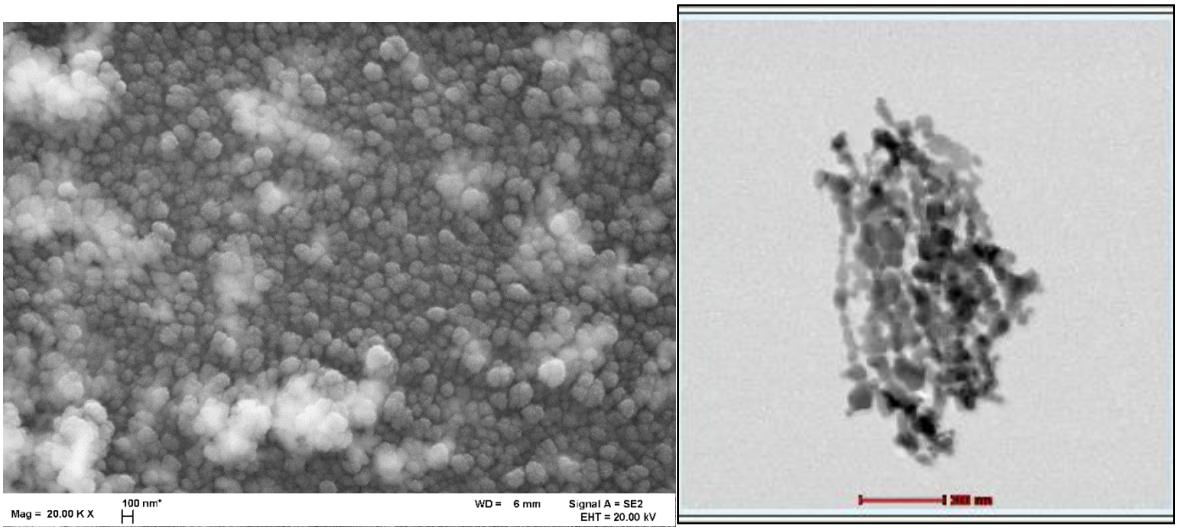

(a) (b)

Figure 43. a) A SEM micrograph of the nano-yttria powder; b) A STEM HAADF micrograph from the as-received Y_2O_3 powder.

An XRD pattern of the as-received α-Al_2O_3 powder is shown in Fig. 44. It revealed a highly pure α-Al_2O_3 powder. This was also confirmed by EDS experiments. An SEM image of the powder in Figure 45 shows that the powder had an average particle size of 500 nm.

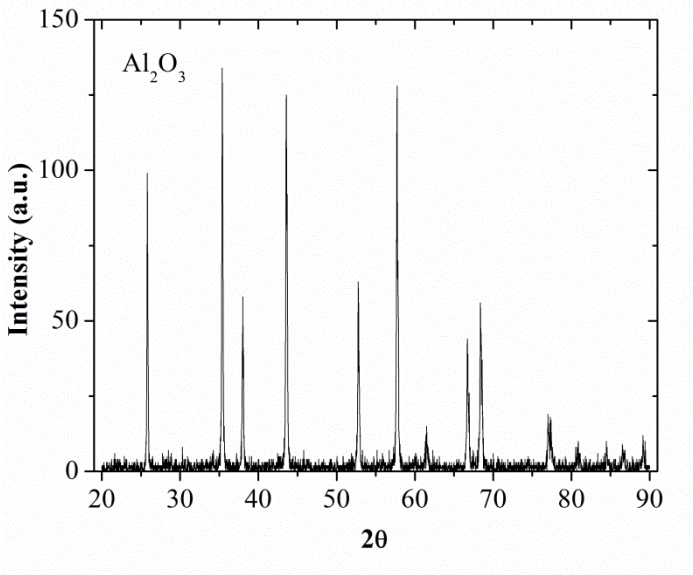

Figure 44. The XRD pattern of the as-received α-Al_2O_3 powder.

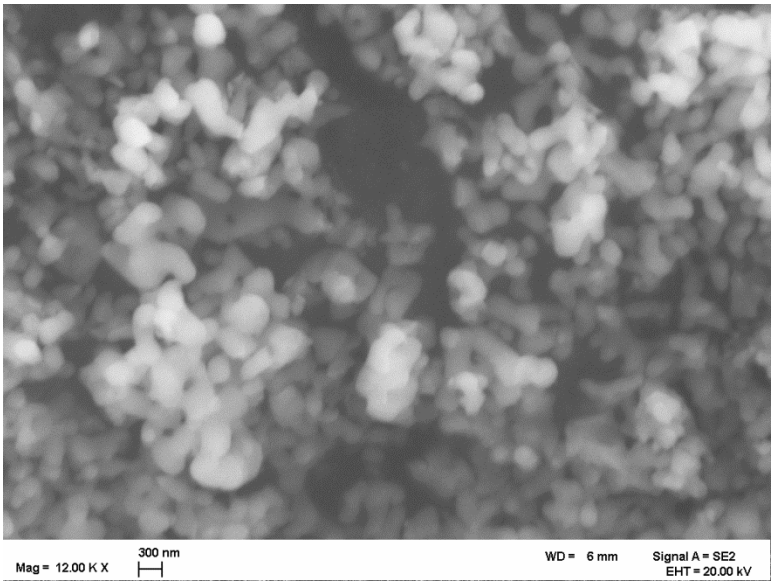

Figure 45. A SEM micrograph of the as-received α-Al_2O_3 powder.

a) Characteristics of the blended (unmilled) powder

The XRD pattern of the blended powder shown in Figure 46 reveals the Ni-20Cr peaks along with short peaks of yttria. Figure 47 shows the powder morphology after blending. As expected, Ni-20Cr powder morphology stayed more or less the same while the nano-yttria powder covered the larger powder particles of Ni-20Cr. This was confirmed by EDS/SEM in Figure 48.

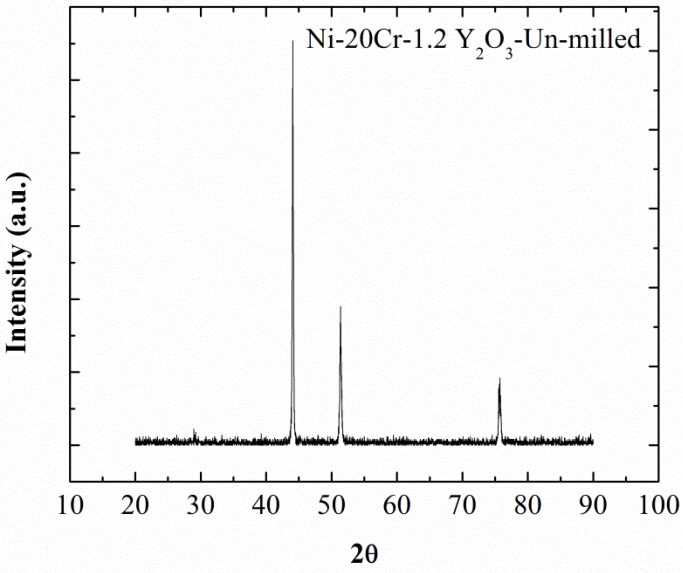

Figure 46. The XRD pattern of the powder mixture Ni-20Cr-1.2Y_2O_3 (before ball milling). Note that the diffraction angle (Y-axis) is in the unit of degree.

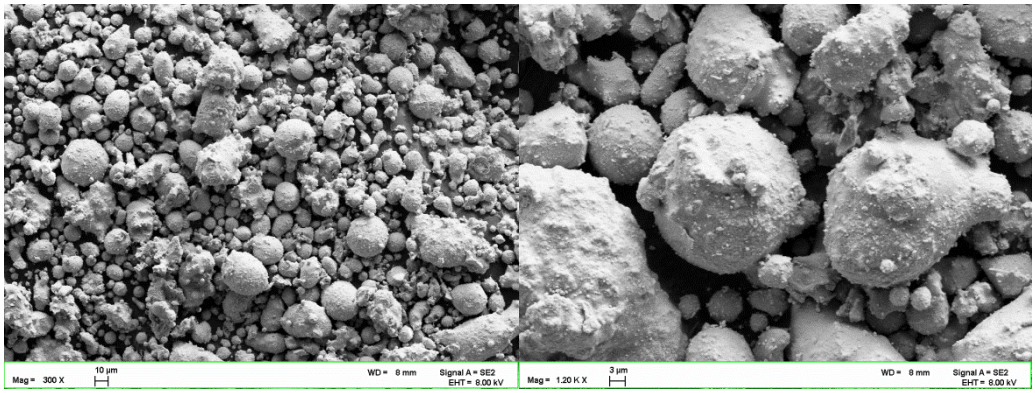

Figure 47. SEM images of the unmilled powder showing the powder morphology.

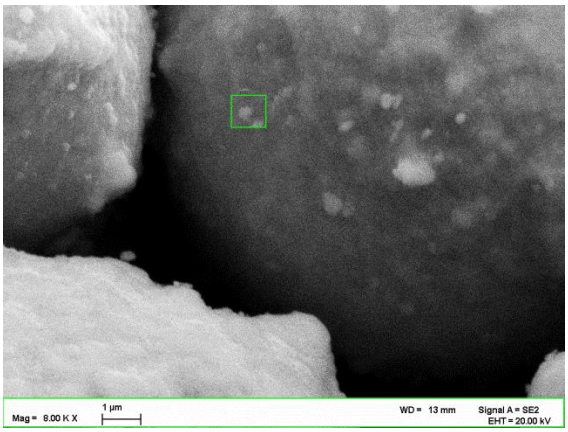

Element Line	Net Counts	Net Error	Element Wt.%	Wt.% Error	Atom %	Atom % Error
Si K	7767	+/-234	3.786	+/-0.114	7.733	+/-0.233
Cr K	29667	+/-300	18.976	+/-0.192	20.939	+/-0.212
Fe K	1725	+/-193	1.404	+/-0.157	1.443	+/-0.161
Ni K	52556	+/-409	63.118	+/-0.491	61.680	+/-0.480
Y L	18425	+/-402	12.716	+/-0.277	8.206	+/-0.179
			---		---	
Total			100.000		100.000	

Figure 48. A high-magnification image of the blended powder showing the EDS results of a powder particle. Note the evidence of yttrium in the selected region of EDS analysis.

b) Characteristics of the ball milled powder

The powder mixture of the Ni-20Cr-1.2Y_2O_3 was milled for 4 h using BPR of 10:1 and stainless steel balls of 8 mm in diameter. After milling, the balls were coated with a heavy layer of the Ni-Cr and only little amount of powder was obtained, i.e., powder yield was very low. Most of the powder was cold welded to the balls! The Ni oxide is not very stable, and during the ball milling the oxide layer gets fractured and Ni-Ni particles contact led to the cold welding and also on the milling balls. The mass of one steel ball before milling was 2.086 g and after milling for 4 h was 2.256 g. This extra mass was due to cold welded Ni powder. The 10 g mass of powder before milling was found to be only 1.006 g after 4 h of milling. Another issue with the Ni powder was that it is so ductile that most of them did not fracture significantly and instead got cold welded. In order to minimize the cold welding effect, chromium steel vial and hardened chromium steel balls were used. Ball milling was carried out in the SPEX mixer/mill for 1, 2 and 4 h, and the XRD was used to characterize them. The XRD patterns in Figure 49 show that 4 h was not long enough to make the yttria peaks disappear. But in this work, yttria particles were not required to dissolve; rather nano-yttria particles needed to be distributed uniformly across the metallic powder particles. Significant peak broadening and peak shift to higher angles were observed just after 1 h of milling. SEM images were used to measure the powder size. However, only after 1 h of milling the mean particle size increased to 280 µm. Significant agglomeration still happened in the milled powder. The agglomeration effect decreases efficiency of the mechanical alloying process. The finer powder particles are desired as they increase the sintering efficiency and final density. Using a process control agent (PCA) can decrease the agglomeration effect. That is why 1 wt.% of ethanol, 1wt.% polyethylene glycol (PEG) and 1 wt.% stearic acid as PCA were added separately to the powder mixture before starting ball milling for 4 h, and the corresponding SEM images are shown in Figure 50(a)-(c),

respectively. The mean powder particle size of the milled powder decreased significantly after using PCA resulting from less agglomeration. The efficiency of stearic acid was found to be better than that of ethanol and PEG as illustrated in Figure 50.

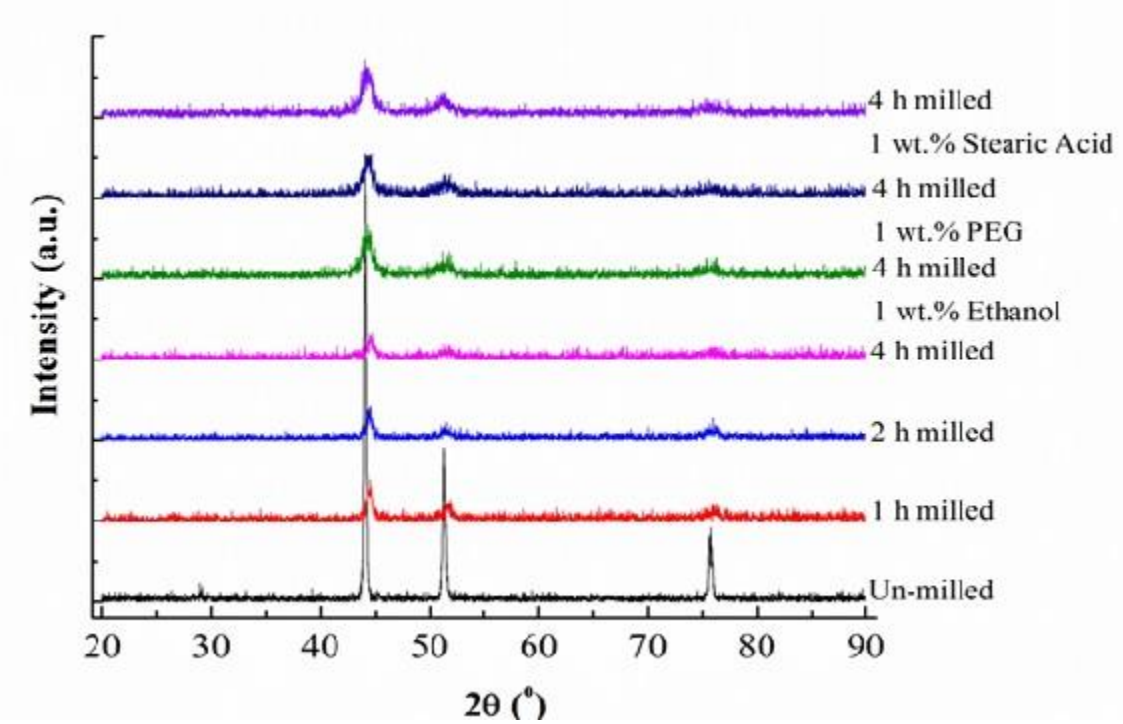

Figure 49. XRD patterns of the Ni-20Cr-1.2Y_2O_3 powder milled under different conditions.

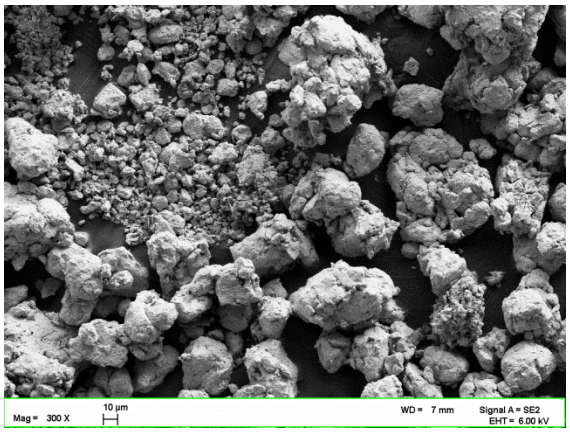

(a)

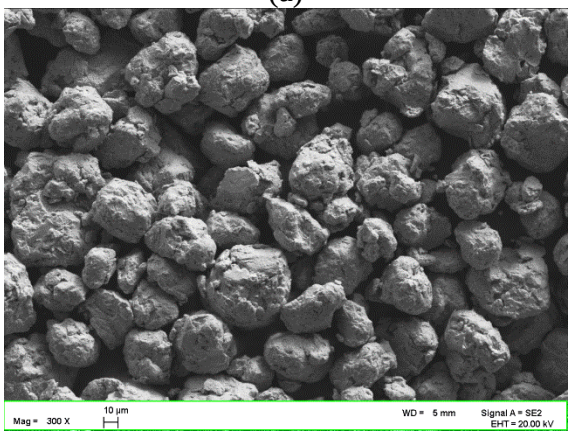

(b)

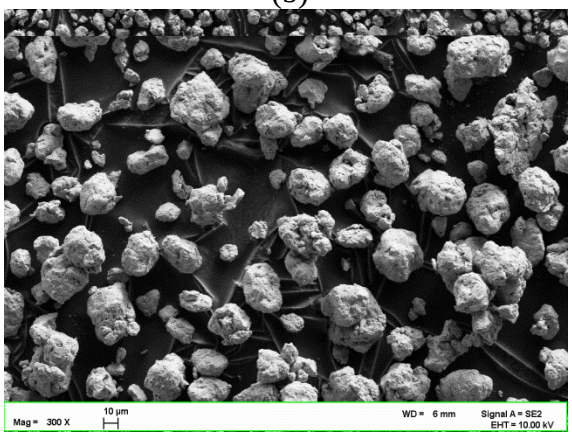

(c)

Figure 50. SEM images of the Ni-20Cr-1.2Y_2O_3 powder milled for 4 h with (a) ethanol, (b) PEG and (c) stearic acid.

It was also found that about 1 wt.% addition of stearic acid yielded optimum result. The XRD results were used to calculate the crystallite size, lattice strain and lattice constant. The Nelson-Riley extrapolation method [44] was used to determine the lattice constant of the ball milled powder, whereas the crystallite size and lattice strain were evaluated using the Williamson-Hall analysis [45]. The ball-milled powder size was determined by SEM. Table 23 lists all the microstructural parameters of the ball milled powder. The relevant parameters of the blended

powder mix (denoted by '0' milling time) are also included in the Table for comparison. The Ni-20Cr powder (milled for 2 h) exhibited a crystallite size of 90 nm.

Table 23. Microstructural parameters of Ni-20Cr-1.2Y_2O_3 alloy as determined by XRD and SEM.

Milling Time (h)	**Crystallite Size (nm)**	**Lattice Strain (%)**	**Lattice Constant (nm)**	**Mean Powder Size (μm)**
0	44±12	0.03±0.001	0.3530±0.0002	23.6±1.1
1	17±9	0.03±0.001	0.3532±0.0003	39.2±2.2
2	14±7	0.03±0.001	0.3536±0.0003	33.6±1.5
4	4±2	0.15±0.003	0.3560±0.0004	39.4±3.1

On the issue of mixing α-Al_2O_3 powder in Ni-20Cr-1.2Y_2O_3 powder, SEM and TEM studies have shown that just blending Al_2O_3 powder to the 2 h milled Ni-20Cr-1.2Y_2O_3 powder did not lead to a homogeneous distribution of Al_2O_3 particles in the sintered alloy. Rather these particles were located on the prior powder particle boundaries. A SEM micrograph of Ni-20Cr-1.2Y_2O_3 milled for 2 h, blended with Al_2O_3 particles and sintered at 1100 ^oC for 30 min is shown in Fig. 51a. The regions showing darker contrast have decorated the boundaries and were found to be enriched with Al_2O_3 particles. The EDS analysis was done on these regions and the spectrum is shown in Fig. 51b. The TEM micrograph of this sample is shown in Fig. 52. The particles larger than 100 nm were distributed on the boundaries and larger Al_2O_3 particles likely disappeared from TEM thin foil during electrojet polishing. In addition to losing the Al_2O_3 particles in jet polishing, these non-conductive particles made electrojet polishing a challenging technique for TEM sample preparation and therefore, focused ion beam (FIB) was used for further TEM sample preparation. However, as shown in Figs. 51 and 52, just blending Al_2O_3 particles did not provide a homogeneous distribution, and ball milling of the Al_2O_3 powder with Ni-20Cr-1.2Y_2O_3 powder was thus followed.

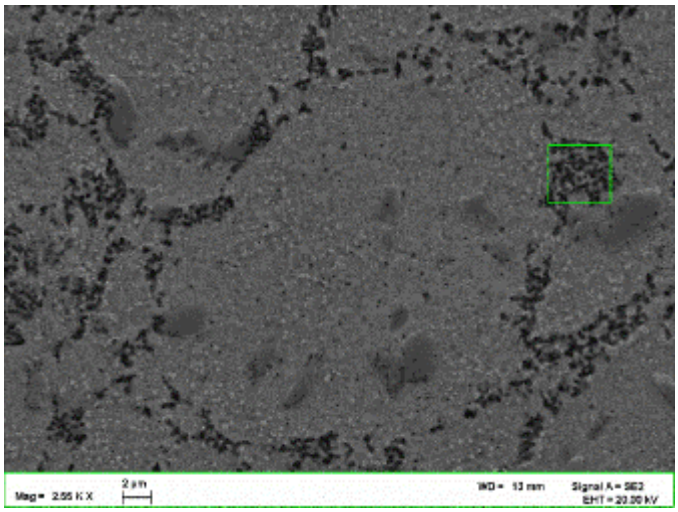

(a)

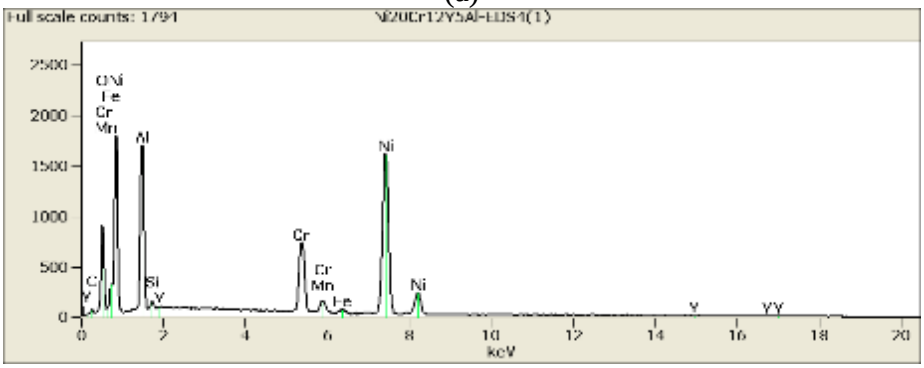

(b)

Figure 51**.** (a) A SEM micrograph of Ni-20Cr-1.2Y_2O_3-5Al_2O_3 alloy after sintering at 1100 ^oC for 30 min, and (b) the corresponding EDS spectrum taken from the square shown in Fig. 51a (the Al_2O_3 particles were blended with milled Ni-20Cr-1.2Y_2O_3 powders without further milling).

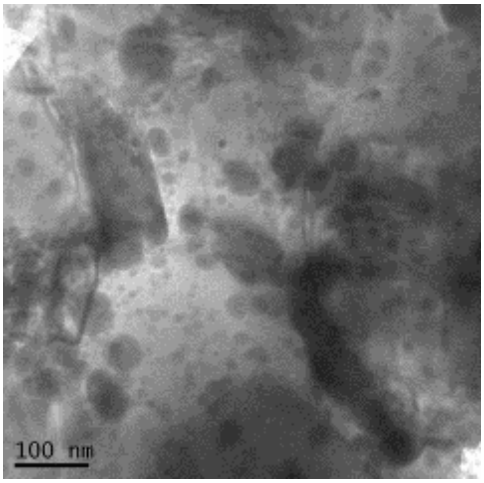

Figure 52**.** A TEM bright field micrograph of Ni-20Cr-1.2Y_2O_3-5Al_2O_3 after sintering at 1100 ^oC for 30 min (the Al_2O_3 particles were blended with the milled Ni-20Cr-1.2Y_2O_3 powder without further milling).

In order to study the fate of alumina powder under ball milling, the alumina powder was ball milled in a Spex mixer/mill with chromium-hardened steel balls, 5 mm in diameter and ball to powder ratio of 10:1. Then the milled alumina powders were coated with carbon and studied in a SEM with a 5 kV accelerating voltage at two different magnifications (500X and 12kX). The SEM micrographs at the lower magnification are shown in Figs. 53a-d while the SEM micrographs at 12kX are displayed in Figs. 54a-e. After 30 min of milling, the average alumina particle size was reduced from 400 nm in the as-received powder to 100 nm, but at longer milling time the agglomeration was the main problem.

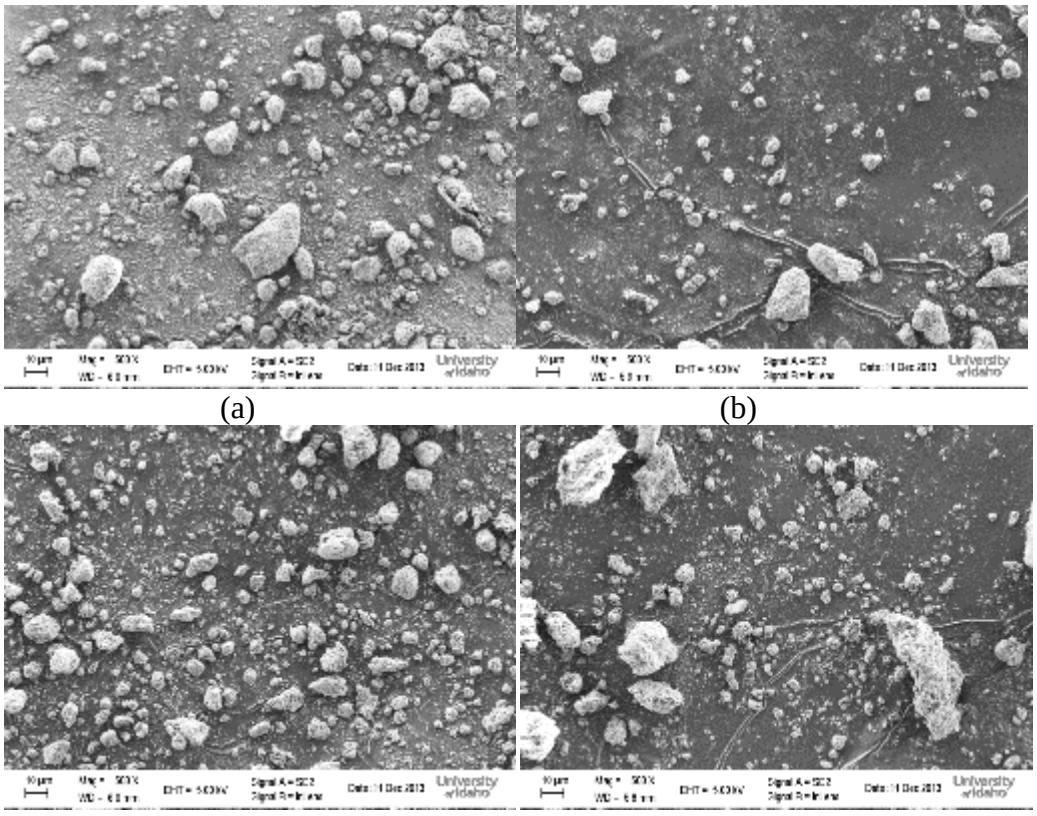

(a) (b)

(c) (d)

Figure 53**.** SEM micrographs of the Al_2O_3 powder milled for (a) 20 min, (b) 30 min, (c) 60 min and (d) 120 min at a magnification of 500 X.

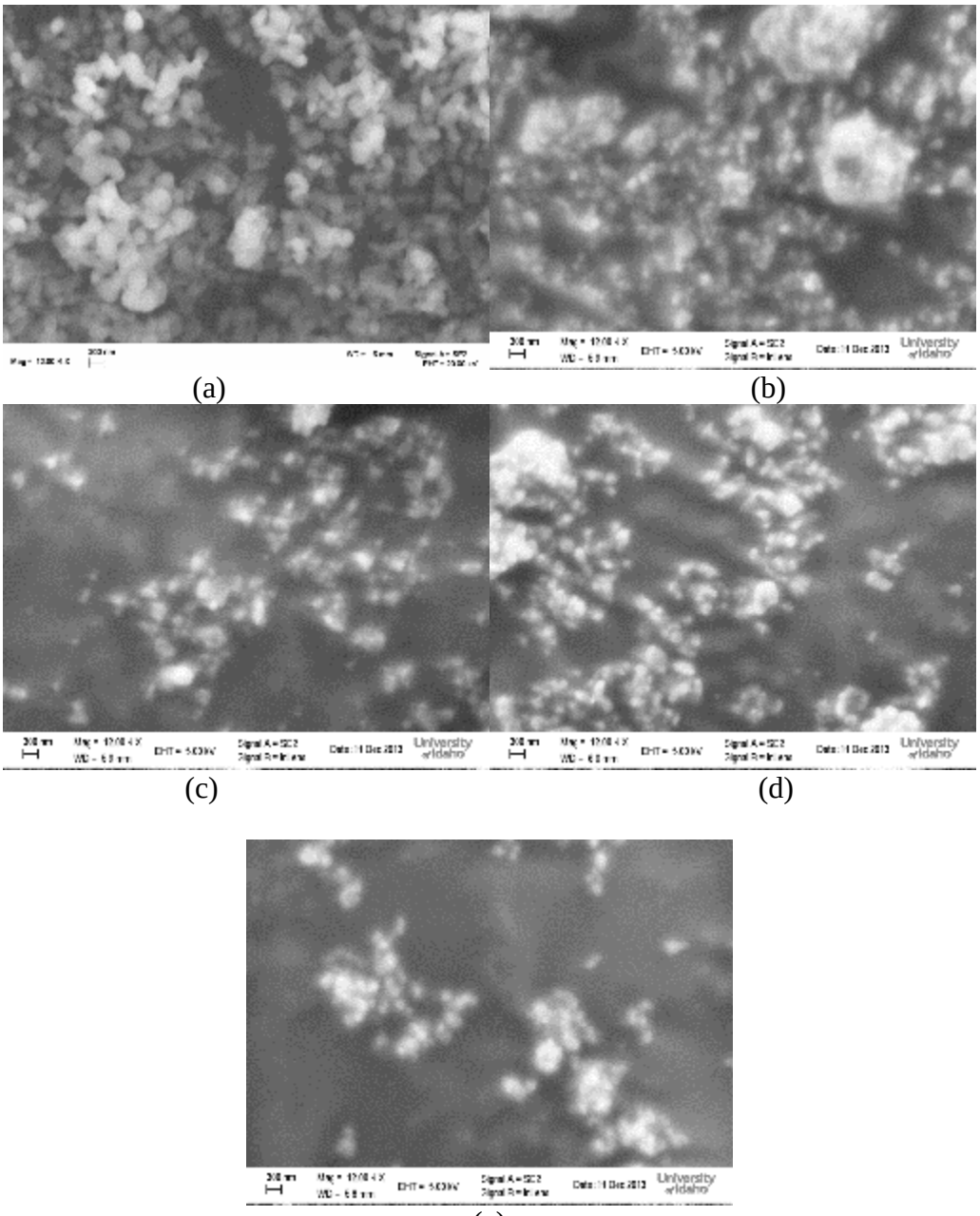

Figure 54. SEM micrographs from the Al_2O_3 particles milled for (a) 0 min (i.e. no milling), (b) 20 min, (c) 30 min, (d) 60 min, and (e) 120 min at 12 kX.

The following procedure was adopted to develop Ni-20Cr-1.2Y_2O_3-5Al_2O_3 powder. The powder with the nominal composition of Ni-20Cr-1.2Y_2O_3 was milled for 2 h using ball to powder ratio of 10:1 and ball diameter of 5 mm. Then 5 wt% Al_2O_3 powder was added to the milled powder inside a glove box and ball milling was continued for 30 min. A SEM micrograph from the as-milled powder of Ni-20Cr-1.2Y_2O_3-5Al_2O_3 is shown in Fig. 55.

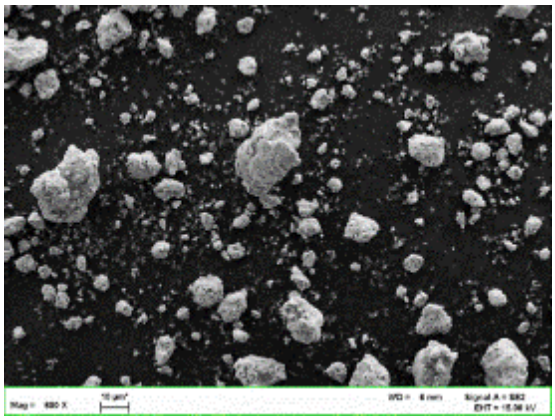

Figure 55. A SEM micrograph of the as-milled Ni-20Cr-1.2Y_2O_3-5Al_2O_3 powder.

Density and mechanical characterization of SPSed samples

The density measurements conducted for each SPSed sample at least 5 times. Then measured absolute density values were converted to relative density values using theoretical density of the materials (Ni-20Cr – 8.28 g/cm^3; Ni-20Cr-1.2Y_2O_3 – 8.21 g/cm^3; Ni-20Cr-5Al_2O_3 – 7.82 g/cm^3; Ni-20Cr-1.2Y_2O_3-5Al_2O_3 – 7.76 g/cm^3). Table 24 summarizes the density and microhardness results of Ni-20Cr-1.2Y_2O_3 alloys SPSed for 5 min at four different temperatures (600, 900, 1000 and 1100 ^oC). With increasing SPS temperature the density increased up to 1000 ^oC, but at 1100 ^oC it did not increase any further as the sample reached near full density. The microhardness of the samples increased with increasing SPS temperature (and density); however at 1100 ^oC, the density decreased presumably due to microstructural coarsening. Table 25 lists the density and microhardness values of the samples with different compositions. The data demonstrates that Y_2O_3 and then Al_2O_3 play a significant role in enhancing the hardness. Table 26 summarizes the density and hardness values of Ni-20Cr-1.2Y_2O_3 alloy SPSed by using powder milled for different times (2 and 4 h). The milling time increases the hardness of the SPSed samples. However, this is possibly due to a lower crystallite size at the initial 4 h milled powder compared to 2 h milled powder. However, 2 h milling time was favored as the contamination pick-up from the steel balls and vial would increase with increasing milling time.

Table 24. Effect of different SPS temperatures (powder milled for 2 hr, BPR of 10 and ball diameter of 5 mm).

Material	**SPS parameters**	**Density (g/cm^3)**	**Relative density (%)**	**Hardness (HV)**
Ni-20Cr-1.2Y_2O_3	600 ^oC/5 min	5.92	72.19±0.24	130.8±31.6
Ni-20Cr-1.2Y_2O_3	900 ^oC/5 min	7.71	93.93±0.03	395.1±11.4
Ni-20Cr-1.2Y_2O_3	1000 ^oC/5 min	8.15	99.26±0.30	555.9±4.6
Ni-20Cr-1.2Y_2O_3	1100 ^oC/5min	8.16	99.48±0.05	469.6±7.8

Table 25. Effect of different powder compositions (powder milled for 2 hr, BPR of 10 and ball diameter of 5 mm; in compositions containing Al_2O_3, they were mixed subsequent to 2 hr milling).

Ni-20Cr	1100 ºC/30 min	8.19	98.95±0.03	307.6±2.7
Ni-20Cr-1.2Y_2O_3	1100 ºC/30 min	8.17	99.55±0.04	471.6±7.5
Ni-20Cr-5Al_2O_3	1100 ºC/30 min	7.79	99.61±0.02	399.1±17.9
Ni-20Cr-1.2Y_2O_3-5Al_2O_3	1100 ºC/30 min	7.68	98.97±1.54	507.8±21.7

Table 26. Effect of different milling times (BPR of 10 and ball diameter of 5 mm).

Ni-20Cr-1.2Y_2O_3 (0 hr milled)	1100 ºC/30 min	8.23	100.26±0.06	201.6±6.2
Ni-20Cr-1.2Y_2O_3 (2 hr milled)	1100 ºC/30 min	8.17	99.55±0.04	471.6±7.5
Ni-20Cr-1.2Y_2O_3 (4 hr milled)	1100 ºC/30 min	8.23	100.24±0.02	526.7±21.4

Compression tests on the three materials (Ni-20Cr, Ni-20Cr-1.2Y_2O_3 and Ni-20Cr-1.2Y_2O_3-5Al_2O_3) were carried out at room temperature and 800 ºC and a strain rate of 10^{-3} s^{-1}. Here the corresponding yield stresses are listed in Table 27.

Table 27. The compression yield stress values of Ni-20Cr, Ni20-Cr-1.2Y_2O_3 and Ni-20Cr-1.2Y_2O_3-5Al_2O_3 alloys sintered at 1100 °C for 30 min.

Alloy	Compression Yield Stress at 25 °C (MPa)	Compression Yield Stress at 800 °C (MPa)
H (Ni-20Cr)	790	125
B (Ni-20Cr-1.2Y_2O_3)	1286	225
I (Ni20-Cr-1.2Y_2O_3-5Al_2O_3)	1470	250

Hot compression tests were done at 800 ºC using the strain rate of 10^{-3} s^{-1} on three developed alloys (Ni-20Cr, Ni-20Cr-1.2Y_2O_3 and Ni-20Cr-1.2Y_2O_3-5Al_2O_3). The true stress – true plastic strain plots for these alloys are shown in Fig. 56a. As expected, the flow stress of Ni-20Cr alloy improved by adding 1.2 wt% Y_2O_3, and it improved further by adding 5 wt% Al_2O_3. Flow curves for the Ni-20Cr-1.2Y_2O_3 alloy obtained from compression tests performed at 800 ºC and different strain rates are shown in Figure 56b. The flow curves show stress show strain-rate sensitive flow behavior as would be expected at high temperature.

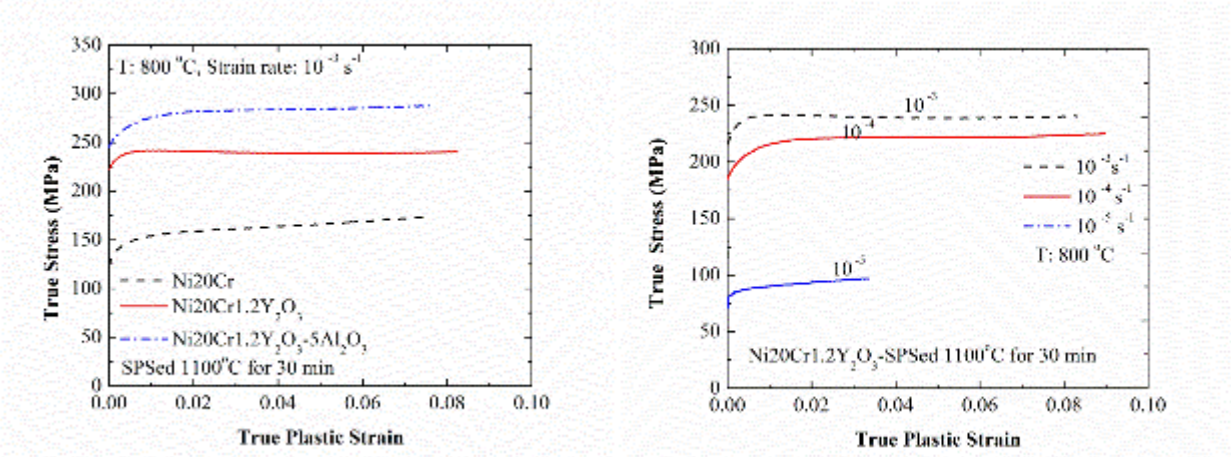

Figure 56. The true stress-strain plots for Ni-20Cr, Ni-20Cr-1.2Y_2O_3 and Ni-20Cr-1.2Y_2O_3-5Al_2O_3 sintered at 1100 °C for 30 min.

Microstructural characterization

Figure 57 shows a TEM image of the ball milled Ni-20Cr-1.2Y_2O_3 powder showing nano particles of Y_2O_3 with an average diameter of about 10 nm in the nanocrystalline matrix of Ni-Cr solid solution. With increasing milling time, the crystallite size decreased. Milling for 4 h caused an increase in the lattice constant as an indication that Y_2O_3 dissolved in the matrix to a significant extent. However, because the purpose of this study was to distribute the yttria particles uniformly and not to dissolve them fully in the matrix, 2 h ball milled powder was used for subsequent SPS experiments.

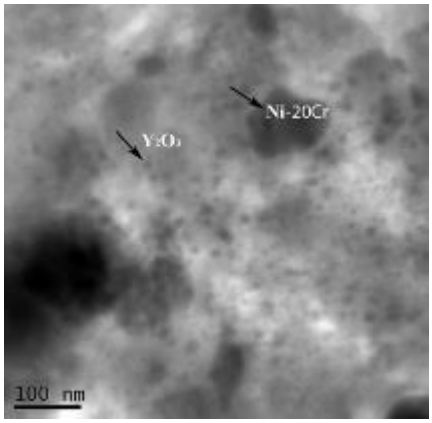

Figure 57. A TEM micrograph of the ball milled (2 h) Ni-20Cr-1.2Y_2O_3 alloy.

The SPSed Ni-20Cr and Ni-20Cr-1.2Y_2O_3 alloys were further characterized for microstructure. The microstructural characteristics were examined using XRD, SEM and TEM. However, SEM performed on the specimens could not provide detailed description of the microstructure due to the strong etchant (aqua regia). The XRD results of the SPSed Ni-20Cr and Ni-20Cr-1.2Y_2O_3 alloys revealed the presence of Cr_2O_3 and Cr_2O_5 as well as Cr_3C_2 and Cr_7C_3. Some blocky particles were also observed in the SEM micrographs that were highly enriched in Cr. These particles were not observed in TEM due to the electropolishing artifact.

Figure 58a shows a bright field TEM image of the SPSed Ni-20Cr alloy while Figure 58b shows that of the SPSed Ni-20Cr-1.2Y_2O_3 alloy. Both images were taken under the same magnification to better compare between the two microstructures. The grain size of the Ni-20Cr-1.2Y_2O_3 alloy was found to be considerably larger than that of Ni-20Cr alloy. The average grain size of the Ni-20Cr-1.2Y_2O_3 alloy was measured to be 130 nm while that of the Ni-20Cr alloy was about 630 nm. The effect of Y_2O_3 addition on the grain size is clearly evident. The presence of homogeneously distributed nanodispersoids in a large volume fraction led to a higher microhardness and grain refinement in the Ni-20Cr-1.2Y_2O_3 alloy.

Twin bands were observed frequently in the SPSed Ni-20Cr alloy as shown in Fig. 59a. On the other hand, Fig. 59b shows the twin bands that were occasionally observed in some larger grains in the microstructure of the Ni-20Cr-1.2Y_2O_3 alloy. Boundaries of the twin bands were straight-edged, as typically shown by annealing twins. While the origin of the twin bands in the SPSed alloys is not clear at this point, it is likely that twin bands are of *annealing origin* created during the recrystallization of the ball milled powder at certain stage during SPS.

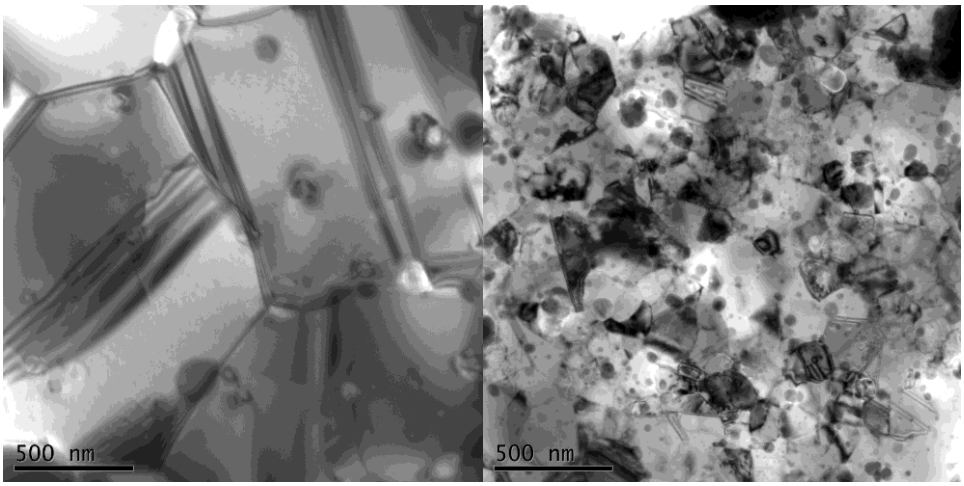

(a) (b)

Figure 58. TEM bright field images of SPSed a) Ni-20Cr and b) Ni-20Cr-1.2Y_2O_3 alloys.

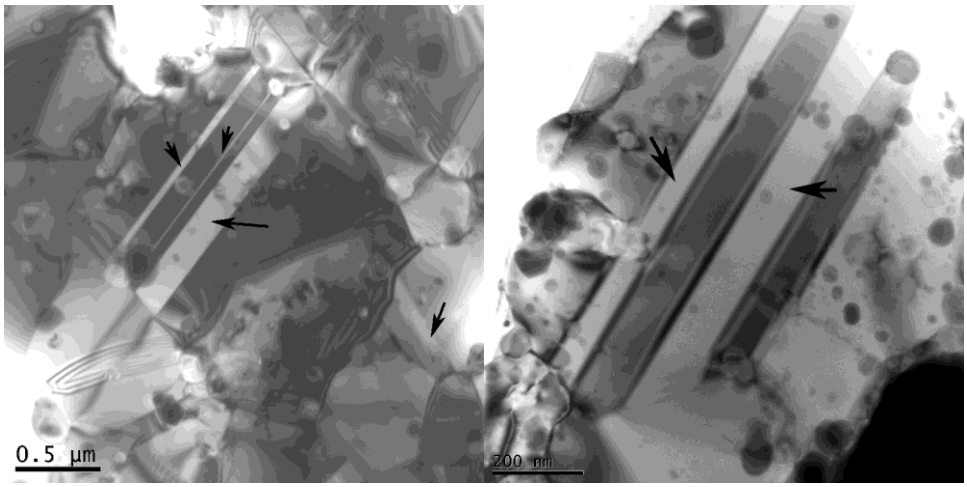

(a) (b)

Figure 59. Twin bands observed in the SPSed a) Ni-20Cr and b) Ni-20Cr-1.2Y_2O_3 alloys.

Figures 60a and b show the second phase particles in the SPSed Ni-20Cr and Ni-20Cr-1.2 Y_2O_3 alloys, respectively. The majority of the particles in the SPSed Ni-20Cr alloy were in a wide size range of 22-180 nm. On the other hand, the microstructure of Ni-20Cr-1.2Y_2O_3 alloy contained a larger fraction of the smaller particles (the particles diameter varied between 3-50 nm). It is likely that at the elevated temperatures during SPS Cr started precipitating out of the Ni-Cr solid solution in the form of Cr based oxides and carbides.

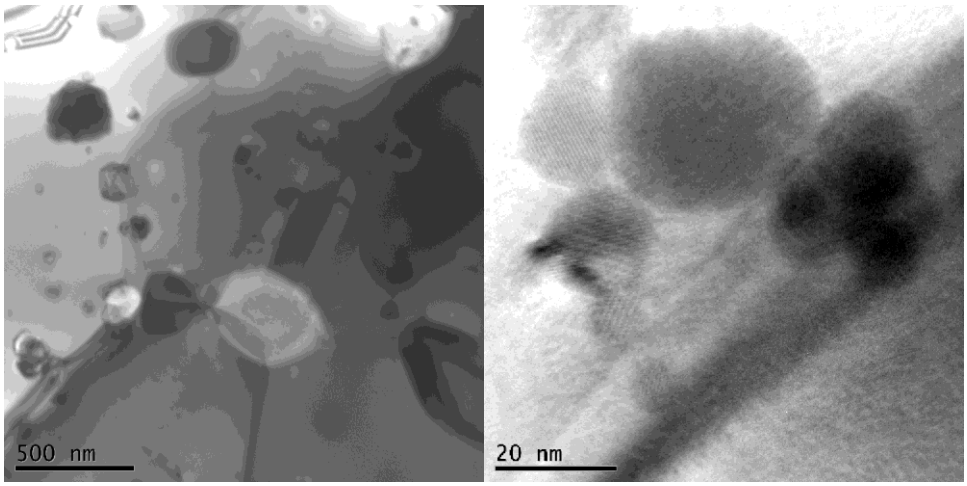

(a) (b)

Figure 60. Particles in the (a) SPSed Ni-20Cr alloy and (b) Ni-20Cr-1.2Y_2O_3 alloy

Yttrium-containing particles as small as 3-5 nm in diameter were also detected in the microstructure of Ni-20Cr-1.2Y_2O_3 alloy. The fine and stable particles were crucial for retaining a finer grain size in Ni-20Cr-1.2Y_2O_3 alloy. The microhardness of the Ni-20Cr-1.2Y_2O_3 alloy was higher than that of Ni-20Cr alloy mainly due to the greater contributions of particle strengthening and Hall-Petch strengthening effects.

The microstructural characteristics examined by transmission electron microscopy of SPSed Ni-20Cr and Ni-20Cr-1.2Y_2O_3 alloy were discussed above. Those alloys were fabricated from material milled for 2 h and SPSed at a temperature of 1100 ^oC and a dwell time of 30 min. Three main oxide particle categories were: i) Ni-based oxide in the range of 80-100 nm in diameter; ii) Cr-based oxide in the range of 20-60 nm in diameter; and iii) Y-based oxide smaller than < 15 nm in diameter. Fig. 61a shows a TEM image of the aforementioned SPSed alloy mainly the yttria based particles. Energy dispersive spectroscopy (EDS) was carried out on these small samples which showed that yttrium is present in the small particles. Peaks of other elements (Ni, Cr, Si) also appeared because of the 'matrix effect'.

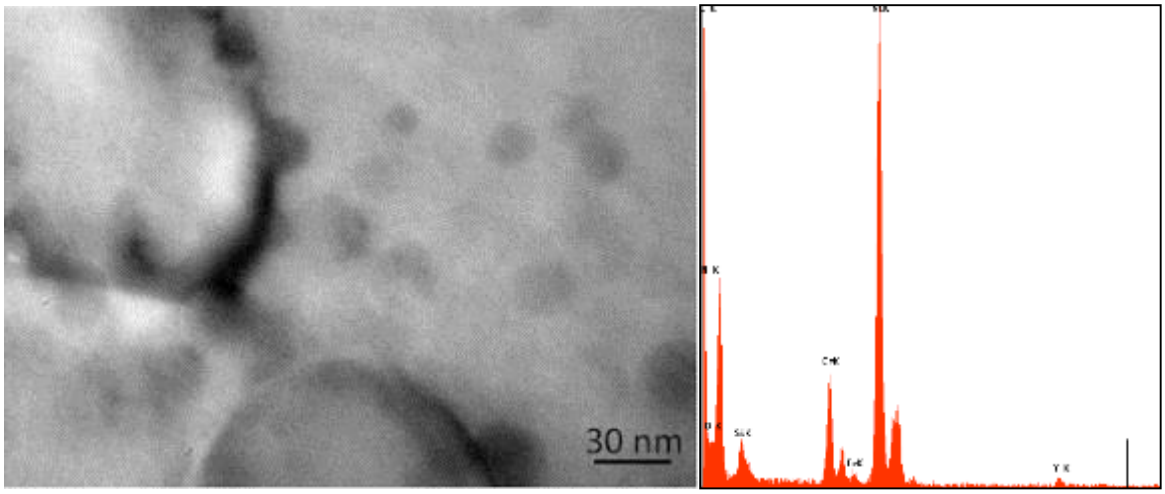

(a) (b)

Figure 61. (a) A TEM image of the SPSed Ni-20Cr-1.2Y_2O_3 alloy. (b) The EDS spectrum taken from the small particles shows the presence of yttrium.

Further TEM study was carried out on the samples of Ni-20Cr-1.2Y_2O_3 alloy processed under two different conditions. One sample was milled for 2 h but SPSed at 900 ^oC for 5 min. Another sample was milled for a longer period (4 h) but SPSed at 1100 ^oC for 30 min. Electro-jetpolishing was used to prepare the TEM specimens. The electrolytic bath contained a mixture of methanol and nitric acid (80:20 by volume). Dry ice was used to cool the solution to a temperature between -35 and -40 ^oC.

Figure 62a-b show bright field TEM images of the SPSed Ni-20Cr-1.2Y_2O_3 alloy (2 h milled / SPS – 900 ^oC / 5 min). Sintering at lower temperatures leads to smaller grains; however presence of sub-grains with sub-grain boundaries were also visible. Twins were much less developed. Such microstructural evolution was due to the lower sintering temperature and time. It is to note that similar kind of particle microstructure was observed in this sample as was observed in other SPSed Ni-20Cr-1.2Y_2O_3 alloys. Despite apparently favorable microstructural characteristics, the material exhibited lower hardness (395 HVN) due to a higher amount of porosity (relative density of 93.9%).

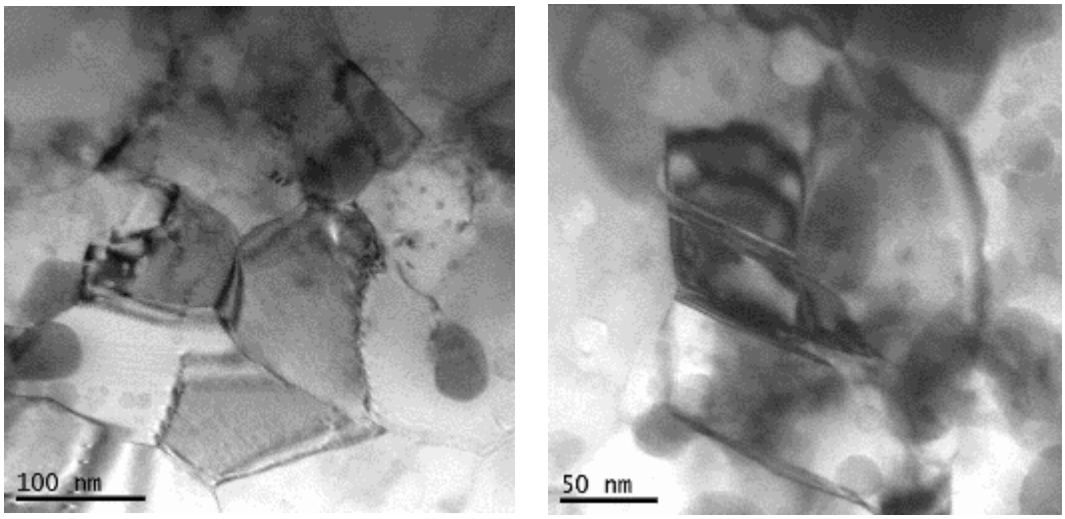

(a) (b)

Figure 62. (a) and (b) TEM bright field images showing the grain structure and particle microstructure in the SPSed Ni-20Cr-1.2Y_2O_3 alloy (milled – 2h, SPS – 900 ^oC/5 min).

Figure 63 shows TEM images and corresponding selected area diffraction (SAD) patterns from the other SPSed sample (milled for 4 h, and SPSed at 1100 ^oC for 30 min). With increasing milling time from 2 to 4 h, there was a tendency for development of a moderate bimodal grain size distribution. Fig. 63a shows a TEM bright field image from the nanocrystalline region where the grain size was close to 100 nm. The SAD pattern in Fig. 63b shows a clear ring diffraction pattern confirming the presence of tiny crystallites. On the other hand, Figure 63c shows a larger grain region where the grain size is 200-300 nm (still considered ultrafine grains). The corresponding SAD pattern is shown in Fig. 63d which is a true ring diffraction pattern. While the exact reason for the bimodal grain size distribution is not clear at this point, it is possibly related to dissolution of some yttria into the Ni-Cr matrix due to the longer milling time.

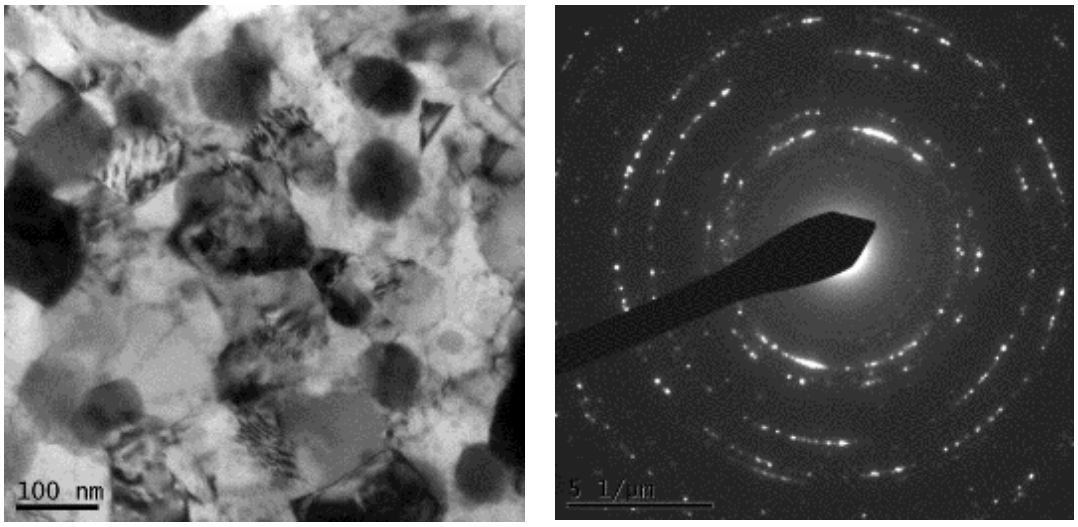

(a) (b)

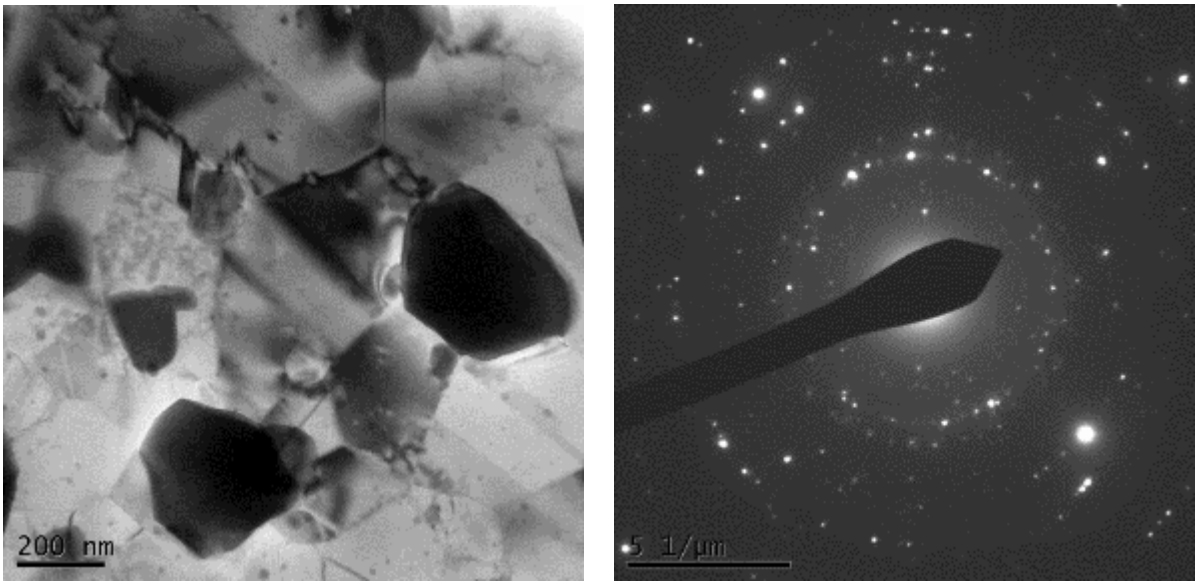

(c) (d)

Figure 63. (a) A bright field TEM image of the Ni-20Cr-1.2Y_2O_3 alloy (milled for 4 h, SPSed at 1100 ºC for 30 min) from the smaller grain region and (b) the corresponding SAD pattern. (c) A bright field TEM image of the same sample from the larger grain region and (d) the corresponding SAD pattern.

A TEM thin lamella of the Ni-20Cr-1.2Y_2O_3-5Al_2O_3 sintered at 1100 ºC for 30 min under a pressure of 80 MPa sample was prepared by the FIB technique and is shown in Fig. 64. The TEM micrograph of the sintered Ni-20Cr-1.2Y_2O_3-5Al_2O_3 alloy is shown in Figs. 65a-d.

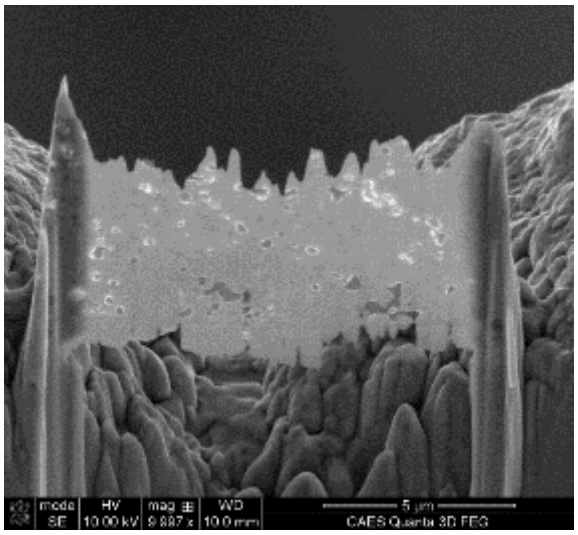

Figure 64. The TEM lamella from the sintered Ni-20Cr-1.2Y_2O_3-5Al_2O_3 alloy prepared by FIB.

The microstructure of the sintered Ni-20Cr-1.2Y_2O_3-5Al_2O_3 alloy is shown in Fig. 65a. Equiaxed recrystallized grains with an average grain size of 340 nm can be observed. For comparison, the average grain sizes of the sintered Ni-20Cr and Ni-20Cr-1.2Y_2O_3 alloys were measured to be 630 nm and 130 nm, respectively. Another bright field micrograph at a higher

magnification is shown in Fig. 65b. The dark field micrograph and the diffraction pattern corresponding to Fig. 65b are shown in Figs. 65c and 65d, respectively.

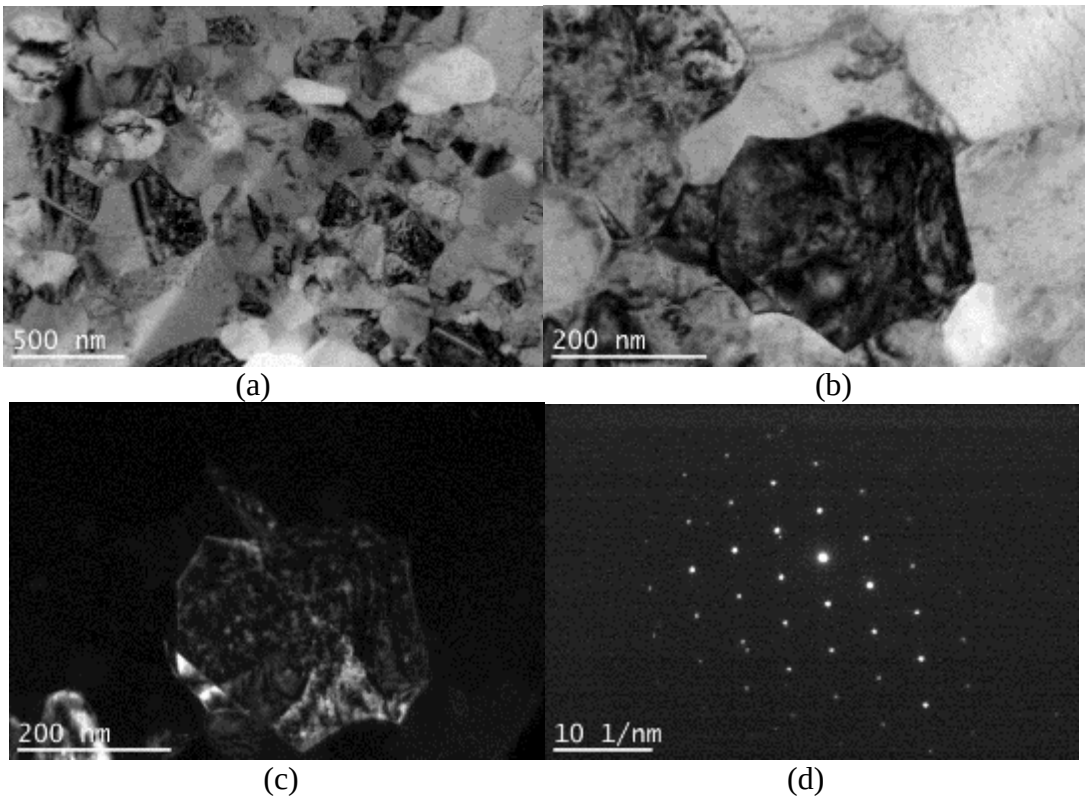

Figure 65. The TEM micrographs from the lamella with a nominal composition of Ni-20Cr-1.2Y_2O_3-5Al_2O_3 after sintering at 1100 ^oC for 30 min: (a) a bright field image overview of the microstructure, (b) BF image showing recrystallized grains, (c) DF from Fig. 65b, and (d) the diffraction pattern obtained from Fig. 65(b).

A bright field and a HRTEM micrograph of twins in Ni-20Cr-1.2Y_2O_3-5Al_2O_3 alloy are shown in Figs. 66a and 66b, respectively. Twins have also been observed in Ni-20Cr and Ni-20Cr-1.2Y_2O_3-5Al_2O_3 alloys. The twins are likely annealing twins and need to be investigated further.

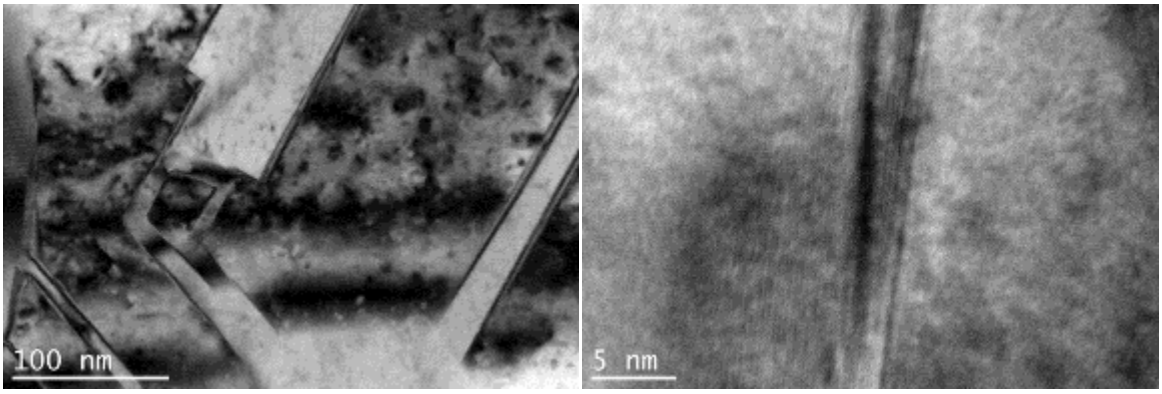

Figure 66. (a) TEM BF image showing twins and (b) HRTEM image of twins in Ni-20Cr-1.2Y_2O_3-5Al_2O_3 alloy.

Figure 67a shows a HDAAF image from Ni-20Cr-1.2Y_2O_3-5Al_2O_3 alloy with 4 different Z contrast region. EDS analysis was conducted on these four areas and the results are given in Figs. 68b-e, respectively.

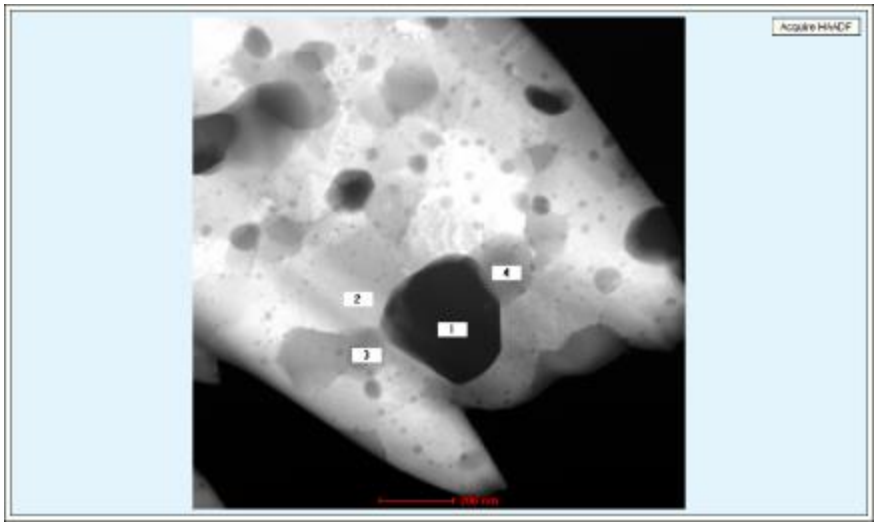

(a)

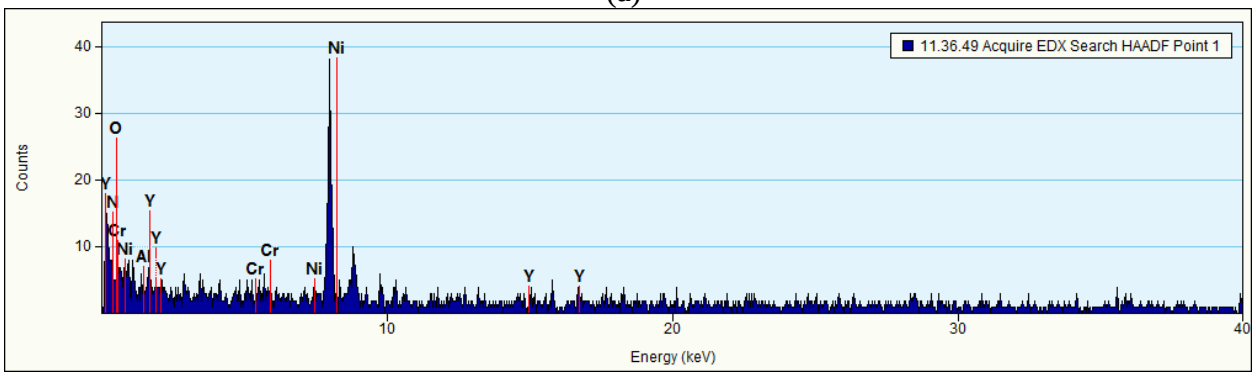

(b)

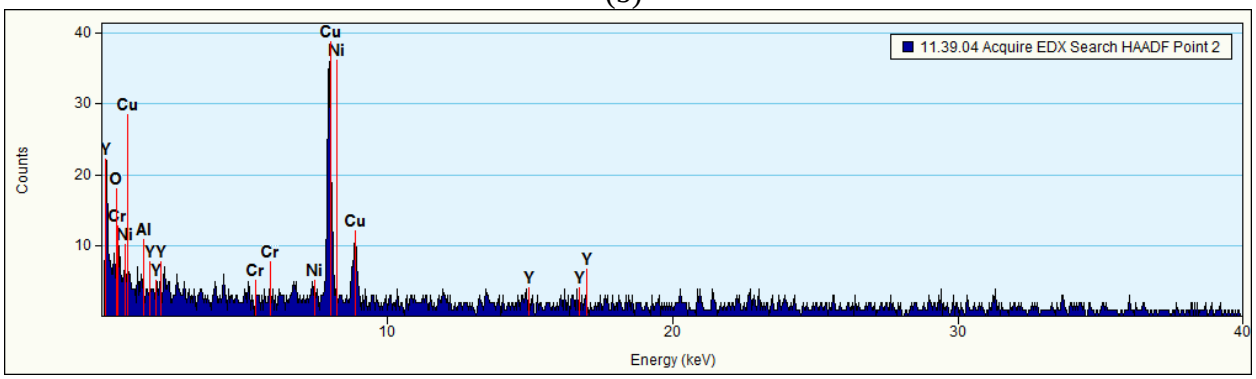

(c)

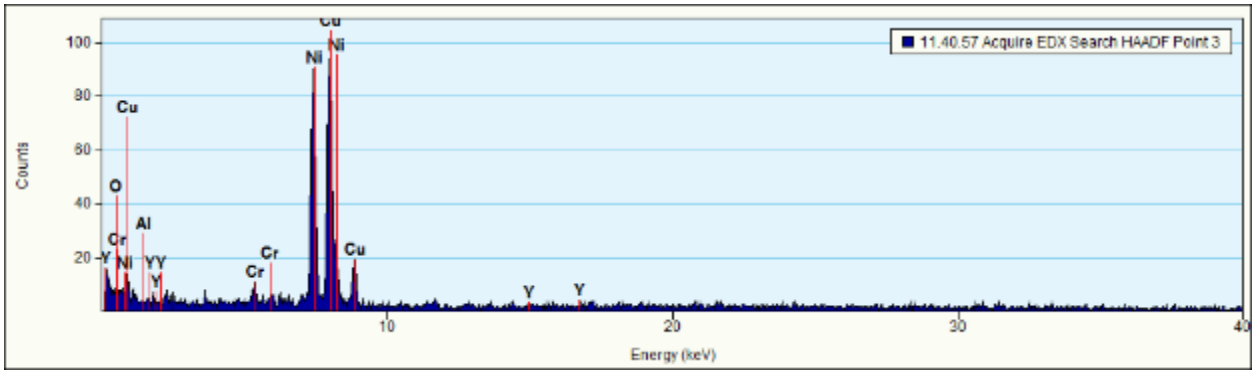

(d)

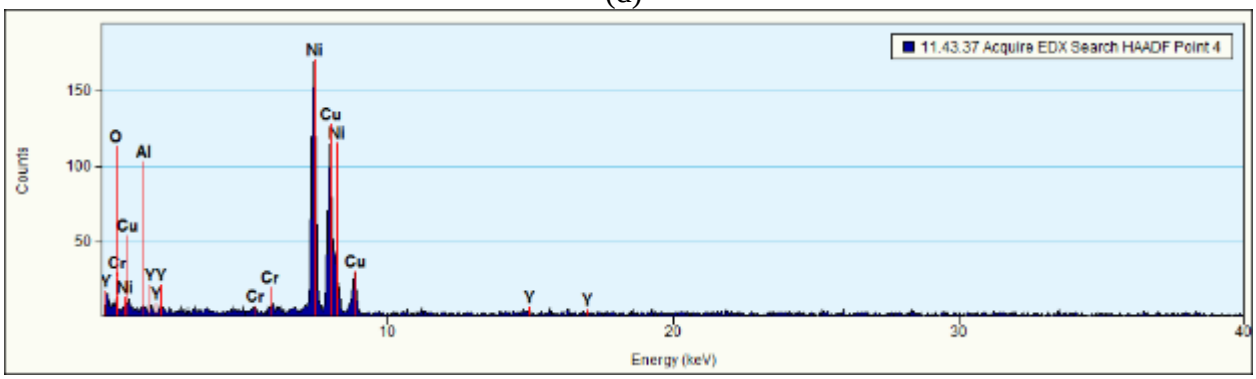

(e)

Figure 67. (a) HDAAF image from Ni-20Cr-1.2Y_2O_3-5Al_2O_3 alloy with 4 different Z contrast areas, (b) EDS spectrum of area 1, (c) EDS spectrum of area 2, (d) EDS spectrum of area 3, and (e) EDS spectrum of area 4.

Figure 68a shows a HDAAF image from a different location on Ni-20Cr-1.2Y_2O_3-5Al_2O_3 alloy along with the EDS spectrum given in Figs. 68b-e, respectively.

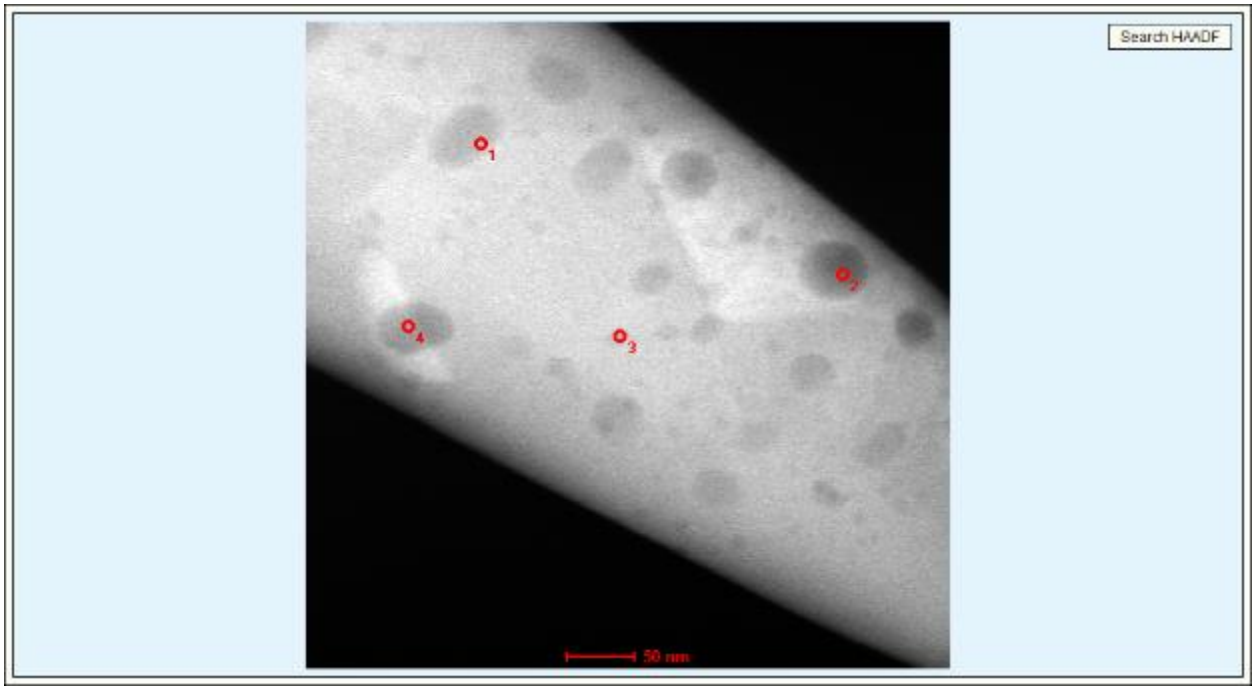
Search HAADF
1
2
3
4
50 nm

(a)

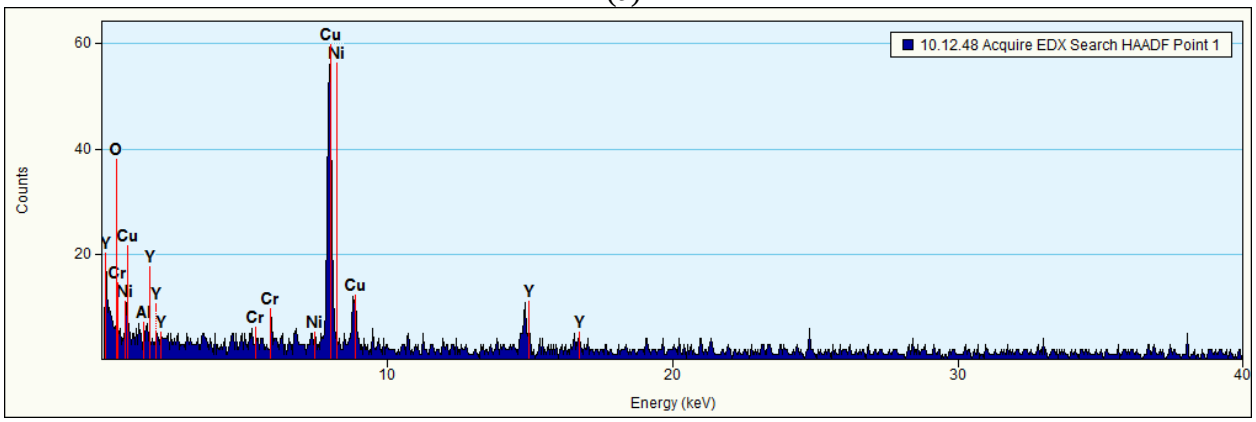
10.12.48 Acquire EDX Search HAADF Point 1
Counts
Energy (keV)
O
Cu
Ni
Cr
Y
Al

(b)

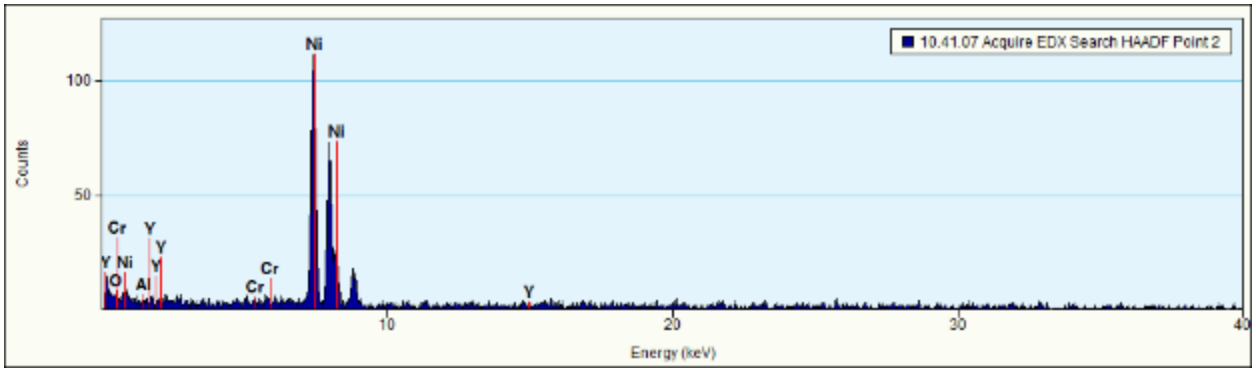
10.41.07 Acquire EDX Search HAADF Point 2
Counts
Energy (keV)
Ni
Cr
Y
O
Al

(c)

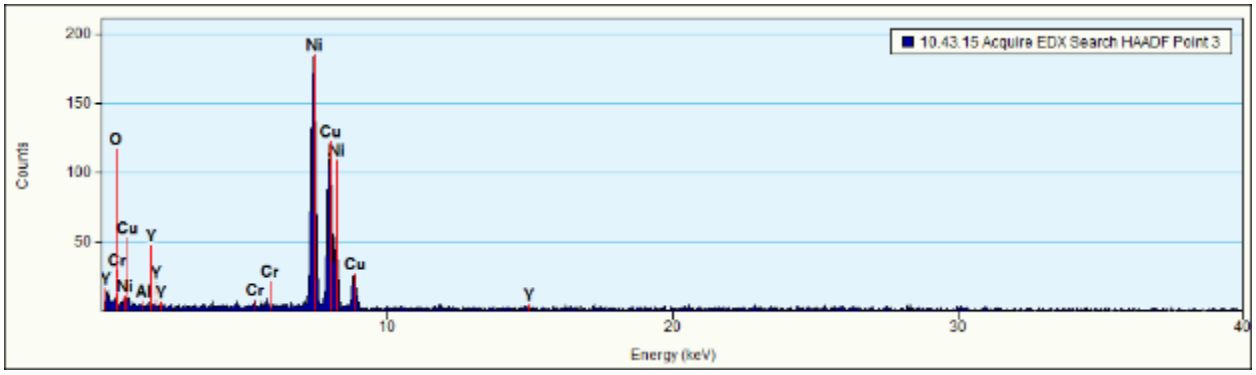

(d)

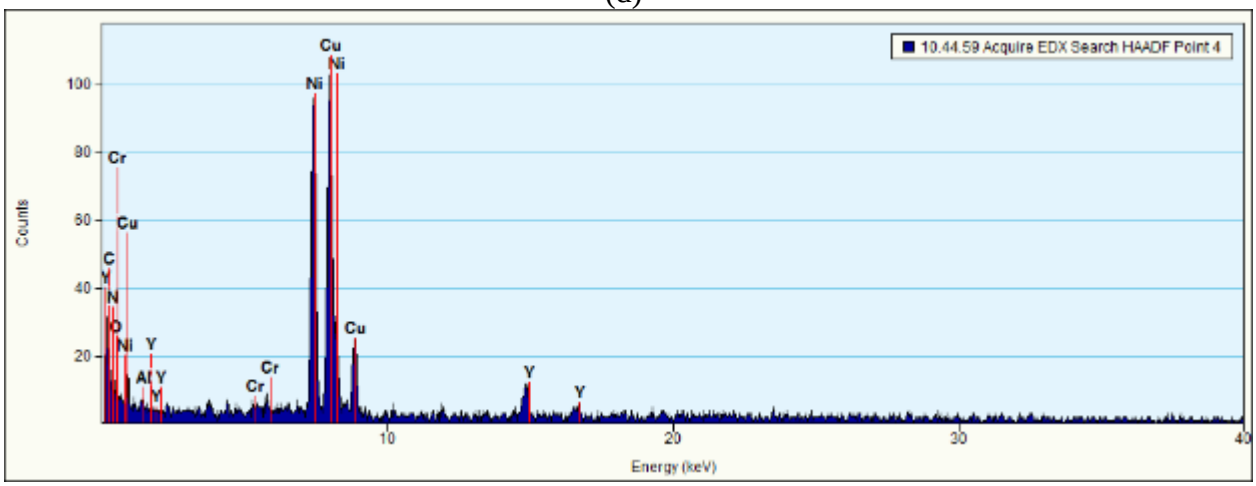

(e)

Figure 68. (a) A HDAAF image from Ni20Cr1.2Y_2O_3 5Al_2O_3 with 4 different Z contrast areas, (b) EDS spectrum of area 1, (c) EDS spectrum of area 2, (d) EDS spectrum of area 3 and (e) EDS spectrum of area 4.

Effect of milling time

The microstructure of the sintered Ni-20Cr-1.2Y_2O_3 specimens milled for 0 h, 2 h and 4 h (alloy A, B and C, respectively) are shown in Figs. 69a-d, respectively. The microstructure of alloy A was observed using EBSD because of coarser grains as shown in Fig. 69a. The grains were equiaxed and fully recrystallized with average size of 8 μm. A high volume fraction of annealing twins and Σ3 boundaries were observed in Fig. 69a. Figure 69b shows a bright field TEM image from the 2 h milled Ni-20Cr-1.2Y_2O_3 (alloy B) with randomly oriented nanograins smaller than 300 nm. The presence of homogeneously distributed nanoparticles in a large volume fraction led to a significant grain refinement in microstructure of Ni-20Cr-1.2Y_2O_3 alloy. The microstructure of Ni-20Cr-1.2Y_2O_3 alloy after milling for 4 h (alloy C) revealed a bimodal grain size distribution containing nanograins with an average size of 120 nm as shown in Fig. 69c and coarser grains with an average size of 400 nm as shown in Fig. 69d. The corresponding SAD patterns obtained from Figs. 69c and 69d also confirmed this bimodal grain size distribution.

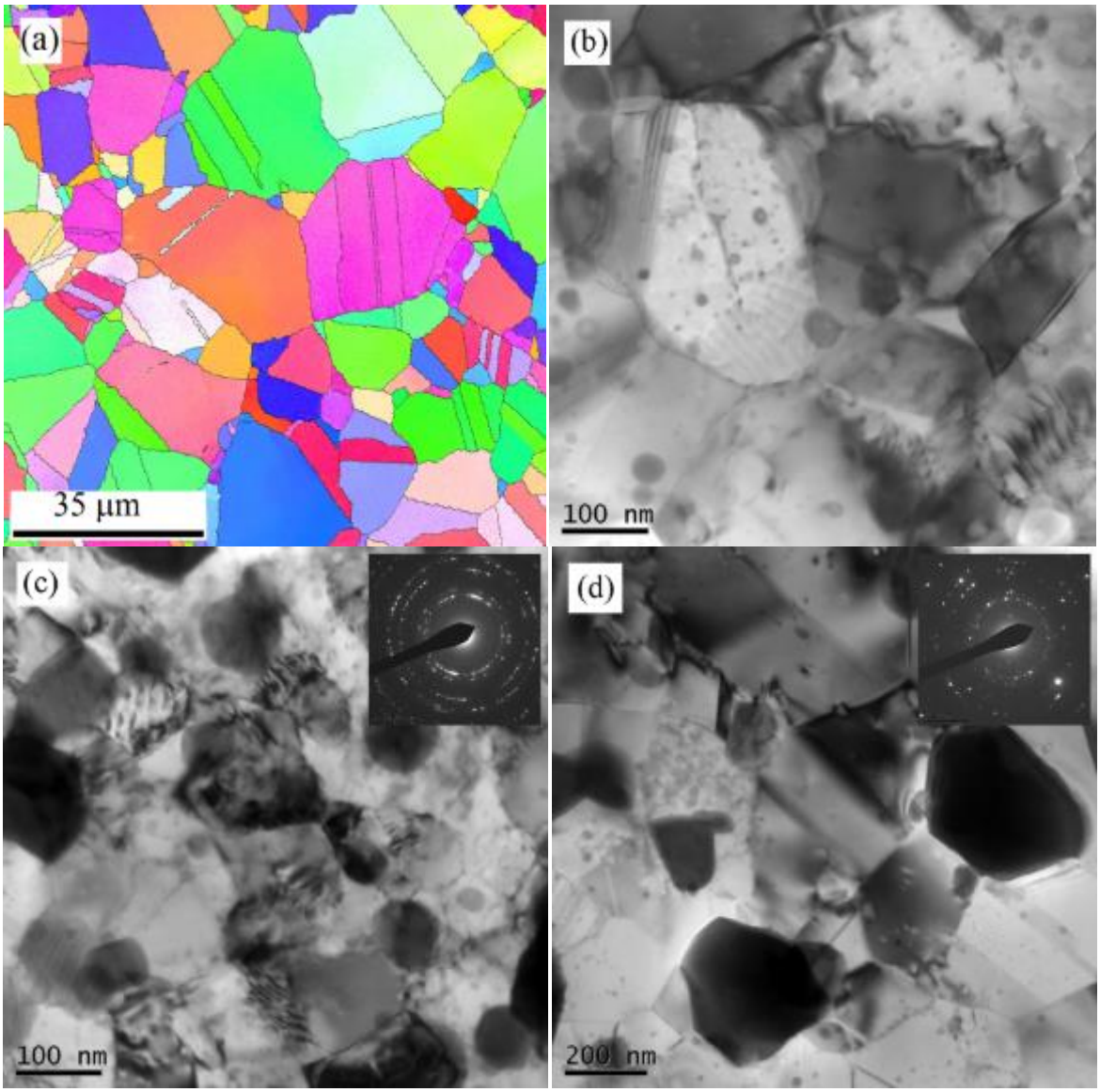

Figure 69. The micrographs of Ni-20Cr-1.2Y_2O_3 alloy milled for (a) 0 h (alloy A), (b) 2 h (alloy B), (c) 4 h (alloy C) showing nanograins and (d) 4 h (alloy C) showing coarser grains.

Figures 70a-b show the second phase particles in the sintered Ni-20Cr-1.2Y_2O_3 alloys after milling for 2 h and 4 h, respectively. For alloy B, the smallest and the average particle diameter were determined to be 3 nm and 14 nm, respectively as shown in Fig. 70a. In alloy B, three main categories of oxide particles were found based on energy dispersive spectroscopy (EDS): (1) Ni-based oxides in the range of 80-100 nm; (2) Cr-based oxides in the range of 20-60 nm; and (3) Y-based oxides smaller than < 15 nm. Similarly, the smallest and the average particle diameter were determined to be 2 nm and 7 nm, respectively for alloy C, as shown in Fig. 70b. The average particle size decreased at a longer milling time. The particles in Fig. 70a were mainly Cr-based oxides or Y_2O_3 whereas the majority of particles shown in Fig. 70b had chemical composition close to $YCrO_3$. This could be attributed to possible dissolution and decomposition of Y_2O_3 and formation of $YCrO_3$ as new compounds.

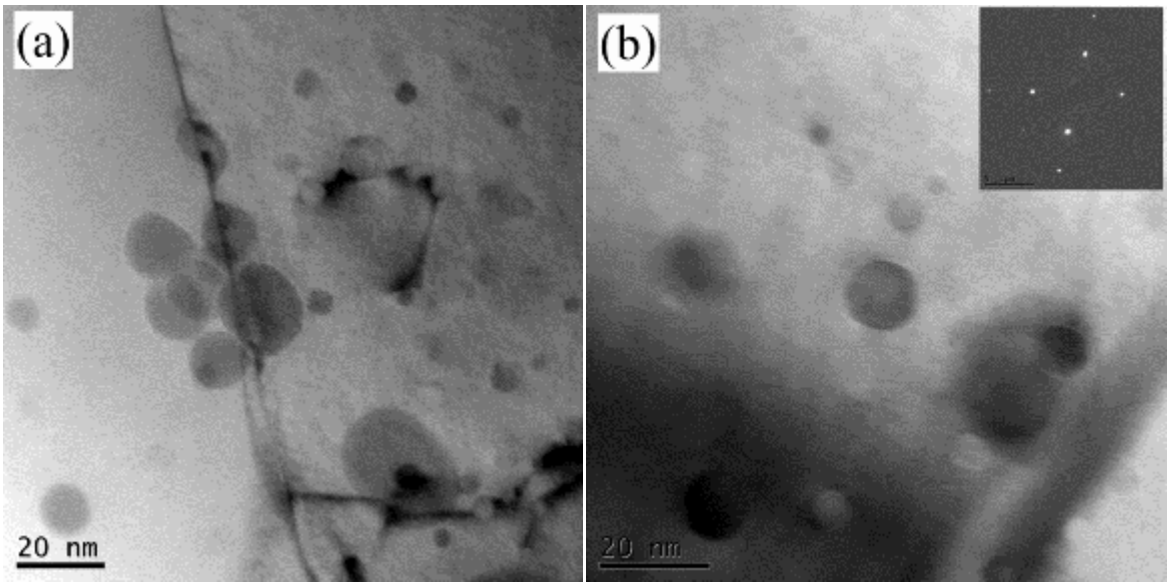

Figure 70**.** The oxide dispersoids in the microstructure of the SPSed Ni-20Cr-1.2Y_2O_3 alloys milled for (a) 2 h (alloy B) and (b) 4 h (alloy C).

Effect of SPS parameters

The overview of microstructure of Ni-20Cr-1.2Y_2O_3 alloy sintered at 900 °C (alloy E), 1100 °C for 5 min (alloy G) and 1100 °C for 30 min (alloy B) are shown in Figs. 71a-c, respectively. Subgrains with an average size of 200 nm were distinguished from each other with arrays of dislocations as shown in Fig. 71a. The grains shown in Fig. 71b were larger with an average size of 350 nm and separated from each other with well-defined sharp boundaries. After sintering of alloy B at 1100 °C for 30 min, the average grain size was reduced even further and an extensive dislocation activity was observed, as shown in Fig. 71c. This could be explained considering that dynamic recrystallization phenomenon likely occurred in the alloy after 30 min at 1100 °C. During dynamic recrystallization, dislocation activity became significant and led to more grain refinement. Meanwhile, the interaction of nanoparticles with dislocations and mobile boundaries effectively inhibited the grain growth process.

The twinning activity as a function of sintering temperature and time can be observed in Figs. 72a-c. The microstructure of Ni-20Cr-1.2Y_2O_3 alloy sintered at 900 °C for 5 minutes (alloy E) shown in Fig. 72a, contained very limited and localized twins with average thickness of 10 nm and volume fraction of 2.8%. The average twin boundary spacing and volume fraction significantly increased to 150 nm and 10%, respectively, after sintering at 1100 °C for 5 minutes (alloy G) as shown in Fig. 72b. Twins in Ni-20Cr-1.2Y_2O_3 alloy sintered at 1100 °C for 30 minutes (alloy B) are shown in Figure 72c, and the average twin boundary spacing and volume fraction were estimated to be 127 nm and 11.6%, respectively. With increasing sintering time from 5 to 30 minutes, the twin boundary width was reduced slightly, but twin boundary volume fraction increased slightly. This could be attributed to the smaller grain size with a higher density of grain boundary areas in alloy B.

The oxide particles in alloy E and G are shown in Figs. 73a-b, respectively. The average particle size in alloy E was measured to be 4.1 nm, and the smallest particle size was found to be 2 nm. Similarly, for alloy G, the average particle size was 12 nm, and the smallest particle size was 4 nm. The oxide particle size increased with increasing sintering temperature and time, plausibly due to faster kinetics of diffusion and particle coarsening at higher sintering temperature and longer sintering time.

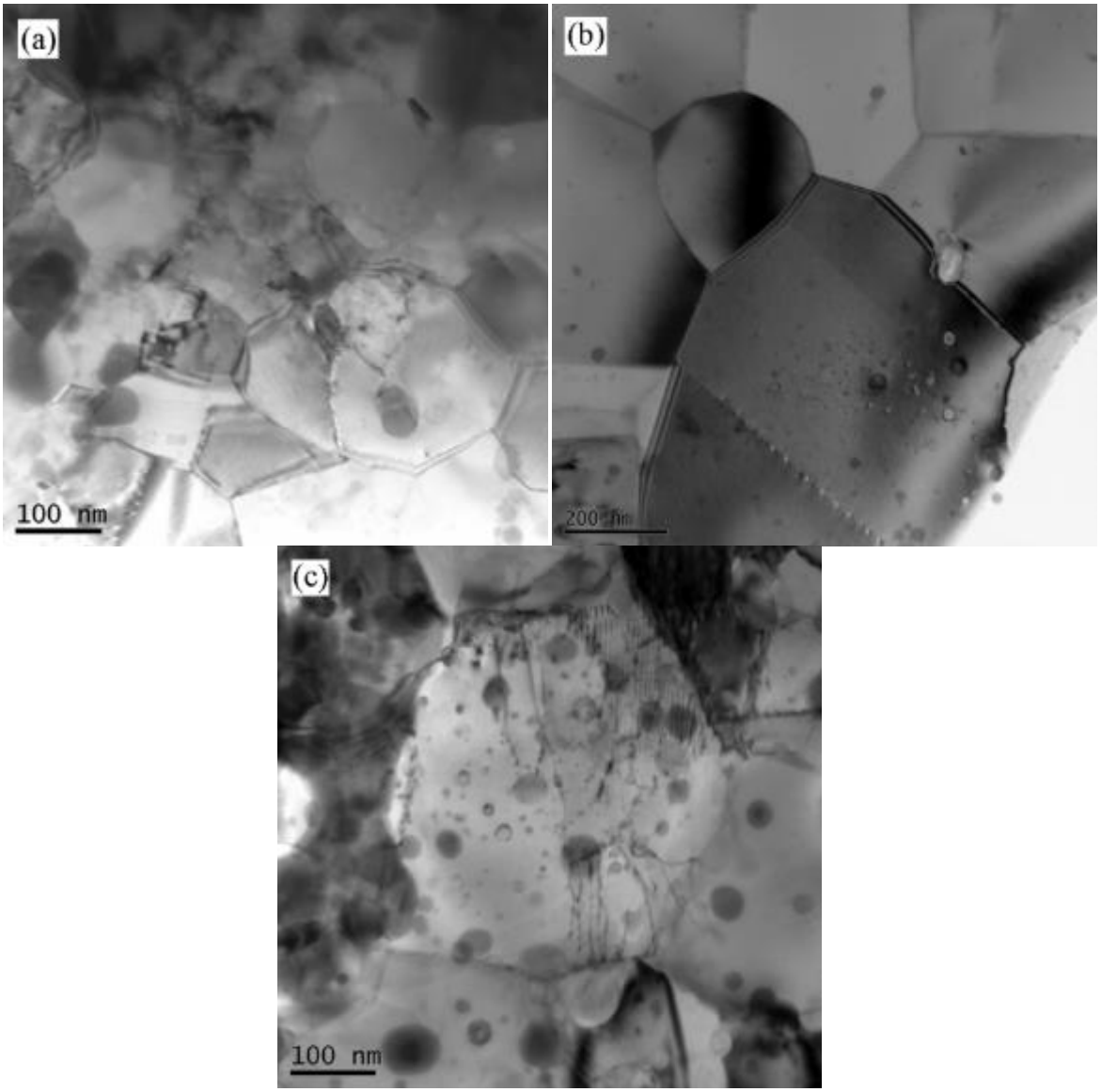

Figure 71. The microstructure of Ni-20Cr-1.2Y_2O_3 alloy sintered at (a) 900 °C for 5 min (alloy E), (b) 1100 °C for 5 min (alloy G) and (c) 1100 °C for 30 min (alloy B).

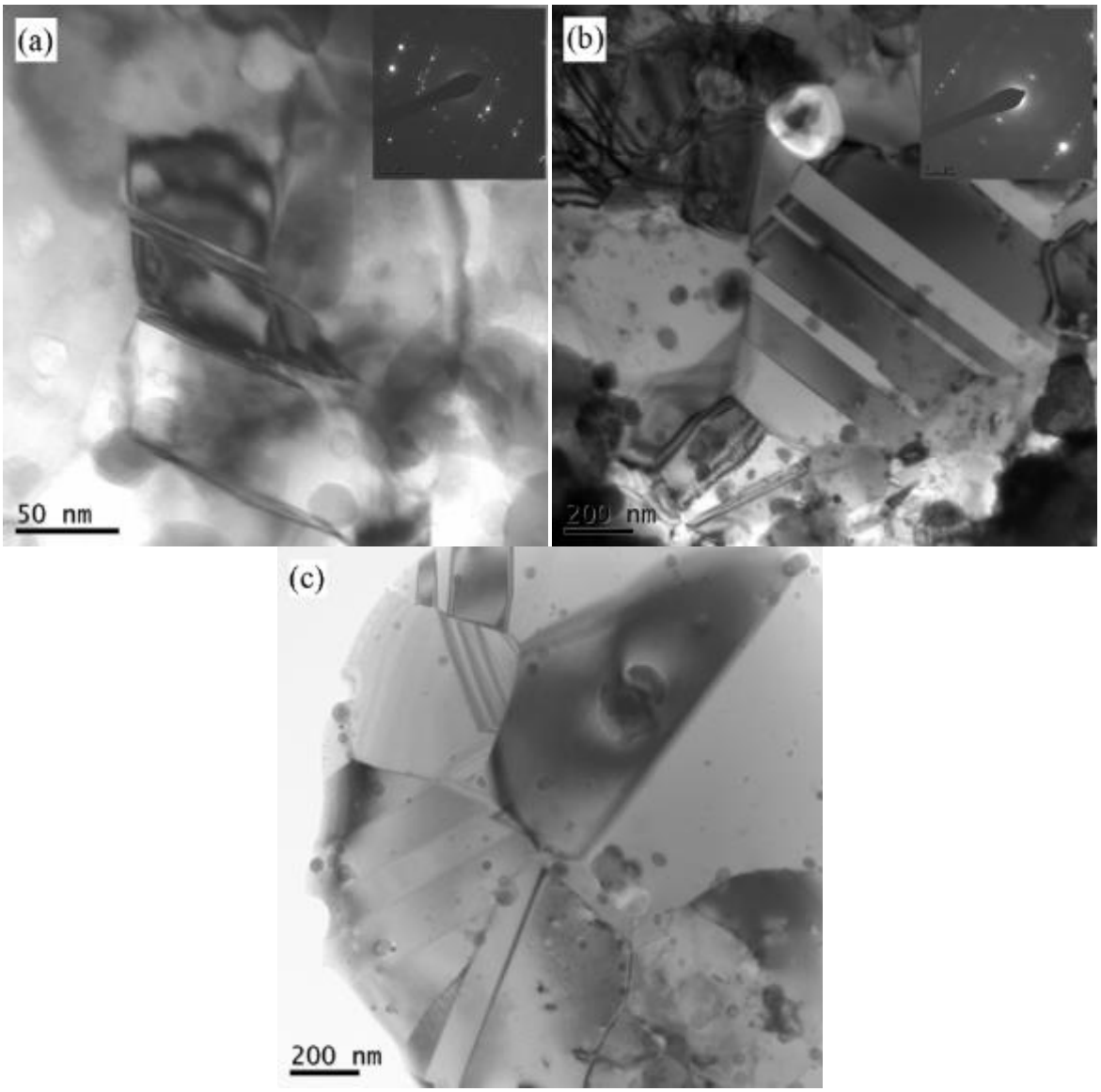

Figure 72. Twins in the microstructure of Ni-20Cr-1.2Y_2O_3 alloys sintered at (a) 900 °C for 5 min (alloy E), (b) 1100 °C for 5 min (alloy G) and (c) 1100 °C for 30 min (alloy B).

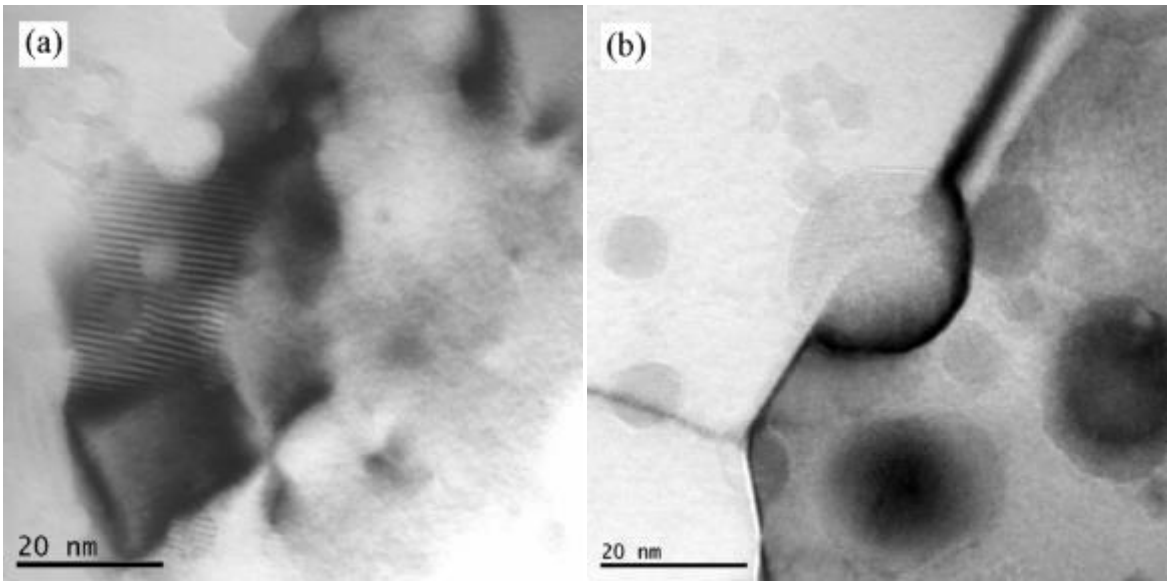

Figure 73. The oxide dispersoid in the microstructure of Ni-20Cr-1.2Y_2O_3 alloy sintered at (a) 900°C for 5 min (alloy E), (b) 1100 °C for 5 min (alloy G).

Effect of alloy composition

The microstructures of Ni-20Cr (alloy H), Ni-20Cr-1.2Y_2O_3 (alloy B) and Ni-20Cr-1.2Y_2O_3-5Al_2O_3 (alloy I) are shown in Figs. 74a-c, respectively. The microstructure of the Ni-20Cr alloy contained fully recrystallized grains with well-defined sharp boundaries and fewer dislocations as shown in Fig. 74a. The average grain size of the Ni-20Cr alloy was measured to be 630 nm, and the number density of oxide particles was less than that of Ni-20Cr-1.2Y_2O_3 formerly shown in Fig. 74a. The effect of Y_2O_3 addition on the grain refinement was clearly evident in Fig. 74b. The presence of homogeneously distributed nanodispersoids in a large volume fraction led to a higher microhardness and grain refinement in the Ni-20Cr-1.2Y_2O_3 alloy. The microstructure of Ni-20Cr-1.2Y_2O_3-5Al_2O_3 (alloy I) is shown in Fig. 74c and revealed randomly oriented grains with extensive dislocation activity and an average grain size of 385 nm.

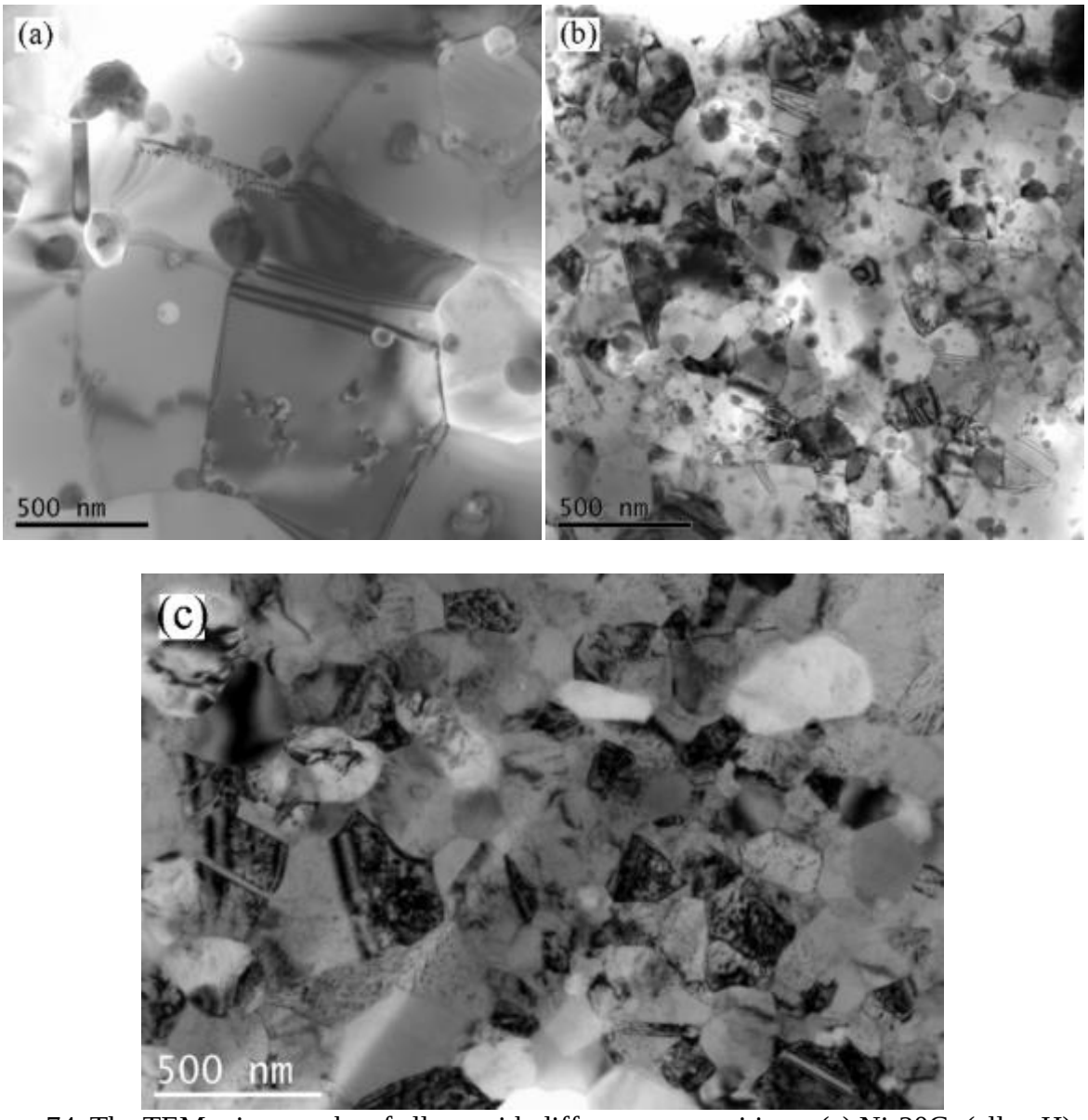

Figure 74. The TEM micrographs of alloys with different compositions; (a) Ni-20Cr (alloy H), (b) Ni-20Cr-1.2Y_2O_3 (alloy B) and (c) Ni-20Cr-1.2Y_2O_3-5Al_2O_3 (alloy I).

The particle size distribution histograms for different alloy compositions are shown in Figs. 75a-c. A broad range of oxide particles were observed in Ni-20Cr alloy as shown Fig. 75a. With addition of Y_2O_3 to Ni-20Cr, both average particle diameter and mean particle separation decreased significantly. In Ni-20Cr-1.2Y_2O_3-5Al_2O_3 alloy, there was a range of nanoparticles smaller than 15 nm and coarser particles larger than 250 nm.

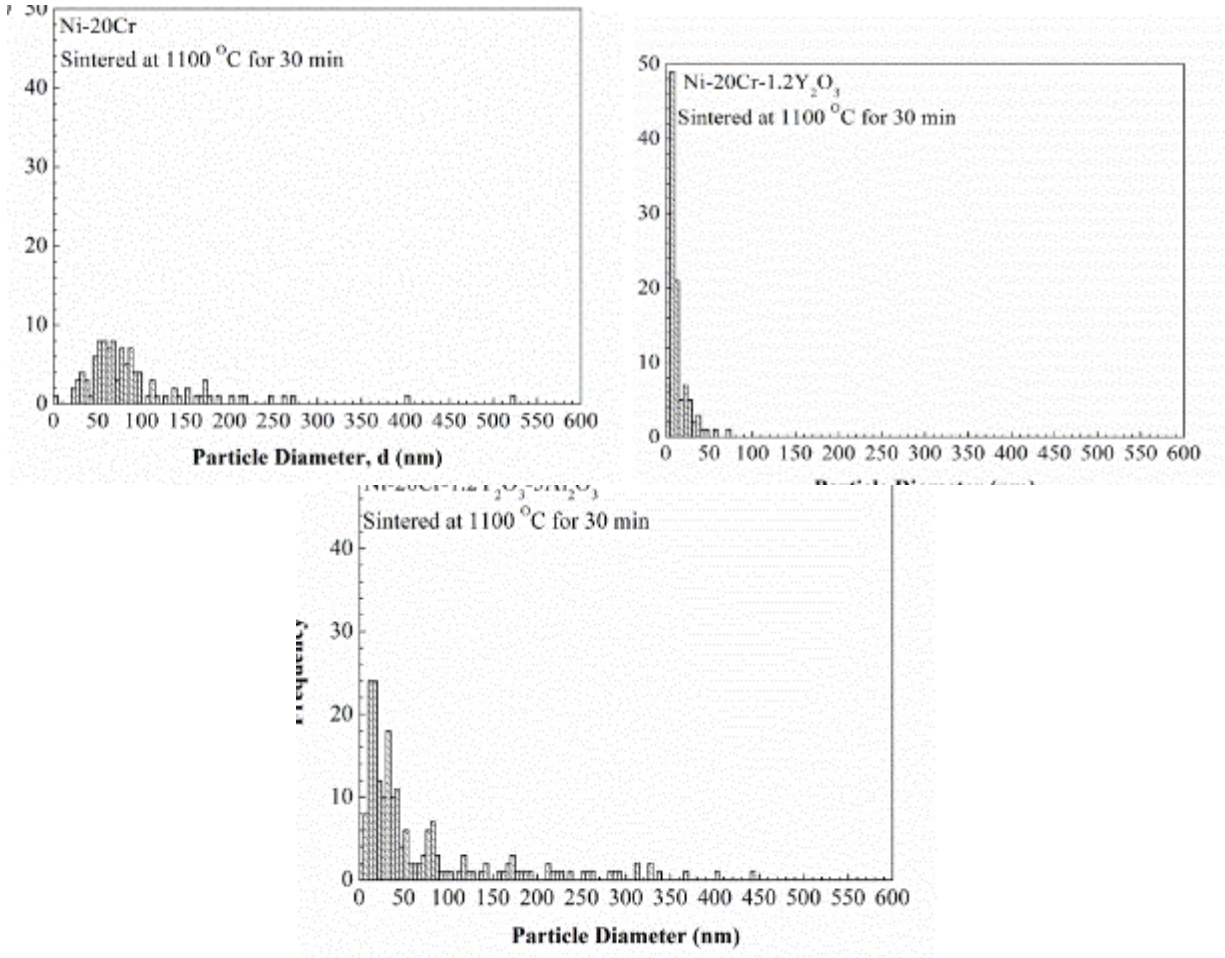

Figure 75**.** Particle size distribution of alloys with different compositions; (a) alloy H, (b) alloy B, and (c) alloy I (approximately 500 particles were counted for each plot).

Creep

Creep tests were performed in compression mode. Creep tests were performed on three different specimens namely Ni-20Cr, Ni-20Cr-1.2Y_2O_3 and Ni-20Cr-1.2Y_2O_3-5Al_2O_3 for shorter time (~ 20-24 hours) and Ni-20Cr-1.2Y_2O_3 and Ni-20Cr-1.2Y_2O_3-5Al_2O_3 samples were used for longer time (>100hours). Ni-20Cr showed very high minimum creep rate in comparison to others. Ni-20Cr-1.2Y_2O_3-5Al_2O_3 showed best creep resistance among all. Considering best creep resistance, test was performed on Ni-20Cr-1.2Y_2O_3-5Al_2O_3 for more than 850 hours (> 30 days). Testing temperature and applied stress was considered 800^0C and 100 MPa respectively. Figure 76-81 (a) and (b) show the plot for % creep and creep rate for different Ni-ODS alloy for different testing time.

Sample A Ni-20Cr
Dimension of specimen: 6.09 mm × 5.07 mm × 4.30 mm

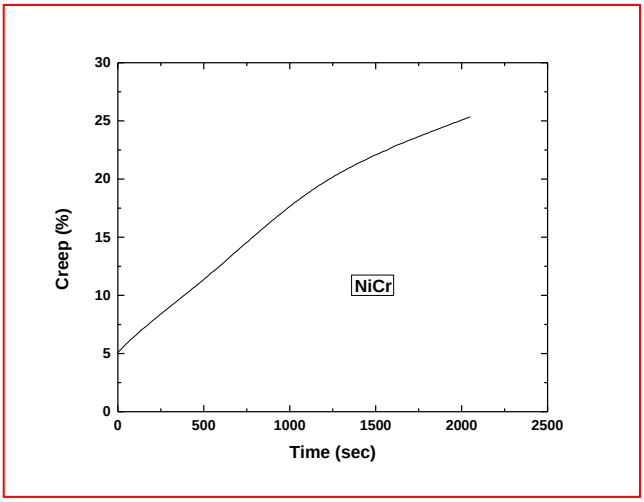

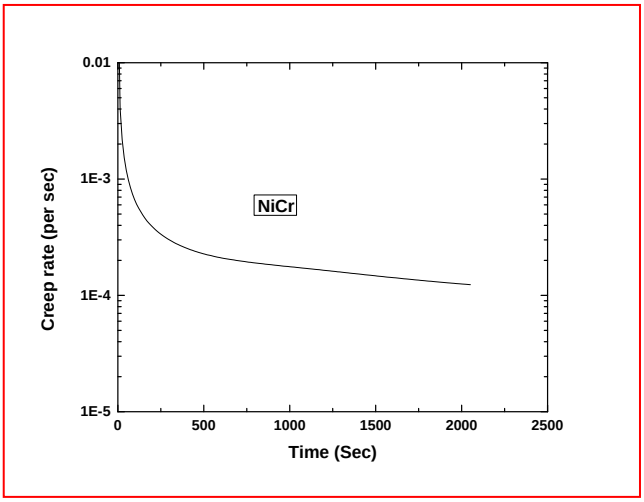

(a) (b)

Figure 76. (a) % creep vs time plot and (b) creep rate vs time plot for Ni-20Cr alloy.

The observed minimum creep rate is approximately 10^{-4}.

Sample B Ni-20Cr -1.2Y_2O_3 (~20-24 hrs)
Dimension of specimen: 9.97 mm × 3.76 mm × 3.77 mm

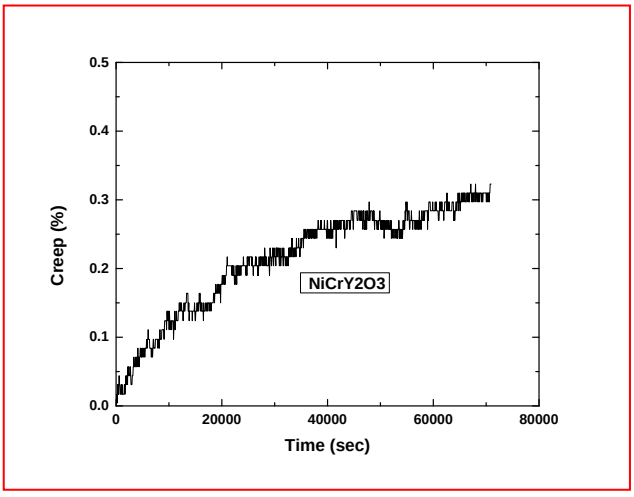

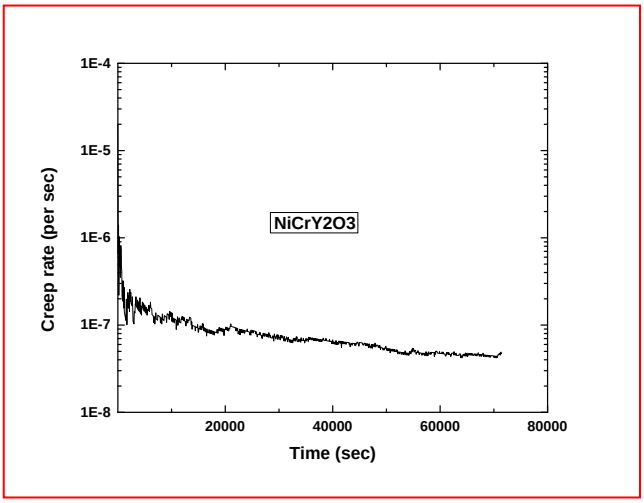

(a) (b)

Figure 77. (a) % creep vs time plot and (b) creep rate vs time plot for Ni-20Cr -1.2Y_2O_3 alloy.

The observed minimum creep rate is approximately. 4.7×10^{-8} s^{-1}.

Sample C Ni-20Cr -1.2Y_2O_3-5Al_2O_3 (~20-24 hrs)
Dimension of specimen: 6.26 mm × 4.71 mm × 4.20 mm

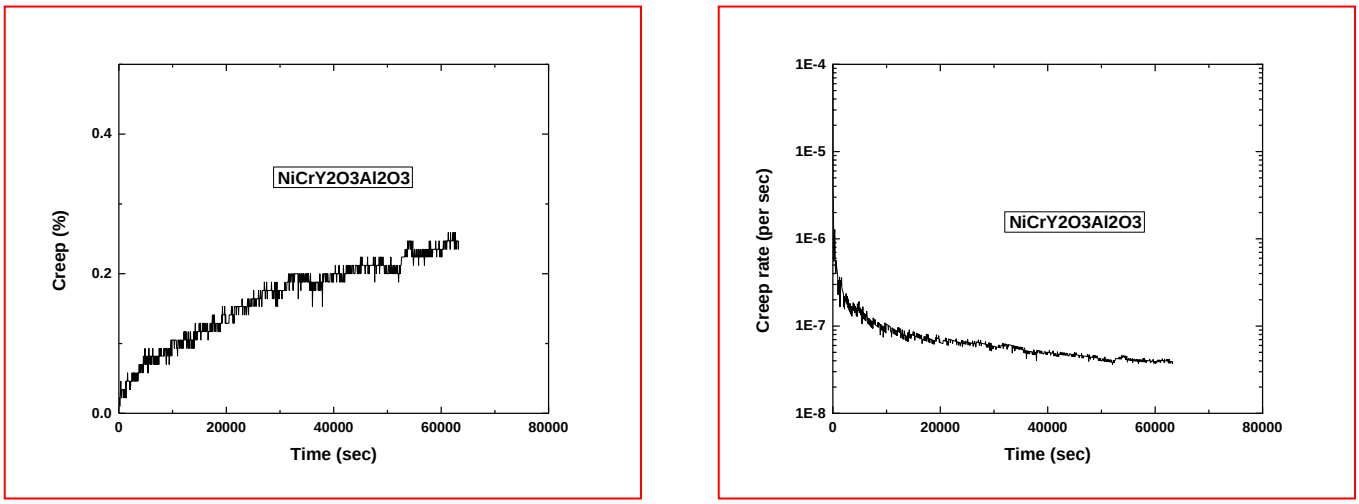

(a) (b)

Figure 78. (a) % creep vs time plot and (b) creep rate vs time plot for Ni-20Cr -1.2Y_2O_3-5Al_2O_3 alloy.

The observed minimum creep rate is approximately. 3.7×10^{-8} s^{-1}.

Sample D Ni-20Cr -1.2Y_2O_3 (> 100 hrs)
Dimension of specimen: 9.97 mm × 3.73 mm × 3.96 mm

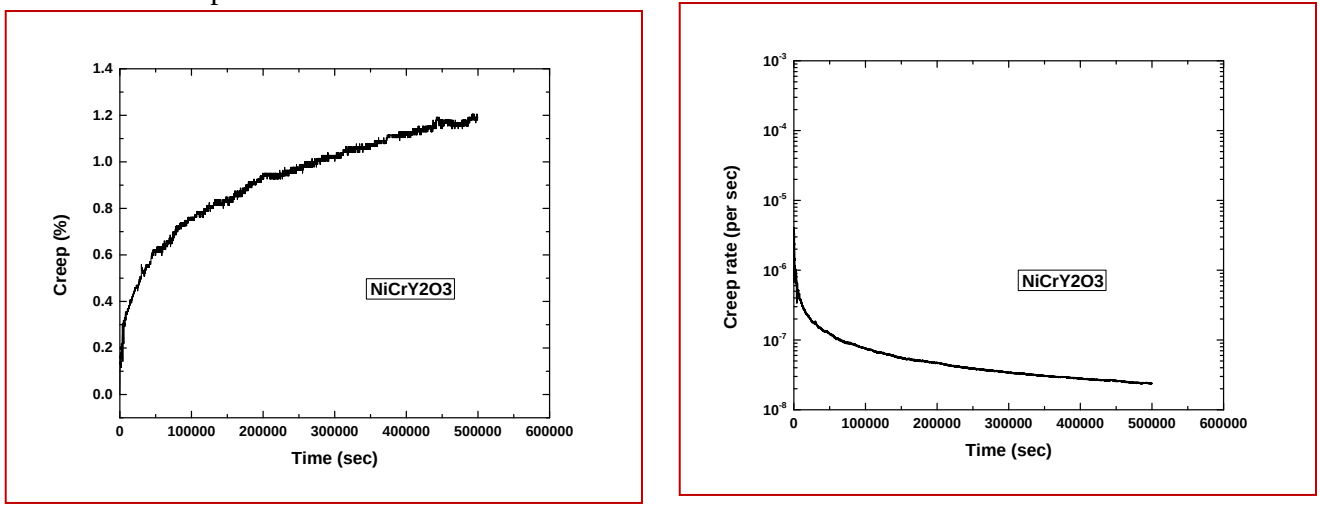

(a) (b)

Figure 79. (a) % creep vs time plot and (b) creep rate vs time plot for Ni-20Cr -1.2Y_2O_3 alloy.

The observed minimum creep rate is approximately. 2.4×10^{-8} s^{-1}.

Sample E Ni-20Cr -1.2Y_2O_3-5Al_2O_3 (>100 hrs)
Dimension of specimen: 4.31 mm × 6.31 mm × 4.09 mm

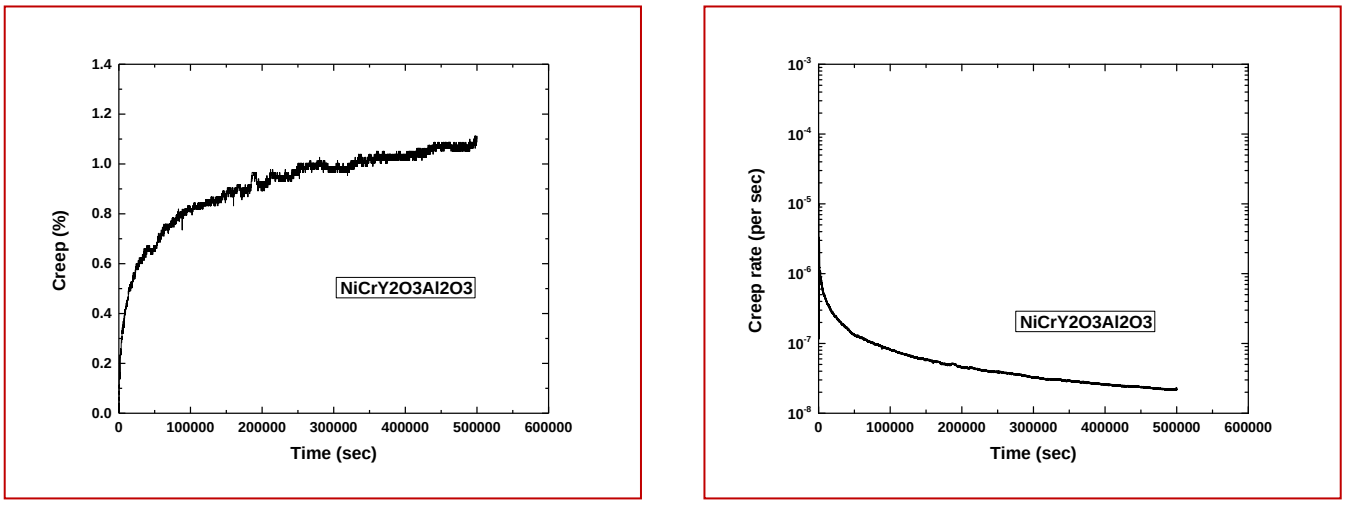

(a) (b)

Figure 80. (a) % creep vs time plot and (b) creep rate vs time plot for Ni-20Cr -1.2Y_2O_3-5Al_2O_3 alloy.

The observed minimum creep rate is approximately. 2.1×10^{-8} s^{-1}.

Sample F: Ni-20Cr -1.2Y_2O_3-5Al_2O_3 (>850 hrs)
Dimension of specimen: 3.91 mm × 6.40 mm × 3.89 mm

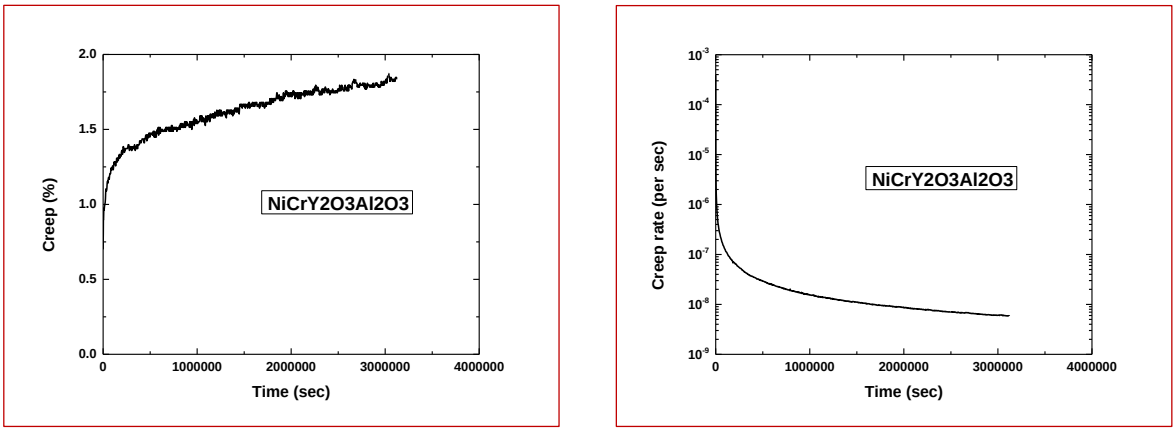

(a) (b)

Figure 81. (a) % creep vs time plot and (b) creep rate vs time plot for Ni-20Cr -1.2Y_2O_3-5Al_2O_3 alloy.

The observed minimum creep rate is approximately. 5.9×10^{-9} s^{-1}.

Creep tests were performed on three different specimens, namely Ni-20Cr, Ni-20Cr-1.2Y_2O_3 and Ni-20Cr-1.2Y_2O_3-5Al_2O_3 for shorter time (~ 20-24 hours) and Ni-20Cr-1.2Y_2O_3 and Ni-20Cr-1.2Y_2O_3-5Al_2O_3 samples were used for longer time (>100hours and > 850 hours). As

expected, Ni-20Cr showed very high minimum creep rate in comparison to others. Ni-20Cr-1.2Y_2O_3-5Al_2O_3 showed best creep resistance among all. Based on above creep results, further creep test was performed on Ni-20Cr-1.2Y_2O_3-5Al_2O_3 for more than 2500 hours (> 100 days).Testing temperature and applied stress was considered 800^oC and 100 MPa, respectively. Figures 82 (a) and (b) show the plot for % creep and creep rate for Ni-20Cr -1.2Y_2O_3-5Al_2O_3 alloy. Another set of tests were conducted at 60, 80 and 100 MPa for short duration with keeping test temperature of 800^oC constant to study the primary creep phenomena.

Sample G: Ni-20Cr -1.2Y_2O_3-5Al_2O_3
Dimension of specimen: 3.90 mm × 6.40 mm × 3.90 mm
Stress: 100 MPa. The observed minimum creep rate is ~ 2.3×10^{-9} s^{-1}.

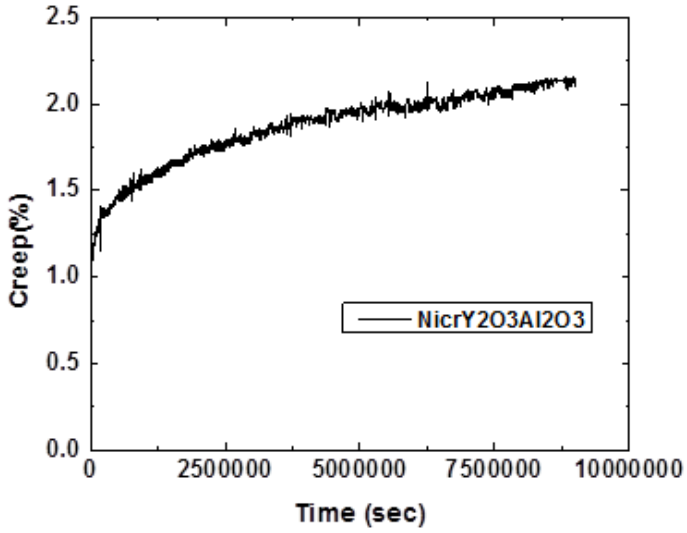

(a)

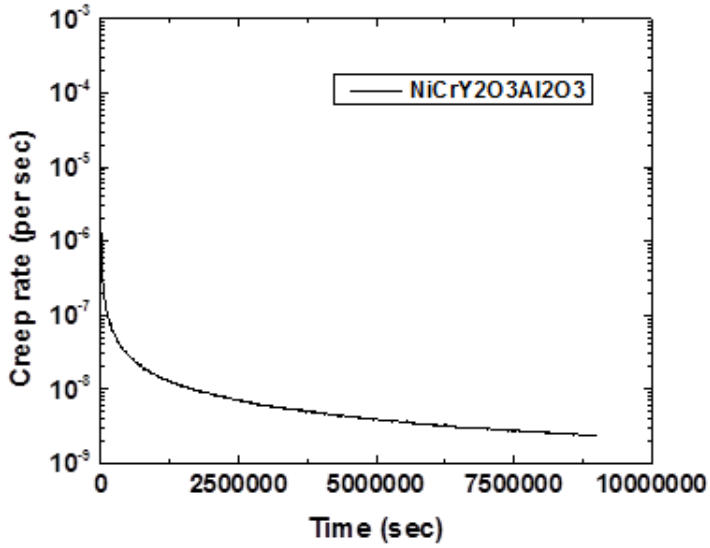

(b)

Figure 82. (a) % creep strain vs time plot, and (b) creep rate vs time plot for Ni-20Cr -1.2Y_2O_3-5Al_2O_3 alloy.

Comparison of minimum creep rate

Figure 83 shows the comparison plot of minimum creep rate for different alloys and testing time. The observed creep rate for Ni-20 Cr is very high in comparison to Ni-20Cr -1.2Y_2O_3 and Ni-20Cr -1.2Y_2O_3-5Al_2O_3 alloys. Ni-20Cr -1.2Y_2O_3-5Al_2O_3 alloy exhibited better creep properties in comparison to Ni-20Cr -1.2Y_2O_3 alloy. Addition of Y_2O_3 in Ni-20Cr improved creep strength significantly. Al_2O_3 addition also showed improvement in creep rate. For shorter testing time the creep rate is relatively high. Decrease in creep rate is observed for longer testing times. The observed creep rate is in order of 10^{-9} s^{-1} for longer time creep test of Ni-20Cr -1.2Y_2O_3-5Al_2O_3.

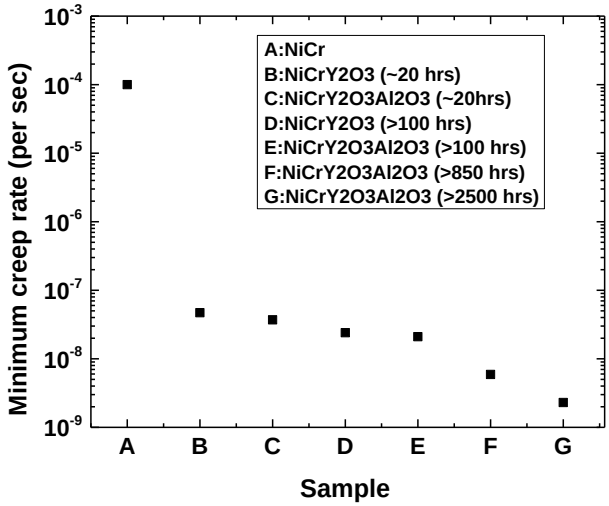

Figure 83. Minimum creep rate comparison plot.

Primary creep study

Primary creep was studied on Ni-20Cr -1.2Y_2O_3-5Al_2O_3 alloy at three different stress levels, namely 60, 80 and 100 MPa, while keeping test temperature constant at 800°C. This is an important aspect because of extended primary creep regime in these alloys. The primary creep strain consists of two parts, namely instantaneous strain and transient strain. With observed data on primary creep, a primary creep curve modeling was carried out. The primary creep curve follows equation either in exponential or power form.

The primary creep curve as in exponential form can be written as

$$\varepsilon_p = \varepsilon_0 + a * \exp(bx) - c * \exp(-dx) \quad (24)$$

where ε_p is the primary strain, $\varepsilon_0$is the instantaneous strain (%), and a, b, c and d are constants which vary with stress and temperature. The constants value is tabulated in table 28.The fitted curves for all three samples are shown in Fig. 84.

Table 28: Constants of primary creep curve equation.

Sample	**ε_0**	**a**	**b**	**c**	**d**
NiCrY2O3Al2O3_100MPa	1.40	2.04	$7.88*10^{-7}$	0.47	$6.83*10^{-5}$
NiCrY2O3Al2O3_80MPa	1.10	1.41	$1.89*10^{-6}$	0.26	$2.42*10^{-5}$
NiCrY2O3Al2O3_60MPa	0.55	0.85	$5.65*10^{-7}$	0.15	$5.43*10^{-5}$

The primary creep curve as in power form can be written as

$$\varepsilon_p = \varepsilon_0 + m * x^n \quad (25)$$

where ε_p is the primary strain, $\varepsilon_0$is the instantaneous strain (%) and m and n are constants which varies with stress and temperature. The constants value is tabulated in table 29. The fitted curves for all three samples are shown in Fig. 85. The fit is much better with this approach.

Table 29: Constants of primary creep curve equation

Sample	**ε_0**	**m**	**n**
NiCrY2O3Al2O3_100MPa	1.40	0.93	0.07
NiCrY2O3Al2O3_80MPa	1.10	0.85	0.06
NiCrY2O3Al2O3_60MPa	0.55	0.43	0.06

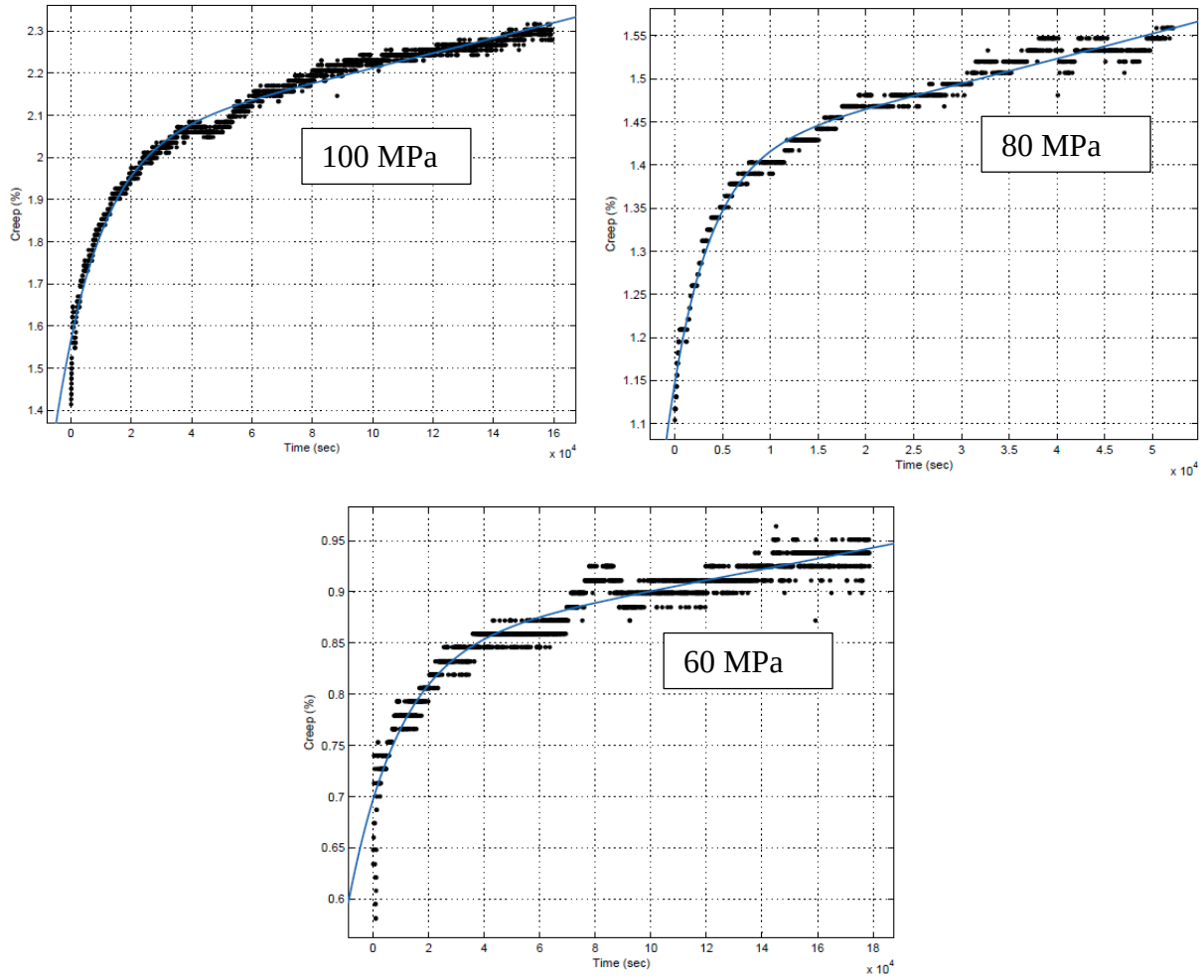

Figure 84. The fitted primary creep curve as exponential plot.

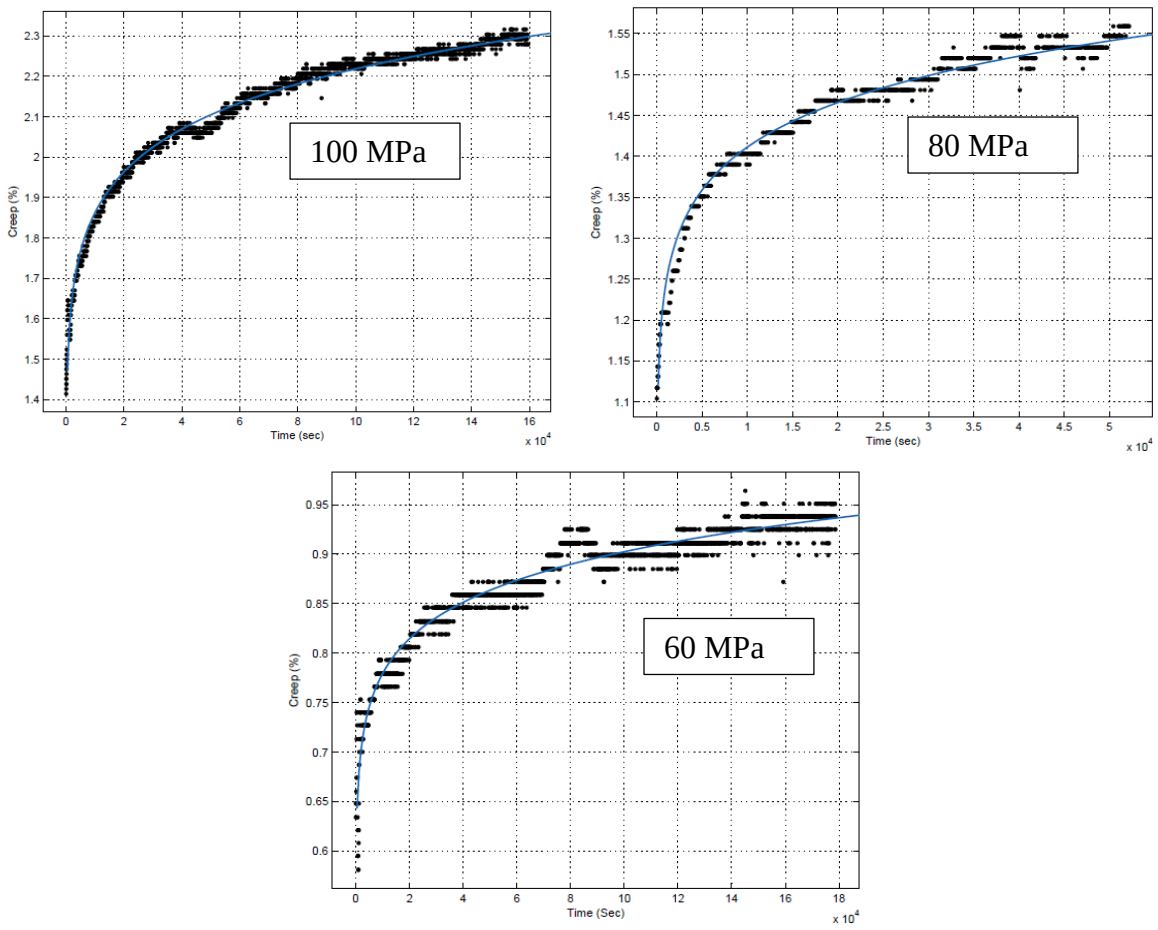

Figure 85. The fitted primary creep curve as power function plot.

Nanoindentation

The Ni-Cr-1.2Y_2O_3-5Al_2O_3 sample was used for nanoindentation experiments. A set of 20 x 20 μm^2 area was selected. Nanoindentation experiments were carried out in a 5 x 5 matrix with keeping 5 μm separation between two consecutive points in X and Y directions. The location of points is shown in Fig. 86. The contour of elastic modulus and hardness along with point-line plot for the same are shown in Fig. 87 (a)-(d). The hardness varies between 4 to 7 GPa and elastic modulus between 180 to 230 GPa. The average elastic modulus and hardness are approximately 200 GPa and 5.5 GPa respectively. The load-displacement curve is shown in Fig. 87 (e). The global shape of P-h curve differ from material to material and usually reflects the different mechanical properties. The contour plot of elastic modulus and hardness gives an idea of distribution of dispersoid and reinforcement particles in Ni-Cr matrix.

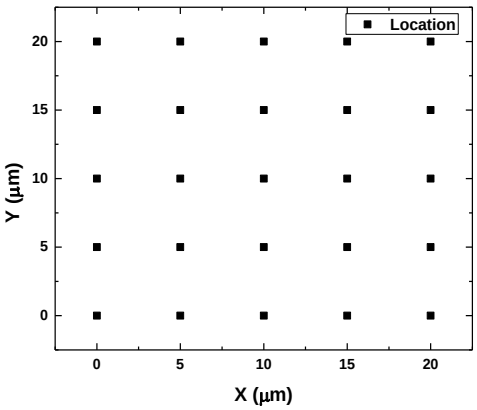

Figure 86. Location of point of interest for nanoindentation.

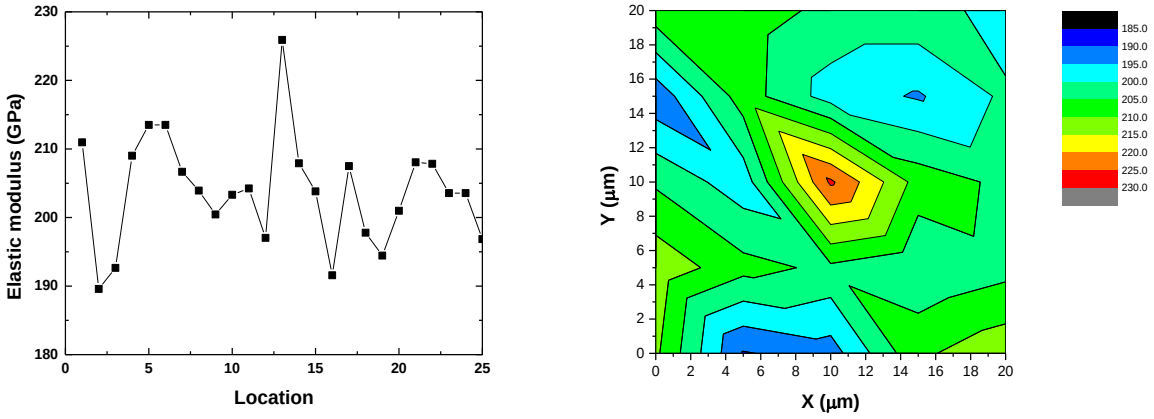

(a)

(b)

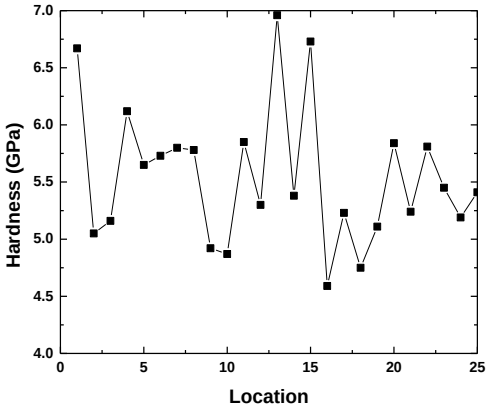

(c)

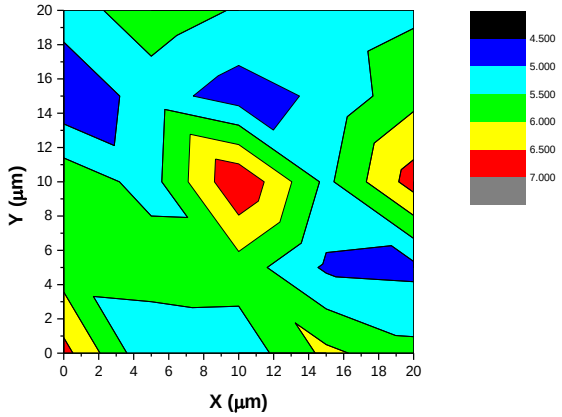

(d)

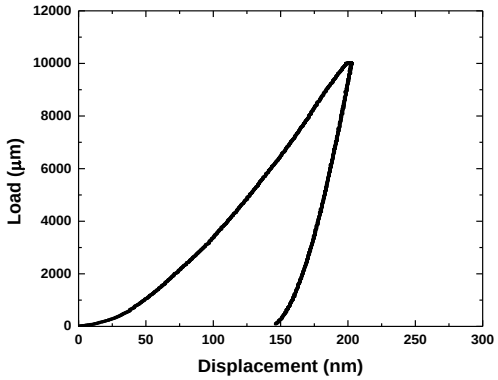

(e)

Figure 87. (a) Elastic modulus plot (b) contour of elastic modulus (c) hardness plot (d) contour of hardness and (e) load-displacement curve of Ni-Cr-1.2Y_2O_3-5Al_2O_3.

3D atom probe

Atom probe tomography (APT) studies were performed on Ni-20Cr-1.2Y_2O_3-5Al_2O_3 sample. Figure 88 shows the atomic distribution of Ni and Cr atoms. Atomic distribution of Al and Y are shown in Fig. 89. The atom maps of combined Ni, Cr, Al and Y and O are shown in Fig. 90 (a) and (b) respectively. Ni and Cr atoms are distributed in more portions of the observed 3DAP analyzed images. Al particles exist mainly on top and right bottom corner. Y exist more at the center of the image. The O atom maps confirm the existence of Y2O3 at middle and Al2O3 particles at the top and bottom corner mainly. Figure 91 shows count verses mass-to-charge state ratio for different ions. Figure 92 shows 1-D profile of atomic concentration along to bottom. It is observed from concentration profile that Al particle mostly exist on top and Y particle in middle while Ni and Cr are uniformly distributed.

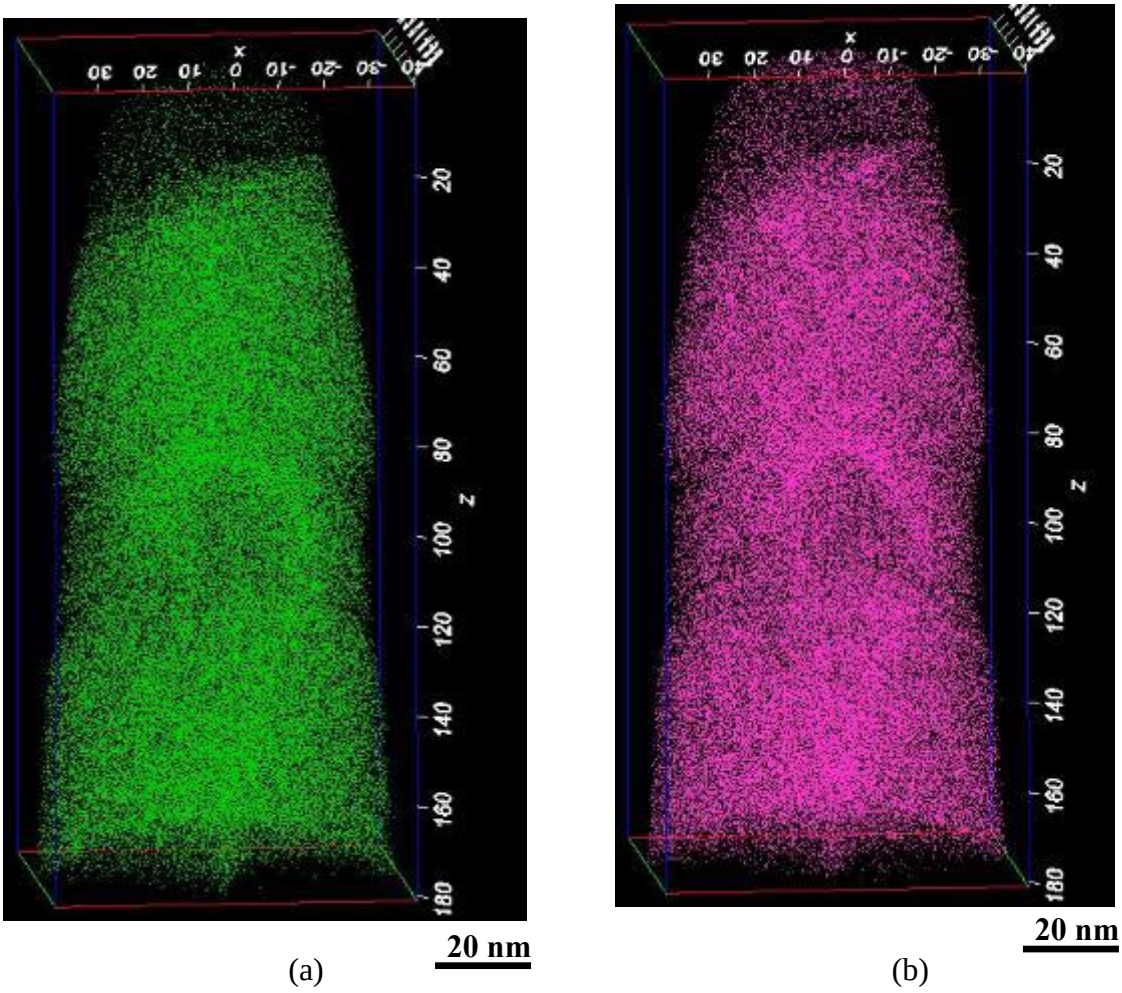

Figure 88. Atomic distribution of (a) Ni and (b) Cr.

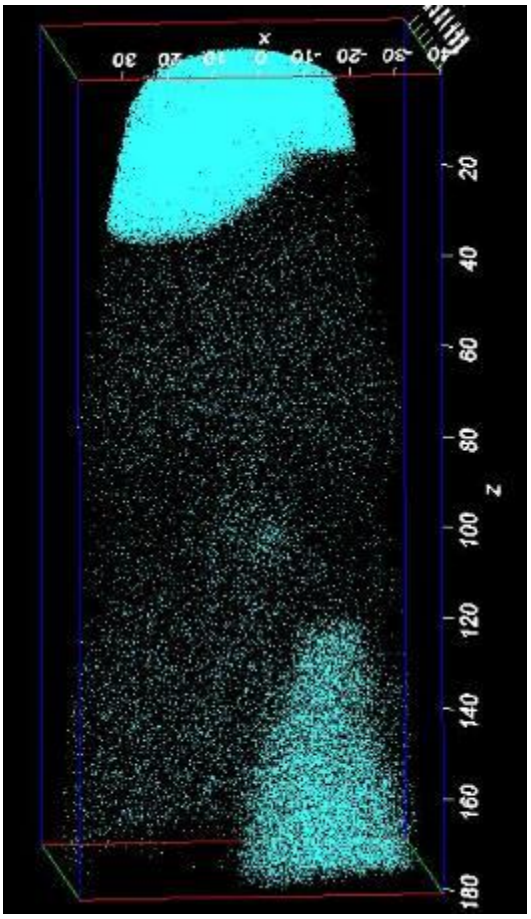

(a)

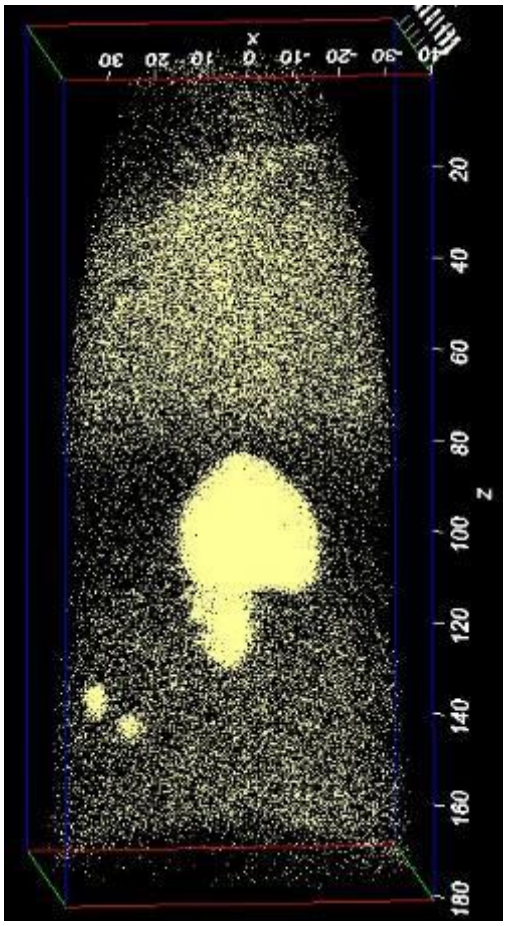

(b)

Figure 89. Atomic distribution of (a) Al and (b) Y.

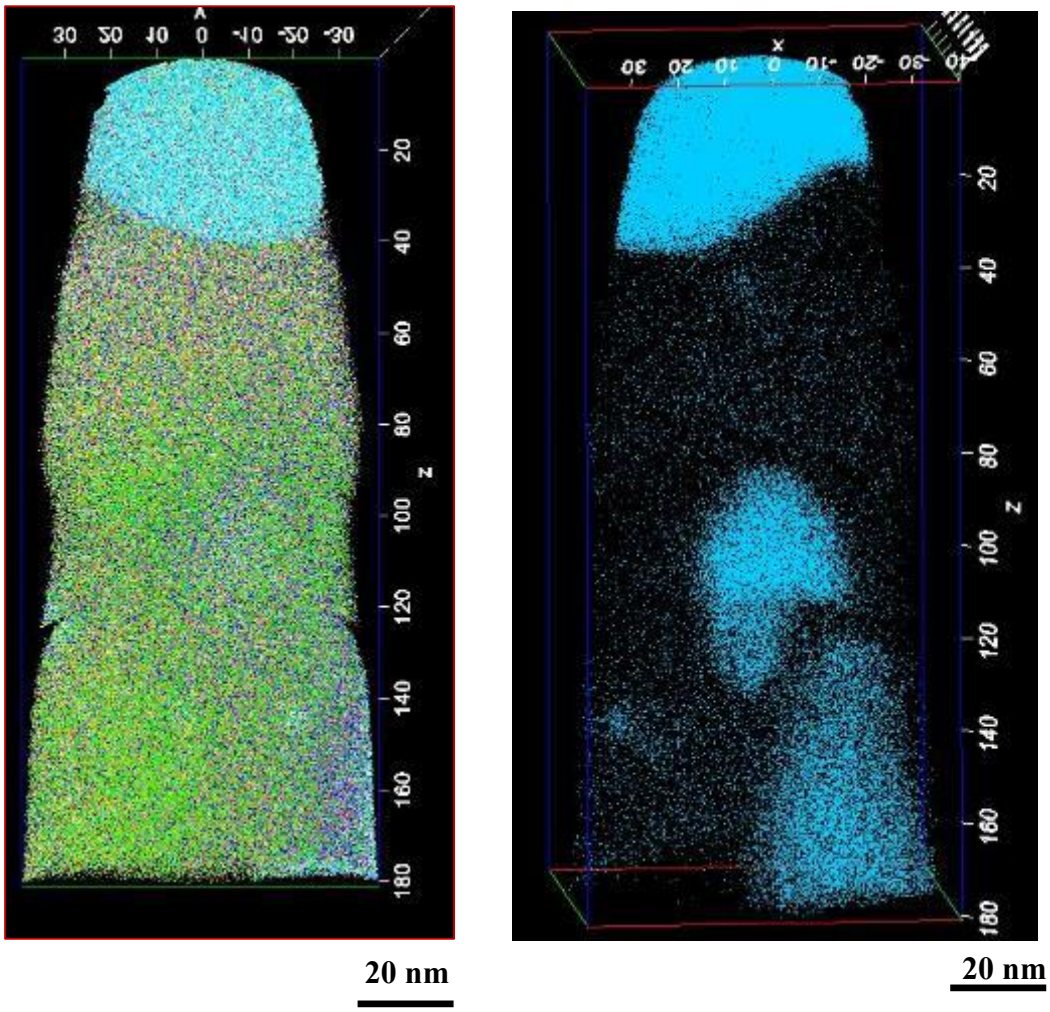

(a) (b)

Figure 90. Atomic distribution of (a) Ni, Cr, Al and Y (b) O atoms

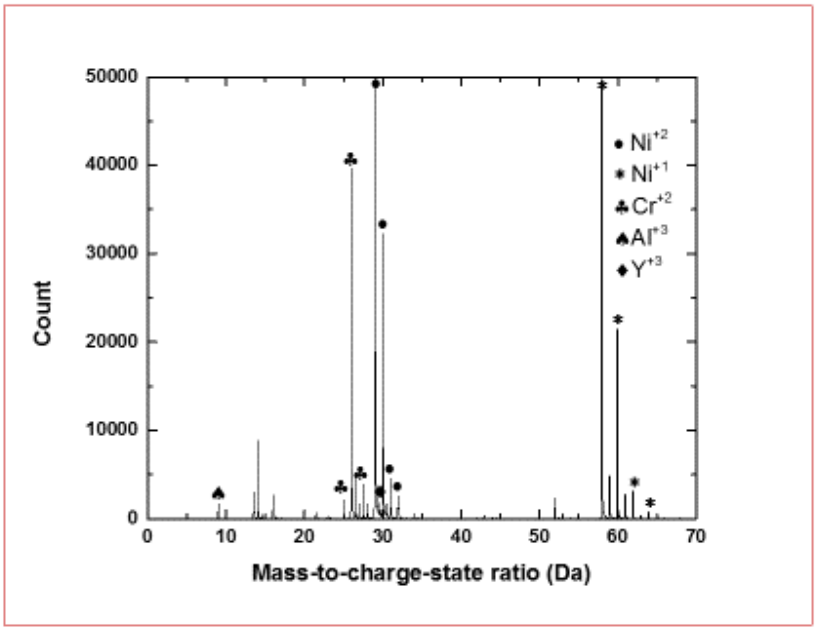

Figure 91. APT mass spectrum of Ni-ODS.

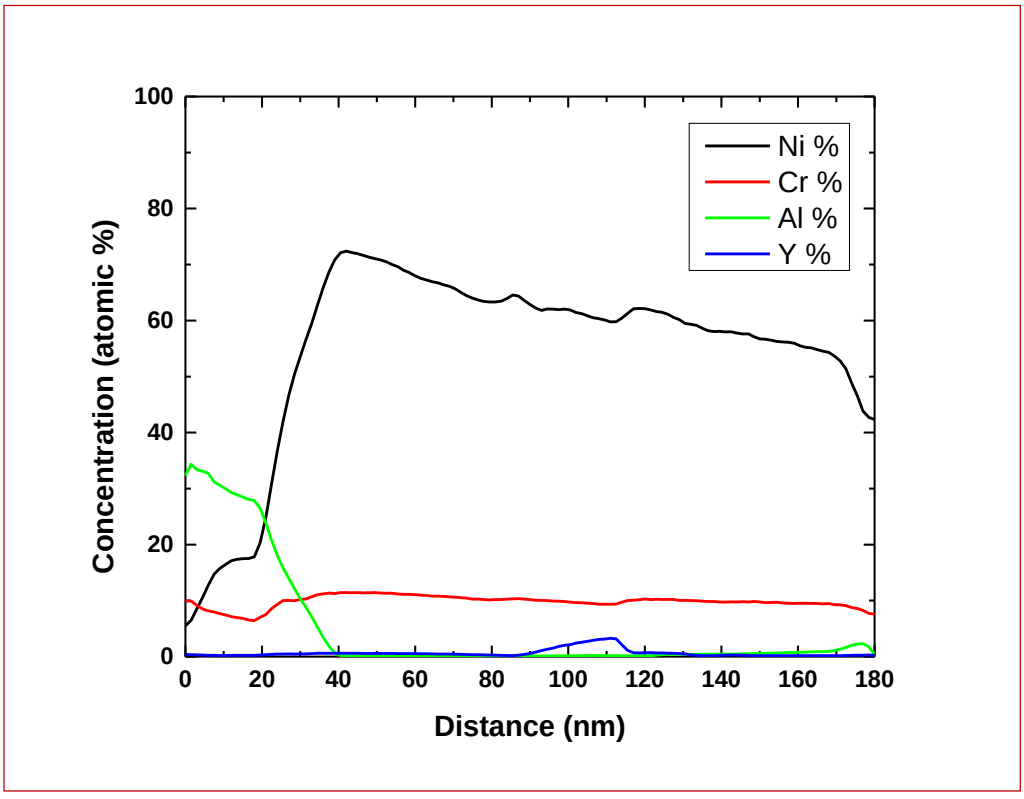

Figure 92. 1-D concentration profile of Ni, Cr, Al and Y.

CONCLUSIONS

The present work was done to develop a new alloy using 'materials by design' technique. Microstructural development of high temperature Ni-Cr ODS alloy was performed through genetic algorithm approach. Ni-20Cr, Ni-20Cr-1.2Y_2O_3 and Ni-20Cr-1.2Y_2O_3-5Al_2O_3 were developed via milling and SPS. The effects of milling time, sintering time and temperature, and alloying composition on overall microstructure, annealing twins, particles size distribution and hardness and compression yield stress of nickel-based ODS alloys were investigated. The following conclusions were made:

a) The conventional approach typically takes 15-20 years to develop new materials. Materials can be developed in shorter time through 'materials by design' approach. To obtain desired mechanical properties (low temperature strength, ductility and high temperature strength), objective function was optimized through genetic algorithm. Simulation for high temperature strength was carried out for 10^{-9} s^{-1} strain rate at 800 ^oC. The observed (calculated) high temperature strength was 43 MPa for dispersoid size range 30-40 nm. It increased to 100 MPa with consideration of wide range of dispersoid size. Introduction of two types of dispersoids with variations in size increased high temperature strength to 150 MPa.
b) The grains in unmilled sintered alloys were in micron size range. The grain size was significantly reduced after 2 and 4 h of milling. The presence or absence of milling has no influence on manifestation of the twins. However, for longer milling times, higher amount of stored energy decreased the activation energy of twin formation and led to a higher volume fraction of twins. The twin width also decreased at longer milling times due to finer crystallite size. Longer milling time (>4 h) led to dissolution of Y_2O_3 in Ni-20Cr and produced complex Y-Cr-O particles.
c) Higher sintering temperature provided higher hardness and density, and higher volume fraction of twins. The oxide particles were stable up to 1100 °C and could efficiently control the recrystallization process and inhibit any grain growth.
d) Adding Y_2O_3 to Ni-20Cr contributed to significant dispersion hardening and additional presence of coarser Al_2O_3 provided composite strengthening in Ni-20Cr matrix alloy. A higher compression yield stress at 800 °C was obtained for the Ni-20Cr-1.2Y_2O_3-5Al_2O_3 alloy. The microstructure of this alloy contained a high density of nanograins and dislocations that were effectively controlled by nanoparticles.
e) The observed creep rate was of the order of 10^{-9} s-1 for this longer time creep test of Ni-20Cr -1.2Y_2O_3-5Al_2O_3, lending support to the overall approach pursued in this project.

GRAPHICAL MATERIALS LIST

Figure 19(a). GA plot of case 1 for condition VII. (b). GA plot of case 2 for condition VII. (c). GA plot of case 3 for condition VII. (d). GA plot of case 4 for condition VII. (e). GA plot of case 5 for condition VII.

Figure 20. GA plot of case [10 1 1] for condition VIII (1).

Figure 21. GA plot of case [1 1 10] for condition VIII (1).

Figure 22. GA plot of case [10 1 1] for condition VIII (2).

Figure 23. GA plot of case [1 1 10] for condition VIII (2).

Figure 24. GA plot of case [10 1 1] for condition VIII (3).

Figure 25. GA plot of case [1 1 10] for condition VIII (3).

Figure 26. GA plot of case [10 1 1] for condition VIII (4).

Figure 27. GA plot of case [1 1 10] for condition VIII (4).

Figure 28. GA plot of case [10 1 1] for condition VIII (5).

Figure 29. GA plot of case [1 1 10] for condition VIII (5).

Figure 30. GA plot of case [10 1 1] for condition VIII (6).

Figure 31. GA plot of case [1 1 10] for condition VIII (6).

Figure 32. GA plot of case [10 1 1] for condition IX (1).

Figure 33. GA plot of case [1 1 10] for condition IX (1).

Figure 34. GA plot of case [10 1 1] for condition IX (2).

Figure 35. GA plot of case [1 1 10] for condition IX (2).

Figure 36. GA plot of case [10 1 1] for condition X (1).

Figure 37. GA plot of case [1 1 10] for condition X (1).

Figure 38. GA plot of case [10 1 1] for condition X (2).

Figure 39. GA plot of case [1 1 10] for condition X (2).

Figure 40. The XRD pattern from the as-received Ni-20Cr powder (note that diffraction angle, 2θ, is in degree).

Figure 41. A SEM micrograph of the as-received Ni-20Cr powder.

Figure 42. The XRD pattern from the as-received nano-yttria powder (note that the diffraction angle 2θ is in degree).

Figure 43. a) A SEM micrograph of the nano-yttria powder; b) A STEM HAADF micrograph from the as-received Y_2O_3 powder.

Figure 44. The XRD pattern of the as-received α-Al_2O_3 powder.

Figure 45. A SEM micrograph of the as-received α-Al_2O_3 powder.

Figure 46. The XRD pattern of the powder mixture Ni-20Cr-1.2Y_2O_3 (before ball milling). Note that the diffraction angle (Y-axis) is in the unit of degree.

Figure 47. SEM images of the unmilled powder showing the powder morphology.

Figure 48. A high-magnification image of the blended powder showing the EDS results of a powder particle. Note the evidence of yttrium in the selected region of EDS analysis.

Figure 49. XRD patterns of the Ni-20Cr-1.2Y_2O_3 powder milled under different conditions.

Figure 50. SEM images of the Ni-20Cr-1.2Y_2O_3 powder milled for 4 h with (a) ethanol, (b) PEG and (c) stearic acid.

Figure 51**.** (a) A SEM micrograph of Ni-20Cr-1.2Y_2O_3-5Al_2O_3 alloy after sintering at 1100 ^oC for 30 min, and (b) the corresponding EDS spectrum taken from the square shown in Fig. 51a (the Al_2O_3 particles were blended with milled Ni-20Cr-1.2Y_2O_3 powders without further milling).

Figure 52**.** A TEM bright field micrograph of Ni-20Cr-1.2Y_2O_3-5Al_2O_3 after sintering at 1100 ^oC for 30 min (the Al_2O_3 particles were blended with the milled Ni-20Cr-1.2Y_2O_3 powder without further milling).

Figure 53**.** SEM micrographs of the Al_2O_3 powder milled for (a) 20 min, (b) 30 min, (c) 60 min and (d) 120 min at a magnification of 500 X.

Figure 54**.** SEM micrographs from the Al_2O_3 particles milled for (a) 0 min (i.e. no milling), (b) 20 min, (c) 30 min, (d) 60 min, and (e) 120 min at 12 kX.

Figure 55. A SEM micrograph of the as-milled Ni-20Cr-1.2Y_2O_3-5Al_2O_3 powder.

Figure 56**.** The true stress-strain plots for Ni-20Cr, Ni-20Cr-1.2Y_2O_3 and Ni-20Cr-1.2Y_2O_3-5Al_2O_3 sintered at 1100 ^oC for 30 min.

Figure 57. A TEM micrograph of the ball milled (2 h) Ni-20Cr-1.2Y_2O_3 alloy.

Figure 58. TEM bright field images of SPSed a) Ni-20Cr and b) Ni-20Cr-1.2Y_2O_3 alloys.

Figure 59. Twin bands observed in the SPSed a) Ni-20Cr and b) Ni-20Cr-1.2Y_2O_3 alloys.

Figure 60. Particles in the (a) SPSed Ni-20Cr alloy and (b) Ni-20Cr-1.2Y_2O_3 alloy

Figure 61. (a) A TEM image of the SPSed Ni-20Cr-1.2Y_2O_3 alloy. (b) The EDS spectrum taken from the small particles shows the presence of yttrium.

Figure 62. (a) and (b) TEM bright field images showing the grain structure and particle microstructure in the SPSed Ni-20Cr-1.2Y_2O_3 alloy (milled – 2h, SPS – 900 ^oC/5 min).

Figure 63. (a) A bright field TEM image of the Ni-20Cr-1.2Y_2O_3 alloy (milled for 4 h, SPSed at 1100 ^oC for 30 min) from the smaller grain region and (b) the corresponding SAD pattern. (c) A bright field TEM image of the same sample from the larger grain region and (d) the corresponding SAD pattern.

Figure 64. The TEM lamella from the sintered Ni-20Cr-1.2Y_2O_3-5Al_2O_3 alloy prepared by FIB.

Figure 65. The TEM micrographs from the lamella with a nominal composition of Ni-20Cr-1.2Y_2O_3-5Al_2O_3 after sintering at 1100 ^oC for 30 min: (a) a bright field image overview of the microstructure, (b) BF image showing recrystallized grains, (c) DF from Fig. 65b, and (d) the diffraction pattern obtained from Fig. 65(b).

Figure 66. (a) TEM BF image showing twins and (b) HRTEM image of twins in Ni-20Cr-1.2Y_2O_3-5Al_2O_3 alloy.

Figure 67. (a) HDAAF image from Ni-20Cr-1.2Y_2O_3-5Al_2O_3 alloy with 4 different Z contrast areas, (b) EDS spectrum of area 1, (c) EDS spectrum of area 2, (d) EDS spectrum of area 3, and (e) EDS spectrum of area 4.

Figure 68**.** (a) A HDAAF image from Ni20Cr1.2Y_2O_3 5Al_2O_3 with 4 different Z contrast areas, (b) EDS spectrum of area 1, (c) EDS spectrum of area 2, (d) EDS spectrum of area 3 and (e) EDS spectrum of area 4.

Figure 69. The micrographs of Ni-20Cr-1.2Y_2O_3 alloy milled for (a) 0 h (alloy A), (b) 2 h (alloy B), (c) 4 h (alloy C) showing nanograins and (d) 4 h (alloy C) showing coarser grains.

Figure 70**.** The oxide dispersoids in the microstructure of the SPSed Ni-20Cr-1.2Y_2O_3 alloys milled for (a) 2 h (alloy B) and (b) 4 h (alloy C).

Figure 71. The microstructure of Ni-20Cr-1.2Y_2O_3 alloy sintered at (a) 900 °C for 5 min (alloy E), (b) 1100 °C for 5 min (alloy G) and (c) 1100 °C for 30 min (alloy B).

Figure 72. Twins in the microstructure of Ni-20Cr-1.2Y_2O_3 alloys sintered at (a) 900 °C for 5 min (alloy E), (b) 1100 °C for 5 min (alloy G) and (c) 1100 °C for 30 min (alloy B).

Figure 92. 1-D concentration profile of Ni, Cr, Al and Y.

REFERENCES

[1] Q. Tang, T. Hoshino, S. Ukai, B. Leng, S. Hayashi, Y. Wang, Refinement of Oxide Particles by Addition of Hf in Ni-0.5 mass% Al-1 mass% Y2O3 Alloys, Materials transactions. 51 (2010) 2019-2024.

[2] J. Park, J. Jang, T.K. Kim, S. Kim, J. Ahn, Formation of Nanostructures in Ni-22Cr-11Fe-1X (X= Y2O3, TiO2) Alloys by High-Energy Ball-Milling, Journal of nanoscience and nanotechnology. 11 (2011) 6213-6218.

[3] J. Zbiral, Tensile properties of mechanically alloyed/milled Ods-Ni-Based alloys, Metallurgical and Materials Transactions A. 27 (1996) 1371-1377.

[4] M. Lee, J. Park, C. Rhee, Synthesis and structural properties of Ni–20Cr–2Y 2 O 3 nanocomposite alloy prepared by a very high energy mechanical milling, Mater. Chem. Phys. 137 (2012) 129-134.

[5] D. Srolovitz, M. Luton, R. Petkovic-Luton, D. Barnett, W. Nix, Diffusionally modified dislocation-particle elastic interactions, Acta Metallurgica. 32 (1984) 1079-1088.

[6] E. Arzt, J. Rösler, The kinetics of dislocation climb over hard particles—II. Effects of an attractive particle-dislocation interaction, Acta Metallurgica. 36 (1988) 1053-1060.

[7] B. Reppich, On the attractive particle–dislocation interaction in dispersion-strengthened material, Acta materialia. 46 (1998) 61-67.

[8] J. Park, H. Choe, S. Hong, M. Lee, C. Rhee, Synthesis of Ni–Y 2 O 3 nanocomposite powders by a very high speed planetary milling process: microstructural development and refinement behavior, Powder Technol. 230 (2012) 139-144.

[9] E. Orowan, Discussion on internal stresses, (1948) 451-453.

[10] R.J. Arsenault, Strengthening Mechanisms in Discontinuous SiC/Al Composites, in: I.H. Marshall (Ed.), Springer Netherlands, 1987, pp. 70-81.

[11] H. Wang, P. Shi, H. Yu, B. Xu, Preparation and Micro Mechanical Properties of Nano-Al2O3 Particles Strengthened Ni-based Composite Coatings, Physics Procedia. 50 (2013) 225-230.

[12] A. Kuruvilla, V. Bhanuprasad, K. Prasad, Y. Mahajan, Effect of different reinforcements on Composite-strengthening in aluminium, Bull. Mater. Sci. 12 (1989) 495-505.

[13] E. Hornbogen, E. Starke, Overview no. 102 Theory assisted design of high strength low alloy aluminum, Acta metallurgica et materialia. 41 (1993) 1-16.

[14] J. Rösler, M. Bäker, A theoretical concept for the design of high-temperature materials by dual-scale particle strengthening, Acta materialia. 48 (2000) 3553-3567.

[15] C. Suryanarayana, N. Al-Aqeeli, Mechanically alloyed nanocomposites, Progress in Materials Science. 58 (2013) 383-502.

[16] R. Darolia, J.J. Lewandowski, C. Liu, P. Martin, D. Miracle, M. Nathal, Structural intermetallics. (1993).

[17] K.N. Allahar, J. Burns, B. Jaques, Y. Wu, I. Charit, J. Cole, D.P. Butt, Ferritic oxide dispersion strengthened alloys by spark plasma sintering, J. Nucl. Mater. 443 (2013) 256-265.

[18] Z. Munir, U. Anselmi-Tamburini, M. Ohyanagi, The effect of electric field and pressure on the synthesis and consolidation of materials: a review of the spark plasma sintering method, J. Mater. Sci. 41 (2006) 763-777.

[19] M. Alinger, G. Odette, G. Lucas, Tensile and fracture toughness properties of MA957: implications to the development of nanocomposited ferritic alloys, J. Nucl. Mater. 307 (2002) 484-489.

[20] S. Kandukuri, A FAST winner for fully dense nano powders, Metal Powder Report. 63 (2008) 22-27.

[21] H. Ke, X. Li, Y. Chao, Y. Li, Densification and microstructure evolution during SPS consolidation process in W-Ni-Fe system, Transactions of Nonferrous Metals Society of China. 21 (2011) 493-501.

[22] J.R. Groza, A. Zavaliangos, Sintering activation by external electrical field, Materials Science and Engineering: A. 287 (2000) 171-177.

[23] S. Pasebani, A.K. Dutt, I. Charit, R.S. Mishra, Nickel-Chromium Alloys: Engineered Microstructure via Spark Plasma Sintering, 783 (2014) 1099-1104.

[24] M. Nanko, M. Sato, K. Matsumaru, K. Ishizaki, Densification mechanism of fine Ni-20Cr powder during pulsed electric current sintering, 510 (2006) 818-821.

[25] A.J. Kulkarni, K. Krishnamurthy, S. Deshmukh, R. Mishra, Microstructural optimization of alloys using a genetic algorithm, Materials Science and Engineering: A. 372 (2004) 213-220.

[26] I. López-Báez, E. Martinez-Franco, H. Zoz, L. Trápaga-Martínez, Structural evolution of Ni-20 Cr alloy during ball milling of elemental powders, Revista mexicana de física. 57 (2011) 176-183.

[27] E. Hall, The deformation and ageing of mild steel: III discussion of results, Proceedings of the Physical Society.Section B. 64 (1951) 747.

[28] N. Petch, The cleavage strength of polycrystals, J.Iron Steel Inst. 174 (1953) 25-28.

[29] L. Gypen, A. Deruyttere, Multi-component solid solution hardening, J. Mater. Sci. 12 (1977) 1028-1033.

[30] H. Roth, C. Davis, R. Thomson, Modeling solid solution strengthening in nickel alloys, Metallurgical and Materials Transactions A. 28 (1997) 1329-1335.

[31] E. Nembach, Particle strengthening of metals and alloys, (1997).

[32] B. Majumdar, A. Pandey, Deformation and fracture of a particle-reinforced aluminum alloy composite: Part II. Modeling, Metallurgical and Materials Transactions A. 31 (2000) 937-950.

[33] R. Mishra, T. Nandy, G. Greenwood, The threshold stress for creep controlled by dislocation-particle interaction, Philos. Mag. A. 69 (1994) 1097-1109.

[34] D. Srolovitz, R. Petkovic-Luton, M. Litton, Diffusional relaxation of the dislocation-inclusion repulsion, Philos. Mag. A. 48 (1983) 795-809.

[35] V. Nardone, D. Matejczyk, J. Tien, The threshold stress and departure side pinning of dislocations by dispersoids, Acta Metallurgica. 32 (1984) 1509-1517.

[36] E. Arzt, D. Wilkinson, Threshold stresses for dislocation climb over hard particles: the effect of an attractive interaction, Acta Metallurgica. 34 (1986) 1893-1898.

[37] R. Mishra, A. Paradkar, K. Rao, Steady state creep behaviour of a rapidly solidified and further processed Al-5 wt% Ti alloy, Acta metallurgica et materialia. 41 (1993) 2243-2251.

[38] A. Kulkarni, K. Krishnamurthy, S. Deshmukh, R. Mishra, Effect of particle size distribution on strength of precipitation-hardened alloys, J. Mater. Res. 19 (2004) 2765-2773.

[39] S. Deshmukh, R. Mishra, I. Robertson, Investigation of creep threshold stresses using in situ TEM straining experiment in an Al–5Y 2 O 3–10SiC composite, Materials Science and Engineering: A. 527 (2010) 2390-2397.

[40] A. Foreman, M. Makin, Dislocation movement through random arrays of obstacles, Philosophical magazine. 14 (1966) 911-924.

[41] M. Cieplak, M.O. Robbins, Influence of contact angle on quasistatic fluid invasion of porous media, Physical Review B. 41 (1990) 11508.

[42] A.C. Fischer-Cripps, Critical review of analysis and interpretation of nanoindentation test data, Surface and coatings technology. 200 (2006) 4153-4165.

[43] C. Dong, PowderX: Windows-95-based program for powder X-ray diffraction data processing, Journal of Applied Crystallography. 32 (1999) 838-838.

[44] J.B. Nelson, D. Riley, An experimental investigation of extrapolation methods in the derivation of accurate unit-cell dimensions of crystals, Proceedings of the Physical Society. 57 (1945) 160.

[45] G. Williamson, W. Hall, X-ray line broadening from filed aluminium and wolfram, Acta metallurgica. 1 (1953) 22-31.

[46] U. Kocks, A statistical theory of flow stress and work-hardening, Philosophical Magazine. 13 (1966) 541-566.

[47] J.P. Hirth, J. Lothe, Theory of dislocations, (1982).

[48] F.R. Nabarro, Theory of crystal dislocations, (1967).

PUBLICATIONS/PRESENTATIONS

Publications:

S. Pasebani, A.K. Dutt, J. Burns, I. Charit and R.S. Mishra, "Oxide Dispersion Strengthened Nickel Based Alloys via Spark Plasma Sintering," *Materials Science & Engineering A,* 630 (2015) 155-169.

S. Pasebani, A.K. Dutt, I. Charit and R.S. Mishra, "Nickel-Chromium Alloys: Engineered Microstructure via Spark Plasma Sintering," (Invited) High & Ultra High Temperature Materials (Intermetallics, Superalloys & Refractory Metals), International Conference on Processing & Manufacturing of Advanced Materials (Thermec'13, Dec. 2-6, 2013, Las Vegas, NV, USA); published in *Materials Science Forum*, Vols. 783-786 (2014) 1099-1104.

Somayeh Pasebani, "Processing of Oxide Dispersion Strengthened Alloys via Mechanical Alloying and Spark Plasma Sintering," PhD Dissertation, University of Idaho, July 2014.

Oral Presentations:

A.K. Dutt, S. Pasebani, I. Charit and R.S. Mishra, "Microstructural Optimization of High Temperature Ni-Cr ODS Alloy Using Genetic Algorithm," Computational Modeling and Stochastic Methods for Materials Discovery and Properties, TMS Annual Meeting & Exhibition, Orlando, FL, Mar. 15-19, 2015.

S. Pasebani, A.K. Dutt, I. Charit and R.S. Mishra, "Novel Processing and Characterization of Nickel Based Oxide Dispersion Strengthened Alloys," Novel Synthesis and Consolidation of Powder Materials, TMS Annual Meeting & Exhibition, Orlando, FL, Mar. 15-19, 2015.

S. Pasebani, A. Dutt, I. Charit, and R.S. Mishra, "Development of Ni-Cr Based Alloys via Spark Plasma Sintering for High Temperature Applications," Materials for High Temperature Applications – Next Generation Superalloys and Beyond, TMS Annual Meeting & Exhibition, San Diego, CA, Feb. 16-20, 2014.

S. Pasebani, A.K. Dutt, I. Charit and R.S. Mishra, "Effect of Yttria and Alumina on the Microstructure and Mechanical Properties of Ni-Cr Based Alloys," 56th Idaho Academy of Science Annual Meeting and Symposium, Moscow, Idaho, March 21, 2014.

Poster Presentation:

S. Pasebani, A. Dutt, I. Charit, R.S. Mishra, "A Novel Route to Process Ni-20Cr Based Alloys for High Temperature Applications," SMD 2014 Technical Division Student Poster Contest, TMS Annual Meeting & Exhibition, San Diego, CA, Feb. 16-20, 2014.